Experiments on sublimation and contact forces of water ice particles and their application on planet formation

von der

Fakultät für Physik
der Universität Duisburg-Essen

zur Erlangung des akademischen Grades
Doktor der Naturwissenschaften
(Dr. rer. nat.)

genehmigte Dissertation

von

MSc.-Astrophys. Guillem Aumatell Gómez

aus

Barcelona

18.07.2014

Gutachter:
Prof. Dr. Gerhard Wurm
Prof. Dr. Carsten Dominik

Tag der Disputation: 20. November 2014

Experiments on Sublimation and contact forces of water ice particles and their application on planet formation

Dissertation von

MSc.-Astrophys. Guillem Aumatell Gómez

Zur Erlangung des akademischen Grades
Dr. rer. nat.

UNIVERSITÄT DUISBURG ESSEN

Offen im Denken

Fakultät für Physik
Universität Duisburg-Essen
Deutschland
18.07.2014

Contents

Abstract

To date, the most accepted planet formation's model is the so called "Nebular Hypothesis". It proposes that planets are formed in a nebular region which remains orbiting around stars before they enter in the main sequence stage. This nebula, made of gas and dust, is called "Protoplanetary Disc" (PPD) due to its flat and symmetrical shape. Sub-micrometre particles' aggregation is the main growth mechanism during the first planet formation phase in the disc. Contact forces between the constituents of solid aggregates determine the outcome of collisional events which occur in the disc. Icy grains are very abundant in regions where water condensates into solid state (regions situated beyond the so called "Snowline"). It implies that water ice is a fundamental ingredient during the planetesimal formation process.

In this thesis, experiments on ice coagulation, sublimation and fragmentation are carried out in order to compare the obtained results with the existing theories. It is shown that sublimation of relatively large icy aggregates ($\sim$ 1 metre) close to the snowline cause their fragmentation and the subsequent concentration of solids in this region, boosting planetesimal formation.

Making use of a "Temperature Gradient Force Microscope" (TGFM), critical forces between water ice particles are determined. This setup allows to establish an upper limit of variables related to contact physics like rolling and twisting torques. When the radius of the contact surface formed between two ice grains is $\lesssim$ 1 nm, actual theories are not able to predict the experimental observations. The variation of water ice's surface energy may cause a reduction of the difference rate between experimental results and theoretical predictions. However, the development of a new model at such small scales may solve the issues presented in this thesis.

Das bis heute am meisten akzeptiertes Modell der Planetenentstehung ist die so genannte "Nebular Hypothese". Diese nimmt an, dass Planeten in einer nebeligen Region, die einen neu enstandenen Sterne umkreist, gebildet werden. Diese Sterne haben die Hauptreihenphase noch nicht erreicht. Der Nebel besteht aus Gas und Staub, und wird wegen seines flachen und symmetrischer Form "Protoplanetarische Scheibe" (PPD auf Englisch) genannt. Die Aggregation Sub-mikrometer Partikeln ist der Hauptwachstumsmechanismus während der ersten Phase der Planetenbildung in der Scheibe. Kontaktkräfte zwischen den Bestandteilen der festen Aggregate, bestimmen das Ergebnis der Kollisionsereignisse, die in der Scheibe auftreten.Eispartikel sind sehr zahlreich in Regionen vorhanden, in denen Wasser in festen Zustand kondensiert (Regionen jenseits die so genannte "Schneelinie"). Es impliziert, dass Wassereis ein Grundbestandteil während des Planetesimalbildungsprozess ist.

In dieser Arbeit werden Experimente zu Eis Koagulation, Sublimation und Fragmentierung durchgeführt, und die erhaltenen Ergebnisse mit den bestehenden Theorien verglichen. Die Sublimation von relativ großen Eisaggregaten ($\sim$ 1 Meter) in der Nähe der Schneelinie, führen zu ihrer Fragmentation und die anschließende Konzentration der Feststoffe in dieser Region. Das erhöht die Bildung von Planetesimalen.

Durch die Nutzung eines Temperatur-Gradient-Kraft-Mikroskop (Thermal Gradient Force Microscope -TGFM- auf Englisch) werden kritische Kräfte zwischen Wassereisteilchen bestimmt. Dieser Aufbau ermöglicht die Obergrenze von Variablen im Zusammenhang mit Kontaktphysik wie die Rollbewegungs- und das Twistens Drehmomente herzustellen. Wenn der Radius der Kontaktfläche zwischen zwei Eispartikeln $\lesssim$ 1 nm ist, sind die Theorien nicht in der Lage, die experimentellen Beobachtungen vorherzusagen. Die Variation der Oberflächenenergie des Wassereis, könnte die Differenzrate zwischen experimentellen Ergebnisse und theoretischen Vorhersagen verringern. Jedoch, die Entwicklung eines neues Modell bei so kleinen Skalen könnte helfen die - sich in dieser Dissertation zeigenden - Probleme zu lösen.

A dia d'avui, el model més acceptat en el camp de la teoria de formació planetària es coneix com l'"Hipòtesi Nebular". Aquest model sosté que els planetes es formen en una nebulosa que roman orbitant al voltant dels estels, abans que aquests entrin en la seqüència principal. Aquesta nebulosa, composta de gas i pols, rep el nom de "Disc Protoplanetari" (PPD en anglès). El mecanisme més important que té lloc dins el disc durant la primera fase de formació planetària, és l'agregació de partícules submil-limètriques. Les forces de contacte entre els constituents dels agregats sòlids determinen el resultat de col-lisions mútues presents en el disc. Els grans de gel són molt abundants en regions on l'aigua es condensa en estat sòlid (regions que es troben situades més enllà de l'anomenada "Línia de Gel"). Això implica que el gel d'aigua es un ingredient clau en el procés de formació planetària.

En aquesta tesi s'han realitzat experiments sobre la coagulació, sublimació i fragmentació de gel d'aigua, amb la finalitat de comparar-ne els resultats amb les teories existents. Es mostra com la sublimació d'agregats de gel relativament grans ($\sim$ 1 metre) prop de la línia de gel, causa la fragmentació d'aquests i la seva conseqüent concentració en aquesta regió. Aquest procés és un mecanisme que hauria de fomentar la formació de planetessimals.

Fent us d'un "Microscopi de Gradients de Forces Tèrmiques" (TGFM en anglès), s'han determinat les forces de contacte crítiques entre partícules de gel d'aigua. L'equip utilitzat permet establir un límit superior d'algunes variables relacionades amb la física dels contactes, com ara els moments de força produïts per rodament i torsió. Per valors del radi de la superfície de contacte que es forma entre dos grans de gel $\lesssim$ 1 nm, les teories vigents són incompatibles amb les observacions experimentals aquí presentades. La variació de l'energia superficial del gel d'aigua podria causar una reducció en la diferència entre els resultats experimentals i les prediccions teòriques. Tot i així, el desenvolupament de nous models per a tan petites escales podria ajudar a solventar les discrepàncies plantejades en aquesta tesi.

Chapter 1

Introduction

When the ancient Greeks denominated "planet" to the objects that slowly cross the sky at night, they probably asked themselves many questions about those celestial, almost-holy objects.

- "Planet", from the ancient Greek *astērplanētēs* means "Wandering Star"

Taking as a reference the actual definition of "planet," according to the I.A.U., i. e. a celestial body which:

1. is in orbit around a star,
2. has sufficient mass to assume hydrostatic equilibrium (a nearly round shape), and
3. has cleared the neighborhood around its orbit.

what they probably couldn't imagine, is that nowadays more than 1790 objects with similar characteristics have been detected "wandering" around other stars in our Galaxy, instead of the Sun (URL: http://exoplanet.eu, 26/05/2014). They are commonly known as Extrasolar Planets or Exoplanets.

How many planets do exist in the Universe may be considered as a philosophical question rather than a scientific one, but what some experts mention, or even claim, is that at least 100 billion planets populate our Galaxy (Swift et al., 2013). Including the Solar System planets and assuming that all Exoplanets accomplish the above

mentioned definition, the way they can be put into groups is quite large. Depending on features like radius, mass, density, composition, orbital period among others, the detected planets can be classified into different types such as: Super Earths, Hot Jupiters, Hot Neptunes, Pulsar Planets or Water Worlds. However, it is believed that their formation and evolution is, from a general point of view, the same in the whole universe.

The story about "where do planets come from?" is so huge, that hundred of pages could be filled. Different hypothesis have been proposed regarding to the cosmogony throughout history. Nowadays, the most accepted one is the so called "Nebular Hypothesis". This hypothesis sustains that every celestial body that populate the Solar System was originated after a giant molecular cloud collapse. However, its acceptance has not been a trivial issue. In the 18th century, Swedenborg (Stanley, 2003), Kant and Laplace (Woolfson, 1993) proposed the formation of the solar system from a giant molecular cloud. Those ideas were, to a certain extent, controverted. After some modifications, in the next century, it became more widely accepted. The assumption of a nebular origin of not only the solar system, was first formulated by astrophysicists such as Weizsäcker (1943), Safronov (1966) and Weidenschilling (1977), among others.

The actual picture of a planet's forming region is a disc of gas and dust, known as protoplanetary disc (PPD), which surrounds a young star. Starting with a mass of about 0.3 $M_\star$ -with $M_\star$ as the star's mass- (Richling et al., 2006) and a radius of 100-1000 AU (see section 2.2.2), they contain submicrometre and micrometre sized dust and icy grains that, after several millions of years and under various physical processes, will evolve into planets, moons and minor populating bodies.

The supposed existence of protoplanetary discs was supported by the spectra of various young stellar objects (YSOs) like T-Tauri stars. They show an excess of radiation in the infrared region, indicating a possible emission from hot dust (e.g. Lada and Wilking, 1984; Adams et al., 1987; Andre and Montmerle, 1994). But this supposition became an evidence with the Hubble space telescope images of isolated YSOs with a surrounding disc, which is visible due to the shadowing of the background light coming from the Orion nebula (see figure 1.1).

Figure 1.1: Orion Nebula's image composed by multiple Hubble Space Telescope captures. The silhouette of 6 PPDs can also be seen. These silhouettes -which shadow the incoming light from the nebula- have been optically amplified in order to distinguish their shape. **Credit:** NASA, ESA, M. Robberto (Space Telescope Science Institute/ESA), the Hubble Space Telescope Orion Treasury Project Team and L. Ricci (ESO).

During many years, the study of the Earth, as well as the observation of our neighbor planets, were the only tools available for the investigation of planet formation. Due to the recent increase of computing power, the models based on different hypothesis can be tested through simulations. But the revolution on the study of planetary formation and evolution, has been taking place throughout the last 20 years, when detection of exoplanets has boosted. The result of this increasing number of discovered planets does not seem to stop in the coming years. This is due to the development of more accurate observation and analysis tools. That had already implied the modification and improvement of the actual theories.

Which processes do take place in PPDs and how do they influence its evolution until the planets are completely formed, are questions that actually does not have any clear answer. A key to solve these questions could be the comparison between the actual models and simulations with not only observational data but also with experimental results as well. It is believed that in the disc, different kind of pro-

cesses (like radial drift, Brownian movement and other mechanisms) will force solid particles to move at different relative velocity and cause mutual collisions sooner or later. In the last twenty years several experiments have been carried out in order to understand how these impacts produce larger bodies via coagulation processes (Blum and Wurm, 2008). Simulations may be implemented with experimental results in order to describe more accurately the first steps of planet formation. Recent works show that the growth of aggregates is strongly dependent on the collisional velocity and the porosity of the colliding particles. It has also been shown, that even through disruptive collisions, a net growth may occur. This fact was experimentally observed (Wurm et al., 2005) but not added to simulation models until recent years (Geretshauser et al., 2011; Windmark et al., 2012).

To date, almost all simulations and experiments carried out to study the first formation's steps were based principally on dust. In fact, there is a key ingredient that at least experimentally, has been poorly considered in terms of planet formation: Water. Water is the most abundant molecule in the Universe after Hydrogen (H_2) and consequently its presence in protoplanetary discs should not be ignored. The presence of water molecules has been detected in the following extraterrestrial environments:

- Solar system objects.
- Interstellar dark clouds (e.g. Gillett and Forrest, 1973; Leger et al., 1979).
- Protoplanetary discs (e.g. Terada et al., 2007; Honda et al., 2009; Riviere-Marichalar et al., 2012).
- Exoplanets (e.g. Tinetti et al., 2007; Beaulieu et al., 2010).
- Active Galaxy Nuclei NGC 3079 (Humphreys et al., 2005) and Quasar APM 08279+5255 (Lis et al., 2011; Bradford et al., 2011).

These observational constraints show us that water exists overall the cosmos, implying an evident but still unknown role on planet formation. Not only water and water ice implications are not clear, even the origin of water itself is still under study. It is believed that most part of the existing H_2O is synthesized via grain-surface reactions at around around 10 K temperatures (e.g. Miyauchi et al., 2008; Ioppolo et al., 2008; Tielens, 2010). This is the conclusion to which has been arrived after

comparing the observed water ice abundance in interstellar clouds and the predicted much lower abundance resulting from gas-phase reactions (e.g. D'Hendecourt et al., 1985; Hasegawa et al., 1992). Most part of the water present in a PPD is previously formed in molecular clouds via grain-surface reactions (van Dishoeck et al., 2014). However, this abundance of water may vary depending on its formation *in situ* through hot gas reactions (Glassgold et al., 2009; Meijerink et al., 2012) or its destruction due to X-ray and UV radiation (Stäuber et al., 2006).

It is unavoidable to take into account the influence that water may have during the first phases of planet formation. In most astrophysical scenarios, water may be found in gas or solid state due to temperature and pressure conditions. If the distance to the central forming star is large enough, the temperature will be low enough to find water in solid state. If any icy body crosses this limit towards the star -known as "Snowline"-, the containing water will sublimate into gas. Nonetheless, it is believed that water should be present in liquid state in some extraordinary conditions such as the surface and subsoil of earth-like planets like Mars (Renn et al., 2009) or under the crust of some icy moons (e.g. Europa and Enceladus) or even asteroids (Zolensky, 2010).

Studies related to water and water ice in PPDs (i.e. to planet formation) started at the end of the eighties (Stevenson and Lunine, 1988) while some contributions were done during the nineties (e.g. Lichtenegger and Komle, 1991; Stepinski and Valageas, 1997; Cyr et al., 1998). During the last decade the number of papers related to this topic increased, in part due to the discovery of many exoplanetary systems. A complete review can be read on Ciesla and Cuzzi (2006). Besides classical coagulation via hit-and-stick processes that are assumed to happen in the disc (Dominik and Tielens, 1997; Wada et al., 2007), recently deeper studies appeared regarding to physical effects which could affect the growth of dusty and icy bodies, like condensation (Ros and Johansen, 2013), sublimation (Machida and Abe, 2010; Saito and Sirono, 2011) and sintering (Sirono, 2011a,b).

Although the theoretical comprehension of these processes has recently raised, there are just a few experiments being made upon them (e.g. Kato et al., 1995; Bridges et al., 1996; Arakawa, 1999; Heißelmann et al., 2010; Gundlach et al., 2011; Aumatell and Wurm, 2011b; Shimaki and Arakawa, 2012; Aumatell and Wurm, 2014). In this thesis I will contribute to a better understanding of these processes, specifically on how ice affects the first stages of planet formation from an experimental point of

view.

Chapter 2

Theory of Planet Formation

Much progress has been made on how planets form. Although most astrophysicists widely agree, many details about it remain unknown. Many theories have been proposed to explain the actual picture of our solar system (Williams and Cremin, 1968), but after the discovery of planets orbiting around other stars, the most accepted standard theory nowadays has become the so called "Nebular Hypothesis" . It is assumed to take place in every planet forming scenario throughout the whole Universe.

2.1 The Nebular Hypothesis

Immanuel Kant in 1755 - and again independently Laplace in 1796 (Jeans, 1919)-, proposed the nebular hypothesis as a consistent theory for the origin of the solar system. However, it was not imposed as the most accepted model until last century with the main contribution of V. Safronov with an important paper (Safronov, 1966). The global argument of the nebular hypothesis maintain that the Sun and all the planets and bodies that orbit it, originated from a mutual giant cloud of dust and gas that gradually collapsed forming a central protosun surrounded by a disc made by gas and dust. That surrounding disc, known as Protoplanetary or Cricumstellar disc, contained all the actual Solar System members' material. Through different physical processes (which take place on over 13 orders of magnitude in size - from dust to planets) this material evolved into the actual picture of the Solar System. This general overview is nowadays not only valid for our Solar System but also

applicable to exoplanets and exoplanetary systems.

Although the global picture of planet formation has not drastically changed since the acceptance of the nebular hypothesis, much improvement has been made in order to explain the vast variety of existing planets and planetary systems. These improvements are focused on a deeper understanding of the large number of different phenomena that exist during the whole planet formation and evolution processes. Depending on the physical and chemical conditions, different phenomena will determine how the system evolves. In order to analyse which ones rule the evolution of the given system, it is convenient to divide these processes into different stages according to astronomical observations of the so called "Young Stellar Objects" (YSO from now on).

2.1.1 Young Stellar Objects

YSOs, like T Tauri stars or Herbig stars, emit orders of magnitude more infrared (IR) radiation than a typical main sequence star (Gillett, 1986). This excess of radiation is associated to the surrounding dust grains, which absorb part of the star emission and reradiate it at longer wavelengths. This radiation can be observed and characterized by their Spectral Emission Distribution (SED). As YSOs evolve, the surrounding envelope will fall into the star and into the forming disc. This evolution can be observed in their SEDs as well. Making use of these observational constraints, YSOs are classified into different classes, based on the slope of the SED between 2 and 25 μm IR wavelengths (Lada and Wilking, 1984; Andre and Montmerle, 1994),

$$\alpha_{IR} = \frac{d\log \nu F_\nu}{d\log \nu} = \frac{d\log \lambda F_\lambda}{d\log \lambda}. \tag{2.1}$$

Each YSO evolution stage is characterized by their own physical processes. Some of these processes can take place at more than one stage but at different disc's locations (Roberge and Kamp, 2011). Following spectral criteria from eq 2.1, the below presented one is the most accepted YSO classification nowadays (Natta,1999):

i CLASS 0: A slow rotating dense molecular core collapses. A central protostar and an enveloping disc made of dust and gas are formed. A persistent infall of gas and dust embeds the system.

ii CLASS I: The embedding material falls into the star through the disc forming a bipolar outflow. Absorption lines produced by the surrounding dust and gas are visible through SEDs.

iii CLASS II: Much of the initial surrounding material amount has been dissipated by stellar winds. The protostar is surrounded by an optically thick circumstellar disc and the material infall ends. It is believed that effective planet formation takes place during this phase.

iv CLASS III: Almost no excess of IR emission is observed, indicating the presence of an almost zero main-sequence star at the center. A disc of debris orbits the star that will dispersed by various physical processes (Hollenbach et al., 2000).

Exists a complementary YSOs classification which uses the star's accretion rate as a classification criterion. Basically, this method classifies T Tauri stars froom classical and weak-lined. (Williams and Cieza, 2011). While classical T Tauris (CTTS) are characterized by their strong Hα and UV emission, weak T Tauris (WTTS) have very low or no accretion's signatures.

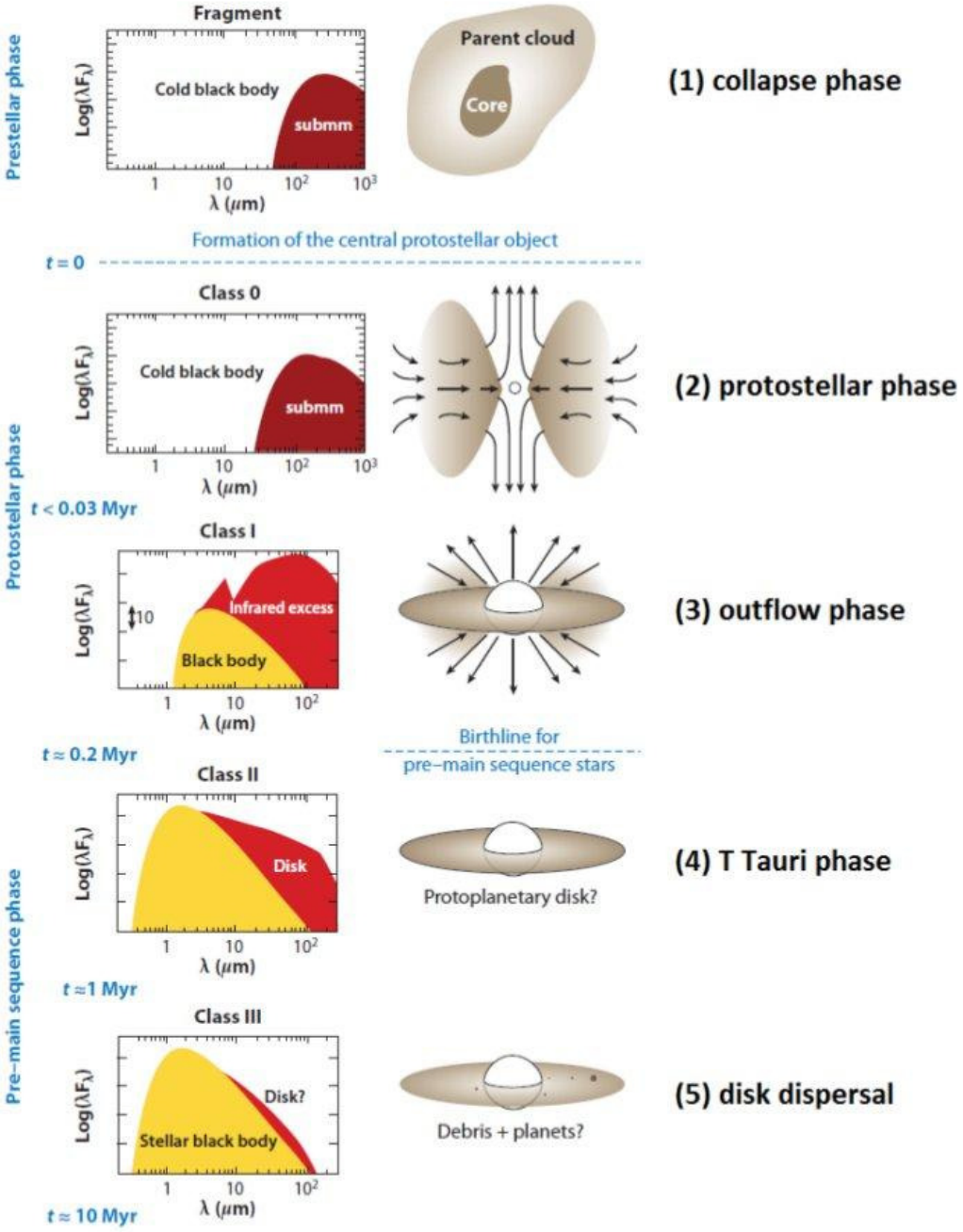

Figure 2.1: Extracted from Andre (2011). Empirical sequence for the formation and circumstellar evolution of a single star from a prestellar cloud core to a Class III young stellar object, based on the shape of the spectral energy distribution (left), the bolometric temperature and the mass of circumstellar (envelope + disk) material indicated on the right (From Lada (1987); Andre et al. (1993, 2000); Myers et al. (1998)).

2.1.2 Circumstellar Discs

As it has been mentioned in the previous YSO classification, planetary bodies start their formation during the Class II phase and as the YSO evolves, the circumstellar disc will acquire different properties. In a similar way, a classification of discs can be established depending on their SED features. If we imagine the disc as an addition of annuli of different radii, each of one having a different local dust temperature that depends basically on their distance to the central star and considering that they emit as blackbodies, the total flux of the disc may be calculated like (Beckwith et al., 1990):

$$F_\nu = \frac{\cos\theta}{D^2} \int_{r_{in}}^{r_{out}} B_\nu(T_d) \left(1 - e^{-\tau_\nu}\right) 2\pi\, r\, dr \tag{2.2}$$

taking with θ as the disc's inclination to the line of sight; D, the distance to the observed disc; $r_{\rm in}$ and $r_{\rm out}$, the radii from the inner and outer parts of the discs respectively; B_ν, the Planck function for dust as blackbody emitter at a temperature T_d. In eq. 2.2, the dust optical depth can be substituted by:

$$\tau_\nu = \frac{\kappa_\nu \Sigma_d(r)}{\cos\theta} \tag{2.3}$$

where κ_ν is the dust opacity per unit mass and $\Sigma_d(r)$ is the dust's surface mass density. If the distance D to the disc is known, its luminosity L can be calculated. The ratio $L_{IR}/L_\star$, where $L_\star$ is the total luminosity of the star and L_{IR} is the re-emitted IR radiation absorbed by the dust grains, is used to classify the circumstellar discs. Depending on the ratio's value, 3 classes are defined:

- **Primordial discs**: they are associated to Class II YSO. Accretion of disc material onto the star is a common feature of primordial discs. H_2 and CO lines show that they are gas rich and optically thick (Thi et al., 2001), assuming a gas-to-dust ratio of 100:1 like in the interstellar (IS) clouds (e.g. Kerr and Knapp, 1974; Hogerheijde, 2010). A commonly well accepted value for the Primordial disc's lifetime is $\sim$ 6 Myr (Haisch et al., 2001), but depending on the star type around which the disc rotates and the star's vicinity, its lifetime may vary significantly (Mamajek, 2009). Although gas accretion contributes to the infared emission, it is assumed that primordial discs reemit a $L_{IR}/L_\star \sim$

$0.1 - 0.2$ from the absorbed star radiation (Roberge and Kamp, 2011).

- **Transitional discs**: the main feature of these discs is the absence of IR radiation excess at short wavelengths. This would imply that the inner regions of the disc should be optically thin. There are plausible explanations about the cause of this optical depth decrease. The coagulation of sub-micrometer dust particles to protoplanetary bodies (Strom et al., 1989), together with photoevaporation and viscous accretion (Clarke et al., 2001), would form an inner gap where the IR emitting material would be removed. Typical timescales for transitional discs phase are ≈ 1 Myr (Currie et al., 2009), but some observations show that they could be even shorter in time (Currie and Kenyon, 2009). For transitional discs $L_{IR}/L_\star \lesssim 0.1$.

- **Debris discs**: these discs are the following phase to transitional discs. They surround stars that are already in the main sequence and with ages between some Myr to stars older than our Sun. Anyway, most of them are found around stars that are no older than 1 Gyr (Su et al., 2006). They have much lower amounts of gas (if they have) in comparison with the previous two phases. Another property of debris disc is their low amount of dust, setting the $L_{IR}/L_\star$ ratio to $\lesssim 3 \times 10^{-3}$ and going down to the detection limit of actual equipment. It is believed, that this dust is the result of interactions between the protoplanetary bodies which populate the debris discs and the present physical conditions (collisions, evaporation). This conclusion arises from the fact that the dynamical lifetimes of the dust grains in the disc are shorter than the stellar ages (Gillett, 1986). Undoubtedly, in debris discs there are already planetary bodies with typical planetary masses. Some of them have been detected by direct imaging and it has been recently proposed by Su and Rieke (2013) to organize the debris disc extension into 5 differentiated regions depending on the ongoing processes.

It must be noticed that, although the features between different types of discs are very clear, it is not still well known how each class of disc evolves in order to become part of the following class. Not all primordial discs will suffer the same phenomena at the same time under the same conditions. The observation of the maximum amount of selected objects and more sophisticated simulations will allow to better understand which processes take place in the discs.

2.2 Properties and Evolution of Protoplanetary Discs (PPD)

Making use of the "discionary" presented by Evans et al. (2009), a protoplanetary disc (PPD) is a primordial disc with the potential to form planets. In this work, I will consider a PPD as a circumstellar disc that surrounds a star which is found in the evolution state between the end of the Class I stage (Williams and Cieza, 2011) and its main sequence. Following this criterion, I will consider a transitional disc as a protoplanetary disc because, in addition to IR excess, the central star is still accreting part of the disc's gas (Najita et al., 2007).

PPDs are active hydrodynamical systems that evolve and suffer dramatic physical and chemical changes. That fact complicates the task for building a description that may fit every kind of PPD. In any case, there are some properties common in all of them that help us to understand the formation and evolution of the precursor bodies formed in their interior.

2.2.1 Mass

In order to know how much mass is required to build the planets that already have been detected, it is fundamental to estimate the amount of gas and dust necessary to build them. Although PPDs masses have already been estimated before the first confirmed detection of an extrasolar planet around a main sequence star (Beckwith et al., 1990), we just had our solar system to test the required initial mass to build a planetary system.

Weidenschilling (1977) and later Hayashi (1981) tried to answer this question by introducing a Minimum Mass Solar Nebula model (MMSN) that is still considered valid in modern theories. Hayashi (1981) suggests that the surface mass distribution along the disc should follow the relation:

$$\Sigma(r) \approx 1700 \left(\frac{r}{1\,\mathrm{AU}}\right)^{-3/2} \mathrm{g\,cm^{-2}} \tag{2.4}$$

with r being the distance to the Sun.

Assuming that the nebula has an extension between 0.3 and 30 AU, its total mass can

be estimated integrating eq. 2.4, giving as result 0.013 $M_\odot$. This is ~ 10 times the total mass of all the solar system bodies (excluding the Sun). If the MMSN model is correct, it would mean that most part of the initial mass forming a PPD is ejected to the ISM with no contribution to the final mass of the system. It must be pointed out that this model is based on our solar system and, therefore, it just considers Sun-like star types. Around 10% of the detected extrasolar planetary systems contain a Sun-like star (Johnson, 2009), and many of them contain much more massive planets than Jupiter, implying that the minimum mass required for their formation should be higher. More elaborated models which consider dynamical processes like viscosity and planet migration have demonstrated that the MMSN model is applicable under specific circumstances and considerations (Davis, 2005; Desch, 2007) and introduce a surface mass distribution that does not follow a $\Sigma \propto r^{-1.5}$ relation. In any case, the final result for the minimum mass for these models does not vary drastically in comparison to the one presented by (Hayashi, 1981).

If we assume that PPDs will lately become planetary objects around a main sequence star, another way to deduce the required mass to form a planetary system is to estimate it from PPD observational data. An effective method to do it is from dust's (sub-)millimeter wavelengths observations (Williams and Cieza, 2011). For dust, the Planck function falls into the Rayleigh-Jeans regime $B\nu \approx 2\nu^2 kT/c^2$ and the temperature dependence of the emission is linear. However, the mass determination is not trivial and some difficulties are associated to it (Roberge and Kamp, 2011):

- **Optical depth effects**: For low dust densities the optical depth τ_ν will be also low. That means the term $(1 - e^{-\tau_\nu}) \approx \tau_\nu$ in eq. 2.2. These conditions correspond to an optically thin scenario and assuming that all the dust is at the same temperature, eq. 2.2 can be written as:

$$F_\nu \approx \frac{\kappa_\nu}{D^2} B_\nu(T_d) \int_{r_{in}}^{r_{out}} \Sigma_d(r) 2\pi\, r\, dr \tag{2.5}$$

  If we define M_d as the total disc dust mass for the integral term from eq. 2.5, it may be estimated as:

$$M_d = \frac{F_\nu D^2}{\kappa_\nu B_\nu(T_d)} \tag{2.6}$$

  As dust is just a minor part of the initial total mass from a protoplanetary

disc, it is necessary to establish a relation between the dust-gas ratio in order to know its whole mass (see below). Although (sub-)millimeter wavelengths seem to be the optimal range to estimate the disc mass (not only because of the linear emission dependency with the temperature but also because at shorter wavelengths than 100 μm the emission form PPDs is optically thick (Beckwith et al., 1990)), the innermost regions of the disc may also be optically thick at (sub-)millimeter ranges (Roberge and Kamp, 2011).

- **Gas mass measures**: to date it is very difficult to estimate the gas mass of a PPD from its observation data. This assumption that the gas-dust ratio (100:1) would only be applicable to youngest primordial discs since disc suffer gas depletion during their evolution. The estimation of gas-dust ratio is extremely significant because errors in the dust mass determination turn into larger uncertainties for the gas and, therefore, total disc mass determination.

- **Emission dependence on dust grain's size**: as the maximal emission efficiency is achieved when grains are the same size of the emission wavelength and the longest observable ranges lay on the millimetre to a few centimetres region, when the aggregates' typical radius is larger than these sizes, they become undetectable. The main issue related with this fact is that these aggregates contain most of the solid mass in the PPD.

2.2.2 Radius and Structure

The disc size can be determined by multiple wavelength emissions. However, outer regions are cool and emit low intensity radiation, therefore it's difficult to establish an exact radius value. Some studies present disagreements between dust thermal continuum emission and the CO gas emission counterpart. Piétu et al. (2005) found that dust from protostar AB Aurigae was detectable at radii of 350 ± 30 AU and CO at distances of 1050 ± 10 AU, while Isella et al. (2007) estimate a dust emission extension of 200 ± 15 AU and CO emission up to 540 ± 40AU for HD 163296. These discrepancies may be originated by the choice of a specific disc-structure model that may affect the final value of the radii estimations (Hughes et al., 2008). Another method to measure the PPD size is the observation of its silhouette resulting from the light absorption from a background source. This method has been applied to estimate the sizes of several discs in the Trapezium Cluster in the Orion constellation,

concluding that at least 40% of the measured objects are larger than 50 AU (Vicente and Alves, 2005). It is noticeable that no relation between disc radius and star mass have been found (Vicente and Alves, 2005).

While protoplanetary discs are dynamic objects, different processes define its shape and inner structure. It is widely accepted that PPDs are not completely flat, but they flare as radial distance to the central star increases (Kenyon and Hartmann, 1987). This feature was introduced to explain the excess of radiation detected from face-on discs and it was observationally constrained by edge-on objects like IRAS 18059-3211 (also known as Gomez's Hamburger) (Noll, 2000; Bujarrabal et al., 2009) or the HH 30 (Cotera et al., 2001).

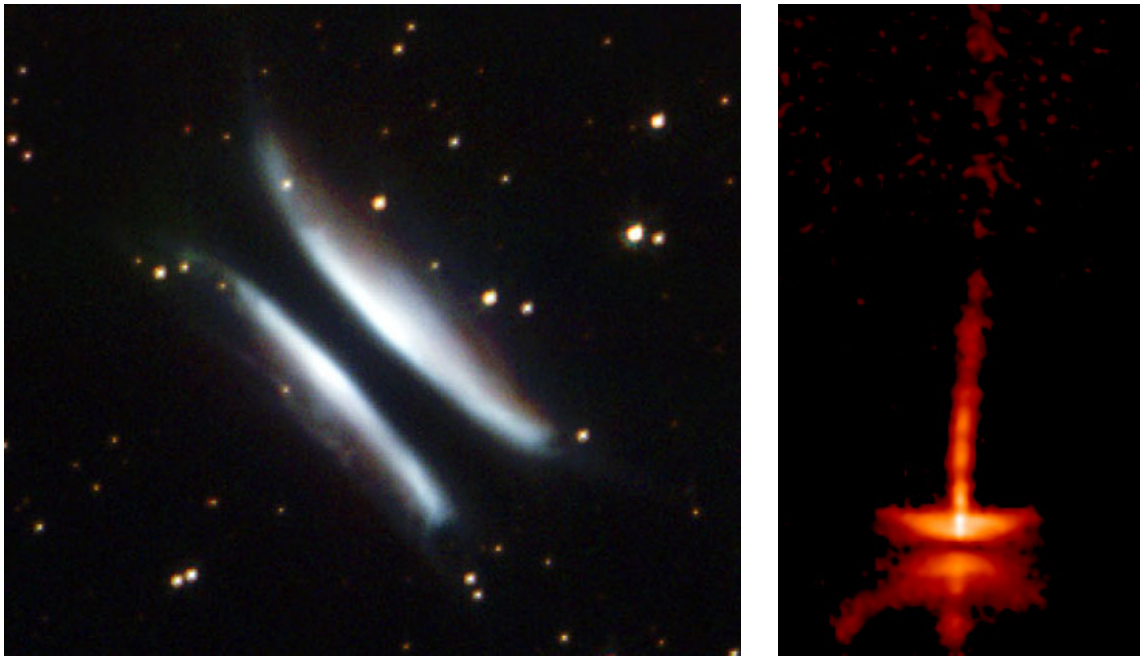

Figure 2.2: Captures of IRAS 18059-3211, "Gomez's Hamburger" (left) and HH 30 (right) obtained by the Wide Field Planetary Camera 2 of Hubble Space Telescope.

Although in first approximation we can assume PPD's as two dimensional structures (flat discs), actual models contemplate its three dimensional nature and study their physical properties considering a vertical and radial components at the same time that azimuthal symmetry is accepted.

Assuming that the disc is in hydrostatic equilibrium, the density profile can be written as (Williams and Cieza, 2011):

$$\rho(r,z) = \frac{\Sigma(r)}{\sqrt{2\pi}H} \exp\left(-\frac{z^2}{2H^2}\right) \tag{2.7}$$

where r is the radial distance to the star; $\Sigma(r)$ the surface density; z the distance to the mid-plane; H is the scale height, defined as $H = c_s/\Omega$, with $\Omega = \sqrt{GM_\star/r^3}$), c_s the sound speed, G the gravity constant and $M_\star$ the star's mass. Equation 2.7 shows a first impression on how the disc is structured in the vertical direction. It can be seen that the density decreases as we move away from the star and the mid-plane. The surface density profile $\Sigma(r)$ plays a crucial role in this assumption. Basic surface mass distributions like in equation 2.4 applied to equation 2.7 gives us a quick idea of how the mass is distributed along the disc radius. However, more sophisticated models are used to obtain more realistic results (Hartmann et al., 1998; Masset et al., 2006).

The radial structure of the disc is mainly defined by the radial force balance. As mentioned, gas is under the influence of difference forces and it presents diffusion along the radial direction. At first approximation it may be written as:

$$\frac{\partial \Sigma}{\partial t} = \frac{3}{r}\frac{\partial}{\partial r}\left[r^{1/2}\frac{\partial}{\partial r}\left(\Sigma\nu r^{1/2}\right)\right] \tag{2.8}$$

where ν is the gas viscosity defined by $\nu = \alpha c_s H$. Here α is the turbulence parameter which value uses to be much less than 1 (Ruden and Pollack, 1991). The model that assumes a viscosity ruled by the commented parameter is commonly known as α-model. Although most of PPDs models assume a simple flared structure, more sophisticated ones have been developed to explain multiple possible shapes according to discs' SED observations (Dullemond and Dominik, 2004)

Considering the multiple physical conditions to which the disc is subjected, several outer and inner regions may be defined. Local temperature is a key physical parameter that determines which processes are going to take place in a certain disc region. Temperature is the main physical parameter that determines where the different disc components solidify. Up to a distance of ~ 0.1 AU from the star, temperatures are so high that all material is found in gas phase. As long as we move away from the star, different materials condensate depending on their solidification temperature. Beyond 0.1 AU, refractory material solidifies (~ 1500 K) and at higher distances from the star, water condensates ($\sim 150 - 170$ K) increasing considerably

the concentration of solid material. The distance at which this effect takes place is known as sonwline and particularly, for the solar nebula, it was situated at 2.7 AU (Hayashi, 1981). A deeper study on the snowline and water ice in PPD is described in chapter 4.

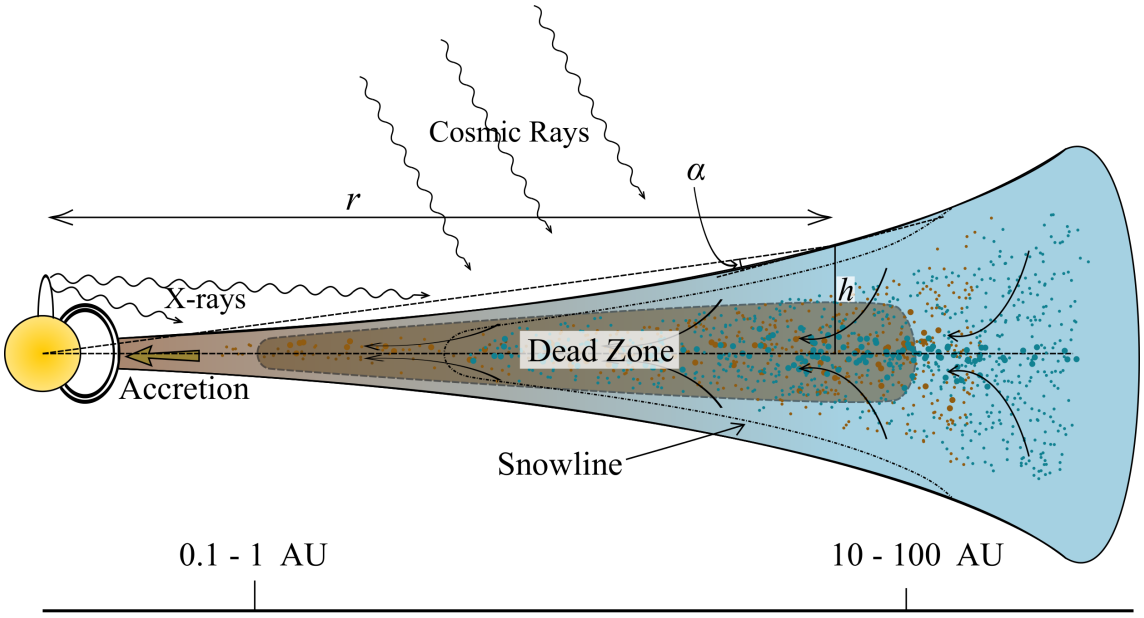

Figure 2.3: Sketch of a flared protoplanetary disk structure. In this figure different parameters are shown for a certain point on the disc surface: r is the distance to the star, h is the distance to the midplane of the disc and α is the angle between the tangent inclination of the disc at the considered point and the line that points toward the center of the star. The brown region corresponds to the "Dead Zone" and the discontinuous line represents the snowline (see description in the text). The surface of the disc is affected by local stellar radiation like X-rays and cosmic rays coming from external sources.

Ionization plays also an important role on the gas distribution in the disc. Though the global disc temperature is too low to ionize the gas thermally, close to the star ($<$ 1 AU) temperatures are high enough to ionize some metals (Armitage, 2010) and, therefore, the embedding gas by ionization balance. Ionized material may couple to the star's magnetic field and, since the disc has viscous properties, turbulences are originated by magneto rotational instabilities (MRI) (Balbus and Hawley, 1991). The disc becomes also partially ionized by nonthermal processes like: X-ray absorption coming from the central star; X-ray and cosmic rays coming from external sources (like other stars, supernovae and Active Galaxy Nuclei (AGN) among other sources) and by radioactive decay of short-lived nuclide. However, PPDs are globally weak ionized and in some regions of the disc, specially where dust

is more abundant, resistivity is so high that MRI decays until turbulence ceases. The region where no MRI take place is known as "Dead Zone" (see figure 2.3).

2.2.3 Planet Formation

During the formation of the first planetesimals, accretion onto the central star causes mass loss of the disc. Accretion rates at primordial ages are estimated to be $\dot{M} = 10^{-7} - 10^{-8} M_{\odot}$ yr^{-1}, but its value varies depending on the star's mass and decays with time (Hartmann et al., 1998). The material that falls onto the star is replaced by other material coming from outer regions. The disc, initially flared, becomes flatter and expands up to several hundreds AU. At the same time, energetic radiation coming from the star, mostly ultraviolet (UV) and higher energetic photons, interact with the disc material causing mass loss by photoevaporation at a $\dot{M} \sim 10^{-9} - 10^{-10} M_{\odot}$ yr^{-1} rate (Williams and Cieza, 2011). The material replacement coming from outer parts of the disc stops when accretion rate drops the photoevaporation rate, causing the formation of an inner hole of a few AU in radius. Once the inner gap is formed, the incoming flow from outer regions material is no longer viable. For the gas, higher phoevaporation rate counteract accretion rate, but for solid particles effects like radiation pressure or photophoresis (Krauss and Wurm, 2005) may force inner material to move outwards.

In a primitive protoplanetary nebula, sub-micrometer solid particles are completely coupled to the gas. Brownian motions produce relative velocities of the order of mm/s to cm/s between grains (Blum et al., 1996; Dominik et al., 2007). Due to these relative velocities, collisions between the grains will occur unavoidably sooner or later leading to aggregation. This hit and stick process causes the formation of larger bodies which have a higher surface-to-mass ratio and therefore, grains decouple from the gas (Weidenschilling, 1977). Once decoupled, the particles and the gas will move at different velocities around the star. Due to the gravitational pull of the star and the mid-plane of the disc, the aggregates settle down to the center of disc increasing the density in this region enhancing grain growth. The gas orbits around the star at sub-Keplerian velocities since pressure and centrifugal force compensate the gravitational pull. Although the grain decouples from the gas, its movement will be still affected by friction.

How exactly the first planetesimals grow up to larger sizes is still under debate.

There are 2 main mechanisms that are specially considered: collisional growth and gravitational instabilities.

Collisional Growth

The collisional mechanism seems to be efficient up to meter sized bodies, but in some simulation models eg. (e.g. Brauer et al., 2008) two main problems seem to stop the growth rate. This issue is known as the "meter barrier".

- Since gas moves at sub-Keplerian velocities, its friction with the solid bodies will affect their velocity enhancing their radial component. This leads to a radial drift (see section 3.2) that will depend basically on the size of the grains and the density of the gas. The gas-grain friction time may be written as (Blum et al., 1996):

$$t_f = \frac{m}{A}\frac{\epsilon}{\rho_g v_{th}} \tag{2.9}$$

  where m is the solid particle mass; A its geometrical cross-section; $\epsilon = 0.68$ an experimental constant; ρ_{g} the gas density and $v_t h$ the mean thermal velocity of the gas molecules. When planetesimals are a meter size, their drift towards the star is so fast that they are destroyed before further growth could occur (Klahr and Bodenheimer, 2006). In fact, starting at 1 AU a meter sized solid would be destroyed by the stellar ablation in less than 100 years.

- In first instance, meter sized bodies sticking efficiency is too low to reproduce the growth rate required to form planets in the considered timescales. This issue is known as the "bouncing barrier" (see e.g. Güttler et al., 2010; Kelling et al., 2014). However, experimental studies like Teiser and Wurm (2009b) and theoretical models like Windmark et al. (2012) suggest that even large bodies at high collision velocities could lead to net growth.

Collisional processes as growth mechanism is shown in more detail in chapter 3.

Gravitational instabilities

Although turbulence was introduced in theoretical models as a dispersal process, recent models based on this phenomena predict the formation of clumps in the disc. In these clumps the concentration of solid particles would be 80 times higher as the typical gas to dust ratio on large scales of the turbulence (Johansen et al., 2006) or even 10^3 on small scales (Cuzzi et al., 2008). How turbulences are originated in the PPD is not totally clear. The above mentioned MRI, are believed to be one of the main causes of this phenomena eg. (Kretke and Lin, 2010). Ionized gas in the disc could be coupled to weak disc magnetic fields. Due to the differential rotation nature of the disc, magnetic field lines are distorted and at the same time they induce a restoring force (Balbus and Hawley, 1991). The resulting angular momentum generated in this way in inner regions of the PPD is transferred to outer regions affecting the evolution of the whole disc (e.g. Armitage, 2011). Streaming instabilities are thought to contribute to solids' concentration as well, forming clusters with such densities that they would start accrete material by self gravity with timescales shorter than radial drift timescales. Both processes (turbulence and streaming instabilities) are the main contributors of the so called gravoturbulent planetesimal formation (Klahr and Johansen, 2008; Dittrich et al., 2013).

In the next growth phase, where Km sized planetesimals grow up to sizes of a few thousands of Km, gravity becomes the dominant force in the disc. However, gas drag still influences the dynamics of planetesimals. It is very difficult to know exactly how the following growth process occurs. A common assumption is that a large body grows by collisions with smaller planetesimals (Goldreich et al., 2004). Then, the small bodies would suffer three main interactions: 1-collisions between them; 2-gravitational attraction and collision with the larger object (what increases the random velocity of the minor bodies) and finally 3-the friction with the gas (what causes a decrease of the random velocity). At that point takes place the so called "runaway" growth regime, where accretion rate is proportional to the radius as R^4 and larger bodies grow much faster than smaller ones. This produces a population detachment between protoplanets and minor bodies (Weidenschilling et al., 1997). The increase of random velocities of smaller bodies slows down the growth rate, leading to a lock-step growth known as "oligarchic mode". However, the growth process from planetesimals to protoplanets present some uncertainties that difficult the exact comprehension of the processes. (For example, initial conditions are not

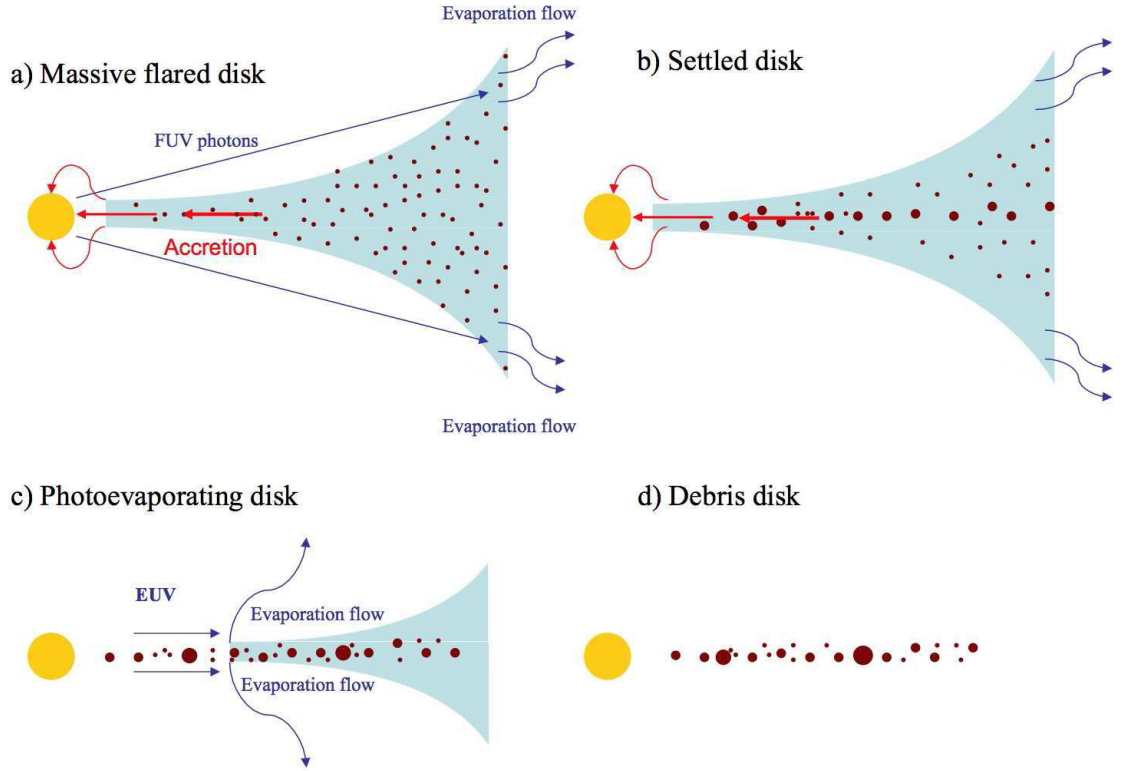

Figure 2.4: Evolution of a typical disc according to Williams and Cieza (2011). The gas distribution is shown in blue and the dust in brown. (a) During the first stage, the disc loses mass through accretion onto the star and FUV photoevaporation of the outer disc. (b) Solid grains grow into larger bodies that settle to the mid-plane of the disc. (c) Disc's mass and accretion rate decrease. EUV-induced photoevaporation becomes important. An inner hole is formed, accretion onto the star ceases, and the disc quickly dissipates from the inside out. (d) Once the remaining gas photoevaporates, the small grains are removed by multiple processes. Large grains, planetesimals, and/or planets are left.

well known; precise simulations require high computational power; in collisions of Km sized solids there are involved processes like shock waves, fracturing and multi-phase fluids dynamics).

Basically two types of planets result from the whole growth process: Gas giant planets or Terrestrial planets.

- **Gas giant planets**: They are characterised by their gaseous composition and by being more massive and larger than terrestrial planets. There are two models concerning the evolution of a protoplanet into a gas giant planet phase. The so called "Direct Gravitational Collapse Model" maintains that giant planets form directly from a gravitationally bound clump originated in

the PPD. The gravitational collapse occurs if the self-gravity of a disc's region is important compared to the gravity produced by the central star (D'Angelo et al., 2011). At the same time, the isolation of the clump from the rest of the disc takes places if the "cooling" time-scale -on which the gas clump cools down and contracts- is short compared to the shearing time-scale. Otherwise the clump would be interrupted.

The so called "Core Accretion Model" assumes that the giant planet formation is divided into 4 steps: First, a solid core made basically of ice and rock grows via two-body collisions until its mass captures a significant amount of gas forming an atmosphere. During the second step, the energy coming from impacts of the core with other planetesimals and gravitational potential is released to the disc. During this phase, the core and the atmosphere gain mass until a critical mass is reached $M \sim 10M_{\oplus}$ leading to the so called "Runaway Phase". During this stage, the planet keeps growing in mass and size mostly capturig gas in a relative short time-scale $\sim 10^5$ yr. Finally, when the gas in planet's vicinity is exhausted (because of dissipation or by a gap opening), a cooling and quasi-hydrostatic contraction process takes place until its final state is reached.

- **Terrestrial planets**: The formation of terrestrial planets mechanism is quite similar to the core formation of giant planets' process, but the concentration of solids is significantly lower. That implies longer collisional time-scales and, therefore, slower protoplanet growth. Planetesimals grow through two-body collisions up to a few thousands Km in size. The dominant interaction between planetesimals is the mutual gravitational force, but the remaining gas in the disc produce a damping effect that lightly affects the planetesimals trajectory.

Chapter 3

Planetesimal Formation through Collisional Processes

This work focuses on the first stages of planetesimals formation. However, this chapter summarizes the physics of possible collisional processes that take place in PPDs. As mentioned before, coagulation and collisions are believed to be the main mechanisms that rule the particle growth from 0.1 μm grains up to a few or several thousand kilometre bodies. The nature of collisions are very different depending on the constituents' size scale. The result of collisions depends on the magnitude of the physical variables implied. These variables are essentially the relative velocity between the particles, their radius and cross section, the impact parameter and finally their mass and structure (composition, porosity and distribution of constituents).

3.1 Growth of First Solids

As it was mentioned in section 2.2.3, since at the first formation stages dust grains are coupled to the gas, their relative velocities are mainly driven by Brownian motions. In order to reproduce the very first stages of cosmic dust grains aggregation in PPDs, simulations and experiments take spheres as basic components. Hit-and-stick processes with such grains give as result aggregates which possess fractal structures. Therefore, average density and mass of the aggregates depend as a power law on the "fractal dimension" D_f (Wurm and Blum, 1998).

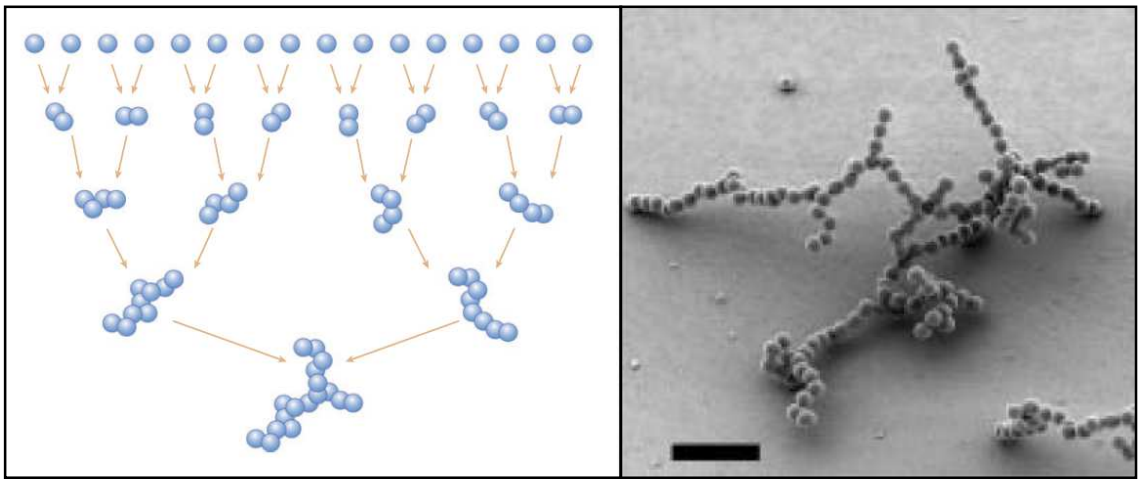

Figure 3.1: Left: Hit-and-stick collisions lead to formation of fractal aggregates (Blum and Wurm, 2008). Right: Scanning Electron Microscope capture of a monodisperse fractal agglomerate formed by spherical SiO_2 particles of 0.95 µm radius. The scale bar shows 10 µm (Blum and Wurm, 2000).

$$m(a) \propto a^{D_f} \tag{3.1}$$

where a is the size of a monomer. D_f have values between 1 (for long linear chains) and 3 (for a compact filled volume). Fractal aggregates generally have large surface-to-mass ratios (Dominik et al., 2007); that will play a fundamental role on the outcome of collisions and on the interaction of the aggregates with the surrounding gas (see eq. 2.9)

For two identic colliding fluffy aggregates which are µm to mm in size, four possible outcomes are possible (Dominik and Tielens, 1997). A graphic example is shown in figure 3.2.

1. Hit and stick: The aggregates collide and remain attached.
2. Restructuring: After collision, the aggregates remain stuck and monomers redistribute restructuring the whole resulting aggregate.
3. Mass transfer: Some monomers are detached after the collision, but the resulting aggregate is more massive than any of the pre-collision bodies.
4. Destruction: The result of the collision is the breakup of the colliding aggregates into smaller and lighter bodies.

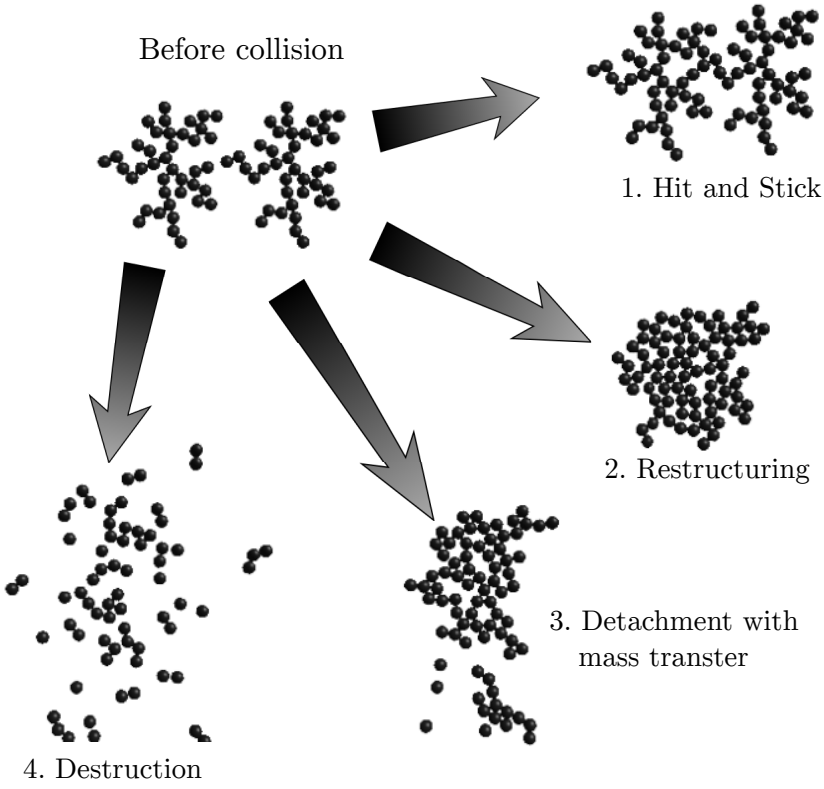

Figure 3.2: Simulation of the possible collisional outcomes of fluffy aggregates depending on the relative impact velocity. Individual grains is a 0.1 µm radius sphere (Dominik and Tielens, 1997)

.

The two main physical parameters involved in the outcome of such collisions are the relative velocity (or kinetic energy) before the interaction and the contact force between the aggregates' monomers. Attraction forces are present in the contact region where two spherical particles are touching. Generally these are Van der Waals interaction (for dust grains) or hydrogen bonds (for water ice) (Dominik and Tielens, 1997). The pull-off force necessary to separate the particles is (Johnson et al., 1971):

$$F_c = 3\pi\gamma R \tag{3.2}$$

where γ is the material surface energy and R the reduced radius $R = r_1 r_2/(r_1 + r_2)$, with r_1 and r_2 as the radius of particles 1 and 2 respectively. However, when restructuring takes place, other effects like rolling, twisting and sliding processes

between monomers must be considered. Relevant aspects related with this topic are deeper studied in chapter 5.

It is assumed that fractal geometry of the solids is conserved up to at least mm sizes (Wurm and Blum, 1998; Blum and Wurm, 2000; Wada et al., 2011). Some simulations have shown that even at high energy collisions, the fractal dimension of the outcoming aggregate is $D_f < 2.5$ (Tanaka et al., 2012). Suyama et al. (2008) suggest that shrinkage of fractal aggregates starts when they are centimeters in size and that meter sized planetesimals would have densities of $\sim 10^{-4}$ g/cm^3. However, this results are highly dependent on the material. Contact forces between water ice monomers are much stronger than the ones silica form, therefore the water ice aggregates tend to be fluffier than silica ones for the same collision energy.

As the size of the colliding bodies increases, the physics involved in the collision process gets more complex. The interaction between two identical aggregates helps us to understand the first steps of aggregation in a simple way. Let's assume that at a certain moment, there is a certain number of aggregates formed by i monomers in a fixed volume with a density n_i. How this density evolves with time can be estimated by the coagulation equation (Smoluchowski equation):

$$\frac{\partial n_i(t)}{\partial t} = \frac{1}{2}\sum_{j=1}^{i-1} A(i-j,i)n_{i-j}n_j - n_i\sum_{j=1}^{\infty} A(i,j)n_j \tag{3.3}$$

where $A(i,j)$ is the probability that two aggregates with i and j monomers stick together. Equation 3.3 is a very general formulation and may be applied to multiple scientific fields. The factor $A(i,j)$ depends on the physical context considered. In the context of planet formation, it may be written as (Armitage, 2010):

$$A(i,j) = P(i,j,\Delta v)\Delta v(i,j)\sigma(i,j) \tag{3.4}$$

with $P(i,j,\Delta v)$ being the probability that collisions between particle i and j results into adhesion, Δv is their relative velocity and σ is the cross section. Making use of equation 3.3 and considering a starting monodisperse distribution of 1 μm particles, 100 % of sticking efficiency and constant aggregate density over time, after 10^3 years some decimetre sized aggregates are formed and after 10^5 years all aggregates are at least millimetre size (Blum, 2004).

It must be noticed that these results are obtained under very general assumptions and that there are many aspects to be treated specifically in order to derive a more realistic aggregation's evolution.

3.2 Gas Drag

Since the gas-to-dust ratio is assumed to be 100:1 during the first planet formation stages in protoplanetary discs, solid particles' dynamics are strongly affected by their interaction with the gas. Depending on the relation between the particle radius ($a_{\rm p}$) and the mean-free path of the gas molecules (λ), two drag regimes are defined (Weidenschilling, 1977):

- **Epstein drag**: If $a_{\rm p} < \lambda$, then the gas drag force applied to a spherical particle is:

$$F_{\rm D} = -\frac{4\pi}{3}\rho_{\rm g} a_{\rm p}^2 v_{th}\mathbf{v} \tag{3.5}$$

  where $\rho_{\rm g}$ is the gas density; v_{th} the thermal velocity of the gas molecules and $\mathbf{v}$ the particle velocity.

- **Stokes drag**: When particles have grown enough to become larger than the gas' mean-free path ($a_{\rm p} > \lambda$), the drag force may be expressed as:

$$F_{\rm D} = -\frac{C_{\rm D}}{2}\pi a_{\rm p}^2 \rho_{\rm g} v\mathbf{v} \tag{3.6}$$

  being C_D the drag coefficient and v the gas velocity. The parameter C_D is a dimensionless coefficient that depends basically on the shape of the particle and on the so called "Reynolds number" $Re = 2a_{\rm p}v\rho_{\rm g}/\eta$, where η is the gas viscosity. For a spherical particle, the drag coefficient depends just on Re, and they are related as:

  $C_D \simeq 24/Re$, $Re < 1$

  $C_D \simeq 24/Re^{0.6}$, $1 < Re < 800$

  $C_D \simeq 0.44$, $Re > 800$

It can be seen that a transition between both regimes takes place at $a_{\rm p} = 9\lambda/4$.

A solid particle with a certain mass situated at a certain height from a non-turbulent disc's midplane and at a certain radial distance from the central star, will settle towards the midplane as (Armitage, 2010):

$$\frac{{\rm d}z}{{\rm d}t} = -\frac{\rho_{\rm m}}{\rho}\frac{a_{\rm p}}{v_{\rm th}}\Omega^2 z \tag{3.7}$$

where $\rho_{\rm m}$ is the particle density. Equation 3.7 shows the velocity of a particle which settles towards the midplane and it can be observed how it linearly increases with the particle radius $a_{\rm p}$.

As it has been commented in section 2.2.3, the gas drag forces solid particles to orbit around the central star at sub-keplerian velocities leading to a radial drift inwards. The radial velocity derived from this effect depends strongly on the particle size and on gas density. Using equation 2.9, we can define the friction stopping time as $\tau_{\rm f} \equiv t_{\rm f}\Omega_{\rm K}$ with $\Omega_{\rm K}$ as the frequency of an orbit completion at keplerian velocity. This allows to write the radial drift velocity as (Armitage, 2010):

$$v_r = \frac{\tau_{\rm f}^{-1} v_{\rm r,gas} - \eta v_{\rm K}}{\tau_{\rm f} + \tau_{\rm f}^{-1}} \tag{3.8}$$

where $v_{\rm r,gas}$ is the radial velocity of the gas. Since the gas friction time $t_{\rm f}$ depends on the gas drag regime and this gas drag depends on the particle size; the radial velocity has also a particular dependence on the particle size. For small particles where $\tau_{\rm f} << 1$ the radial velocity is almost $v_{\rm r,gas}$. For very large bodies where $\tau_{\rm f} >> 1$ the radial velocity increases linearly with the friction stopping time. In particular, Weidenschilling (1977) found that the maximum drift velocity takes place for bodies that are ~ 1 meter size.

Taking into account the different factors that affect the velocity of the solid particles, it is possible to compute the relative velocities between them depending on their sizes. PPDs models -already described above- show that it is possible to establish well defined ranges of relative velocities between aggregates depending on their sizes (e.g. Weidenschilling and Cuzzi, 1993; Windmark et al., 2012).

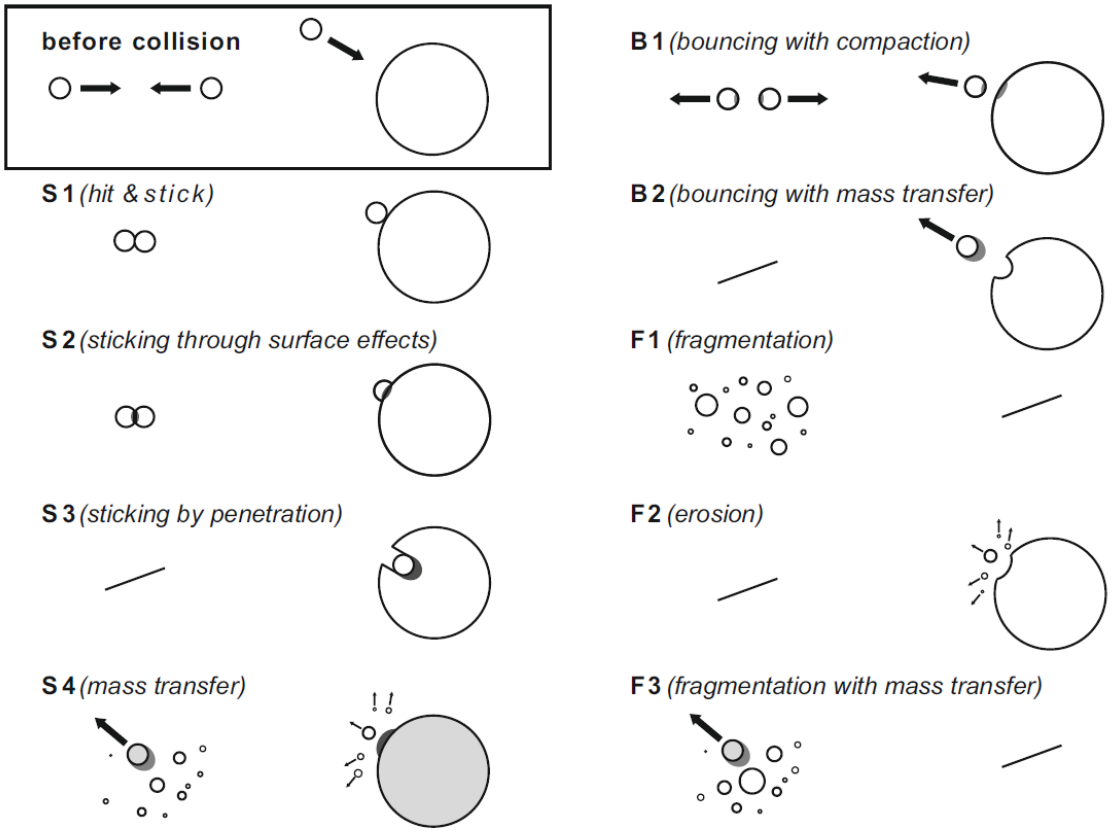

Figure 3.3: Possible two-body collisional outcome of experimentally observed according to Güttler et al. (2010). The result of the impacts are classified here as sticking (S), bouncing (B) and fragmentation (F) events. The solids that gain mass after an impact event are grey coloured.

3.3 Collisional Outcome

Growth based on hit-and-stick processes is assumed to be effective for small aggregates at low velocities with perfect sticking efficiency. However, if such conditions were constant, the disc would become optically thin after 1000 years (Blum and Wurm, 2008). This contradicts PPDs obsevations, which show that small particles are still abundant after a few millions years.

Fluffy aggregates become more compact after several collisions due to grain restructuring, reducing the sticky efficiency rate. At a certain point bouncing events are very common (Zsom et al., 2010; Kelling et al., 2014), and when colliding velocities are high enough, fragmentation takes also place (Blum and Wurm, 2000). Then, depending on multiple factors, different possible outcomes may arise from a two-body collision (see figure 3.3).

Although high velocity impacts may result on fragmentation, part of the broken aggregate may transfer part of its mass to the other body, leading to a net growth after a collision (Wurm et al., 2005) even at velocities of $\sim$ 50 m/s (Teiser and Wurm, 2009b). However, fragmentation is necessary in order to explain the number of minor bodies that crowd the solar system and to maintain the disc optically thick over millions of years (Dullemond and Dominik, 2005).

Since the number of physical parameters involved in two body collisions with solids larger than millimetre sizes is relative high, it is difficult to develop a theoretical model that describes this growth phase. In the last years much improvement has been done from a theoretic point of view (e.g. Schäfer et al., 2007; Zsom et al., 2010; Geretshauser et al., 2011; Meru et al., 2013). Although models are an important contribution on aggregation understanding, they must be supported by experimental counterparts. Several experimental studies have been done principally on dust aggregation (see e.g. Blum and Wurm, 2008; Güttler et al., 2010; Teiser et al., 2011; Weidling et al., 2012; Jankowski et al., 2012; Schräpler et al., 2012; Deckers and Teiser, 2013; Brisset et al., 2013). Figure 3.4 shows the possible outcomes from two body collisions depending on the relative velocity, the relative size difference and aggregate compaction.

The volume filling factor ϕ plays a crucial role on the possible collisions outcomes (Wurm et al., 2005; Beitz et al., 2011; Teiser et al., 2011; Meisner et al., 2012). Given a particular volume V, ϕ is defined as the ratio between the space filled by the solid particles inside V and the value of V:

$$\phi = \frac{\sum_i V_i}{V} = \frac{\rho_{\mathrm{agg}}}{\rho_{\mathrm{bulk}}} \tag{3.9}$$

where V_i is the volume of the i-th monomer; ρ_{agg} the aggregate's density and ρ_{bulk} the bulk density of the aggregate's material. The volume filling factor ϕ evolves with aggregates' collisions. Experimental works show that small quartz aggregates (µm - mm) the ϕ increases with the impact velocity (Teiser and Wurm, 2009a; Meisner et al., 2012).

The volume filling factor resulting from a collision does not only depend on the impact velocity. Re-accretion of detached particles after the impact results on a decrease of ϕ (Teiser et al., 2011). It has also been observed that ϕ varies with the monomer size: considering a specific velocity range, outcomes from aggregate's

collisions show that the larger the constituting monomers are, the more compact the resulting aggregate is (Meisner et al., 2012).

Even though experimental methods are limited to physical constraints, the evolution of the volume filling factor and its influence on collisional outcome are in good agreement with the above commented results (Geretshauser et al., 2010; Seizinger and Kley, 2013).

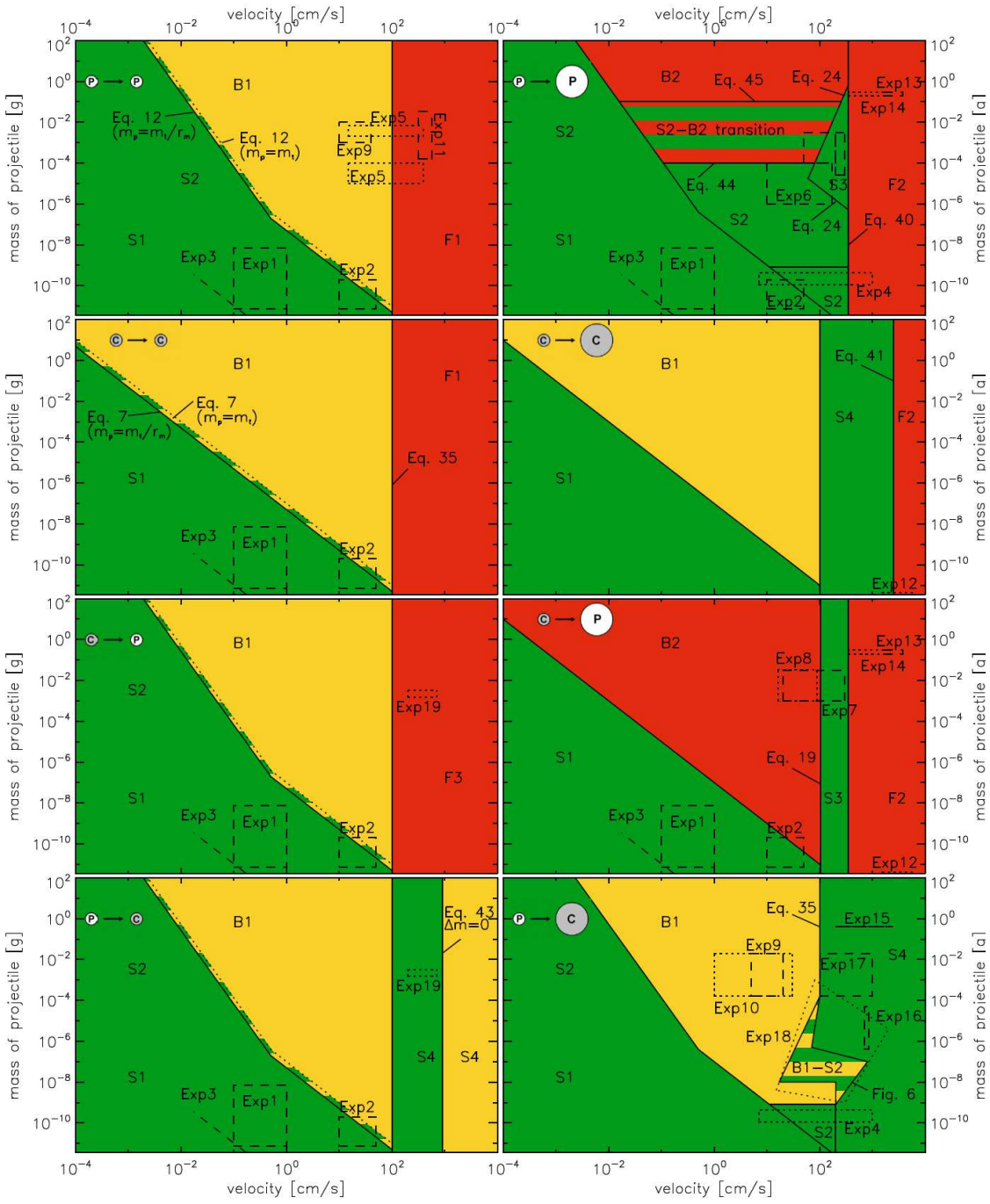

Figure 3.4: The resulting collision model, depending on the projectile mass and the relative velocity, according to Güttler et al. (2010). Similar-sized (left column) and different-sized (right column) collision partners are shown. They are either porous (P) or compact (C). Collisions within green regions can lead to the formation of larger bodies, while red regions denote mass loss. Yellow regions are neutral in terms of growth. The dashed and dotted boxes show where experiments directly support the model.

Chapter 4

Water Ice in Planet Formation

Oxygen is the most abundant element after Hydrogen and Helium in the Universe. Since water molecules contain hydrogen and Oxygen, it is expected that water should be a highly abundant molecule in the interstellar medium and, therefore, in proto-planetary nebulae. In addition to the already observed water presence in our solar system objects, H_2O has been already detected in gas phase in PPDs (e.g. Carr and Najita, 2008; Salyk et al., 2008; Riviere-Marichalar et al., 2012; Podio et al., 2013)) and in exoplanets (e.g. Barman, 2008; Brogi et al., 2013). Water in solid state has also been detected in PPDs (Terada et al., 2007; Honda et al., 2009). For these reasons, the role of water in planet formation cannot be ignored.

Dust is the main material present in the major part of sticking and coagulation models. However, the solid density is highly enhanced in regions where water and other volatiles condense (Stevenson and Lunine, 1988; Anders and Grevesse, 1989) and the opacity jumps up to almost a factor 5 (Podolak, 2010). In addition, dusty particles are covered by icy layers in theses regions, for this reason it is crucial to understand how icy surfaces interact during coagulation and collisional processes, in order to obtain more realistic models and results.

It has been suggested that water in PPDs could be formed through *in situ* chemical reactions (Glassgold et al., 2009), but it is assumed that almost the whole amount of H_2O contained in PPDs comes from interstellar clouds, where it is formed via grain-surface reactions (e.g. van Dishoeck et al., 2014). Since PPDs are optically thick during their first evolution stages, it is difficult to estimate the total amount of H_2O present in regions closer to the disc's mid-plane.

One of the most important aspects regarding the role of water ice in planet formation, is the sticking efficiency of icy grains. The presence of an icy layer around dust grains implies a more effective aggregation process because of its higher sticking efficiency (Bridges et al., 1996; Wang et al., 2005). Even if the collision does not yield to a sticking outcome, the energy loss after the impact is higher than in dust collisions. Contact between water ice covered bodies are ruled by dipole forces which are much stronger than the van der Waals forces between dust grains (Wang et al., 2005).

Like every known substance, water exists in different states of matter depending on its pressure and temperature. In protoplanetary discs it is found in gas or solid state. Just in special cases where temperature and pressure are suitable, water may be found in liquid state (e.g. Earth's surface, Mars and icy moons' subsoils), but those conditions are just reached once protoplanets and planets are already formed. The left side in figure 4.1 shows a general phase diagram of water with dependence on pressure and temperature. Water is only found in vapour phase in the PPD's regions close to the star. Water is present as solid ice in the rest of the disc, where temperatures and pressures are relatively low (some fraction of vapour coexists as well).

Under the conditions related to the present study, it is important to know the phase diagram of H_2O for temperature ranges between $10 - 200$ K, and pressures of $10^{-10} - 10^2$ Pa. The temperature T at which water sublimates (or condensates) in function of the pressure P may be estimated as (Wagner et al., 2011):

$$P_{\mathrm{subl}} = P_{\mathrm{t}} \exp\left\{\frac{T_{\mathrm{t}}}{T}\left[a_1\left(\frac{T}{T_{\mathrm{t}}}\right)^{b_1}\right]\left[a_2\left(\frac{T}{T_{\mathrm{t}}}\right)^{b_2}\right]\left[a_3\left(\frac{T}{T_{\mathrm{t}}}\right)^{b_3}\right]\right\} \tag{4.1}$$

where $P_{\mathrm{t}} = 611.657$ Pa and $T_{\mathrm{t}} = 273.16$ K are the pressure and temperature corresponding to the water's triple point, and a_i and b_i are dimensionless parameters with values: $a_1 = -21.2$, $a_2 = 27.3$, $a_3 = -6.11$, $b_1 = 0.00333$, $b_2 = 1.21$ and $b_3 = 1.70$. Equation 4.1 is valid for a 50 to 273 K temperature range with a lower than 5% uncertainty (Wagner et al., 2011). The phase diagram corresponding to the above mentioned ranges is plotted in the right side of figure 4.1.

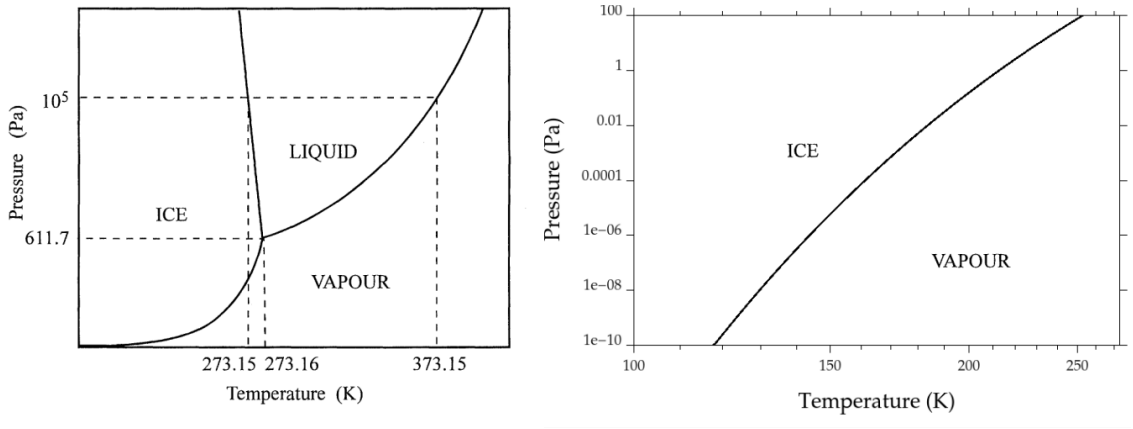

Figure 4.1: Left- Water phase diagram from Petrenko and Whitworth (1999). Right- Water phase diagram at very low pressures extrapolated from equation 4.1.

4.1 The Snowline

The Snowline is the virtual line that separates the region where water exists only in gas state from the region in which physical conditions enable its condensation (see Fig. 2.3). In most models, the snowline is considered just as a radial distance to the star at which the water freezes, and in the case of the solar nebula it is situated approximately at 2.7 AU (Hayashi, 1981). However, thermal and radiative processes on the PPD surface causes water in these regions to be found mainly in form of vapour, even at several AU from the central star (Meijerink et al., 2009; Min et al., 2011). Therefore, an *atmospheric* or *photospheric* snowline may be defined as the region that separates the water vapour layer from the water ice present in colder regions closer to the mid plane (Podolak, 2010; Ros and Johansen, 2013).

Since pressure in most regions of PPDs is far below the pressure corresponding to the critical point of water, temperature is the physical variable that rules the condensation of water into ice. The temperature at any point of a PPD can be estimated as (Podolak, 2010):

$$T^4(r) = T^4_{\rm rad}(r) + T^4_{\rm visc}(r) \tag{4.2}$$

where $T_{\rm rad}$ is the temperature induced by external radiation and $T_{\rm visc}$ the temperature caused by the viscous heating. For flared discs, the first member of the right side of equation (4.2) can be estimated as (Armitage, 2010)

$$T^4_{\rm rad}(r) = T^4_\star \left(\frac{R_\star}{r}\right)^2 \alpha \tag{4.3}$$

being $T_\star$ the temperature of the star's surface; $R_\star$ the star's radius and α, the angle between the incoming radiation and the tangent to the disc's surface at the required region (see figure 2.3). The second member on the right side of the equation (4.2), related to the viscous heating, is caused by the flux of material moving inwards due to the material accretion into the star and it may be calculated as

$$T^4_{\rm visc}(r) = \frac{3GM_*\dot{M}}{8\pi r^3\sigma}\left(1-\sqrt{\frac{R_*}{r}}\right) \tag{4.4}$$

where σ is the Stefan-Boltzmann constant.

According to equations 4.3 and 4.4, the snowline position depends strongly on the parameters chosen. For a star with $M_* = 0.5M_\odot$ and an accretion rate of $\dot{M} = 10^{-8}\ M_\odot \mathrm{yr}^{-1}$, the snowline is located so close to the star as 1.3 AU (Sasselov and Lecar, 2000). This would imply that, in our solar system scenario, the snowline would not lie much further away and all the objects that populate the main-belt of asteroids would be icy bodies, being in disagreement with observations (Podolak, 2010). However, the above mentioned model just considers the gas temperature, at $\sim$ 170 K, as the only parameter to obtain the snowline's position.

To obtain a more realistic result, it is necessary to take into account other physical parameters that are important for the condensation/evaporation of icy grains (like a: water vapour density within the disc; b: the distribution of the radiation field; and c: the size distribution and composition of the grains). These parameters are strongly influential for the determination of the thermal balance between the grains and the surrounding gas. It basically depends on five terms (Podolak, 2010).

- Heating processes:
  - Radiative Heating: Induced by direct radiation of the star or the surrounding medium, depending on the optical thickness of the disc.
  - Gas Heating: Produced by grain contact with gas.
  - Condensation Heating: Grain's heating by the water condensation on it.

- Cooling processes:
  - Radiative Cooling: Cooling out by radiation to space.
  - Evaporative Cooling: Produced by the sublimation of water.

As the PPD evolves, the accretion rate reduces and the snowline migrates inwards because viscous dissipation of gas, which is the main heating source in the disc, is also reduced during the disc's evolution (Garaud and Lin, 2007). In the later formation phase, when the accretion rate is much lower, the snowline moves outwards due to stellar radiation (Oka et al., 2011). In figure 4.2 it is shown the relation between the snowline position (distance to the star) and the mass accretion rate.

Due to the turbulent nature of the disc, water vapour diffuses through the snowline into regions where it condenses (Stevenson and Lunine, 1988). At the same time, icy objects drift inwards and sublimate enhancing the water vapour density (Cuzzi and Zahnle, 2004) and, eventually, releasing dusty material contained (Saito and Sirono, 2011; Aumatell and Wurm, 2011a). Although it seems a self-compensating process that does not produce net growth, since small aggregates are coupled to the gas, their random trajectories eventually causes that a significant part of the particles remain in the condensation region, growing to larger sizes by condensation of diffused water vapour. Ignoring collisional processes, this condensation would lead to the formation of decimetre-sized icy bodies in only 1000 years (Ros and Johansen, 2013). However, the timescale for further growth would increase at this point due to bouncing and fragmentation (expected to occur for decimeter-size icy objects). Experimental studies show that this behaviour could be common in scenarios like planetary rings or impacts between Kuiper belt objects (Hatzes et al., 1988; Dilley, 1993; Kato et al., 1995; Higa et al., 1998), but also in planetesimal formation scenarios (Bridges et al., 1996; Heißelmann et al., 2010; Shimaki and Arakawa, 2012). A more detailed analysis of ice collisions is shown in section 6.3.2.

4.2 Amorphous and Crystalline Ice

Water ice presents a severe polymorphism and exists in, at least, 15 different phases depending on the temperature and pressure conditions (Loerting and Giovambattista, 2006). On Earth, the most common ice structure is the so called *hexagonal*

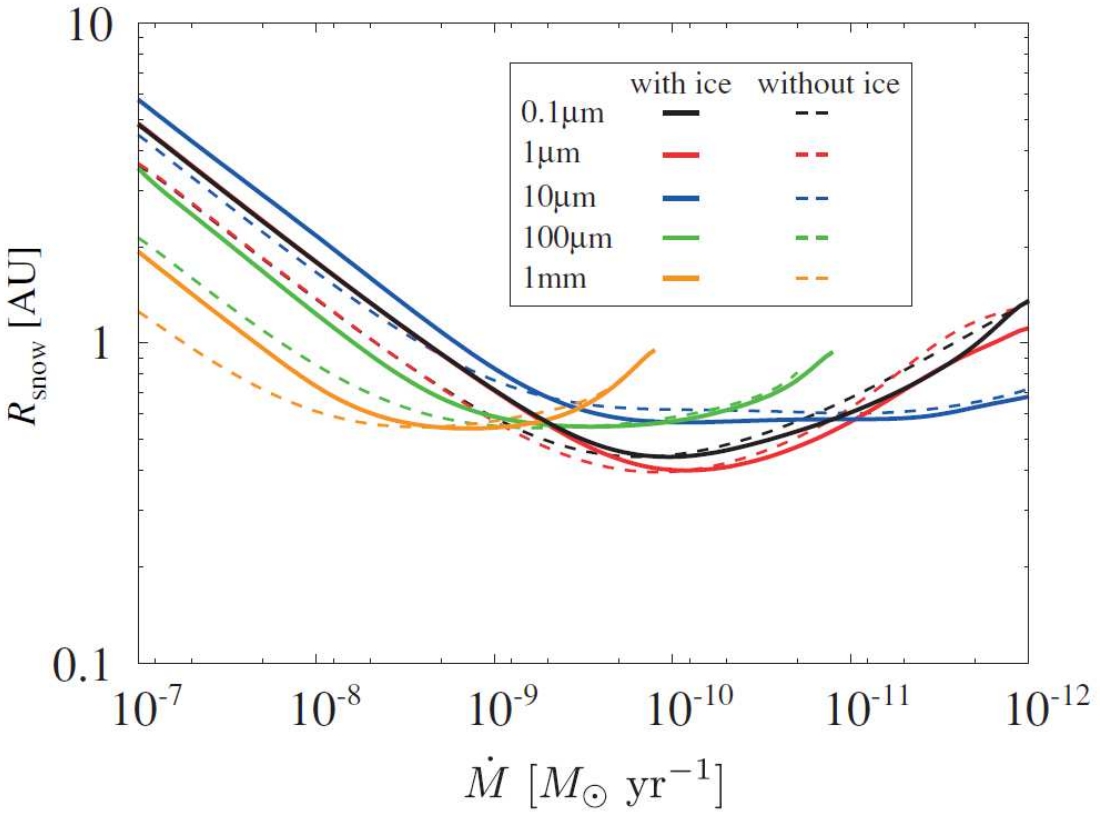

Figure 4.2: Distance of the snow line to the star as a function of the mass accretion rate with various dust grain sizes (Oka et al., 2011). The stellar parameters are $M_\star = 1\,M_\odot$ as the mass; the effective temperature on the stellar surface $T_{\rm eff} = 4000$ K; the stellar luminosity $L_\star = 1\,L_\odot$; and $\alpha = 0.01$ as the viscosity. The horizontal axis represents the mass accretion and the vertical axis, the location of the snowline. The black, red, blue, green, and orange curves represent the results with dust grain sizes of 0.1, 1, 10, and 100m, respectively. The solid and dashed curves represent the results with and without ice opacity, respectively.

ice (Ih) and, at very low pressures, it is stable down to temperatures of 170 K. The term hexagonal is referred to the disposition of the water molecules in the crystalline structure. For lower temperatures, the structure of the water molecules is to the so called *cubic ice* (Ic), where the molecules present a regular cubic distribution. While Ih and Ic have a clear and regular structure, for temperatures below 130 K the molecules lose this property to become an irregular structure known as *amorphous ice* (Hobbs, 1974).

Temperature and pressure ranges in PPD are wide enough to assume that water ice should be present as Ih, Ic and amorphous phases during the first planetesimal formation stages. By investigating ice condensation, we can understand the formation

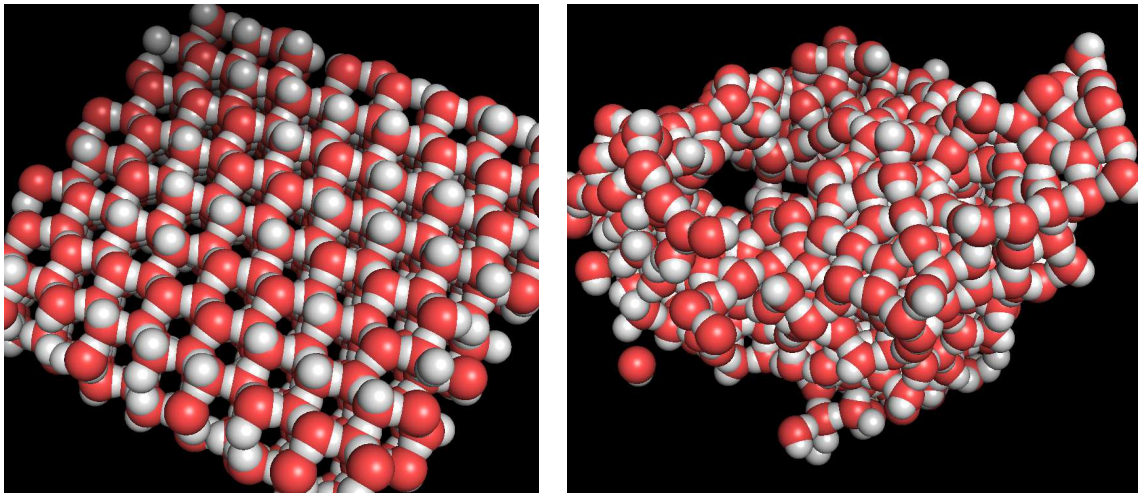

Figure 4.3: Left: molecular structure of hexagonal ice (Ih) with a periodic distribution of water molecules forming a well defined lattice. Although Ih presents mainly a well defined periodicity, it presents defects and dislocations at a molecular scale. Right: molecular structure of amorphous ice. In this case, the water molecules are distributed randomly in the space forming eventual pores. Red and white spheres represent oxygen and hydrogen atoms respectively, and their sizes have been exaggerated to distinguish the molecular structure.

and evolution of icy grains in interstellar and circumstellar discs (as well as icy bodies, like comets and centaurs). Observational evidences of amorphous ice in comets (Meech et al., 2009) and centaurs (Jewitt, 2009) have been already extrapolated. It is important to point out that the crystallization process from pure amorphous ice to non-amorphous phases is exothermic and irreversible. That implies that amorphous ices can only be obtained by direct vapour condensation or quenching. Therefore, it is possible to trace a history of an object depending on the type of ice it contains.

However, it is possible to obtain amorphous ice from crystalline forms. Mishima et al. (1984) obtained amorphous ice subduing Ih at 77 K to pressures above 1 GPa. This type of ice is known as *high density amorphous ice* (HDA), while *low density amorphous ice* (LDA) is referred to those that are stable at much lower pressures. These pressure conditions are hard to be found during the first stages of planetesimal formation and it should not be considered as a process that could play any role here. Though water could be one of the most abundant solids in outer regions of PPDs, it is normally mixed with other volatiles forming structures known as clathrates. This structures have slightly different properties that may allow endothermic phase transitions from amorphous to crystalline icy structures.

The irregular disposition of molecules in amorphous ice structures causes the forma-

tion of big pores (see figure 4.3). As it was mentioned above, porosity plays a very important role on collisional outputs, aggregate density and gas-grain interactions. In icy aggregates, the molecule distribution affects important physical parameters and thermal properties as well (Marboeuf et al., 2012). In particular, amorphous ice is more inelastic than crystalline ice, specially at temperatures < 100 K (Wang et al., 2005). Therefore, the knowledge of where and how icy grains condensate is very important in order to know how they evolve into larger bodies. Since the type of ice can be relevant, or even very important for aggregate's sizes up to centimetres (or more) (Wang et al., 2005), it would not be so significant from a collisional point of view when icy planetesimals are involved. That would depend on how porous the planetesimal are considered to be.

Chapter 5

Surface Contact Forces

In order to predict accurately the outcome of aggregates' collisions, it is fundamental to understand how the contact between their composing monomers are. When the surfaces of two bodies touch, molecular forces take action and produce a mutual attractive interaction. Van der Waals' interaction is the lower limit for such forces, but depending on the material, stronger interactions (like dipole-dipole attraction between ices or metallic binding) may take place (Dominik and Tielens, 1997). If we consider interstellar aggregates as a conglomerate of multiple monomers, it is very important to understand how they interact with each other. Different material and monomer's sizes will condition the characteristics of this attraction. Since in this work the first stages of aggregation are considered, the typical particle sizes which the following description refers to, are $\sim$ µm.

Real ice and dust aggregates are composed by irregular monomers which are different to each other. However, most of the models assume a perfect spherical shape of monomers in order to simplify calculations and increase efficiency (see figure 5.1).

Let us assume that the aggregates are composed by spherical monomers which are indivisible. Further on, let us suppose that two of these monomers, with radius R_1 and R_2, are pressed together under a static force F. A circular contact area with radius a is formed and can be estimated by (Chokshi et al., 1993):

$$a = \left(\frac{3RF}{4E^\star}\right)^{1/3} \tag{5.1}$$

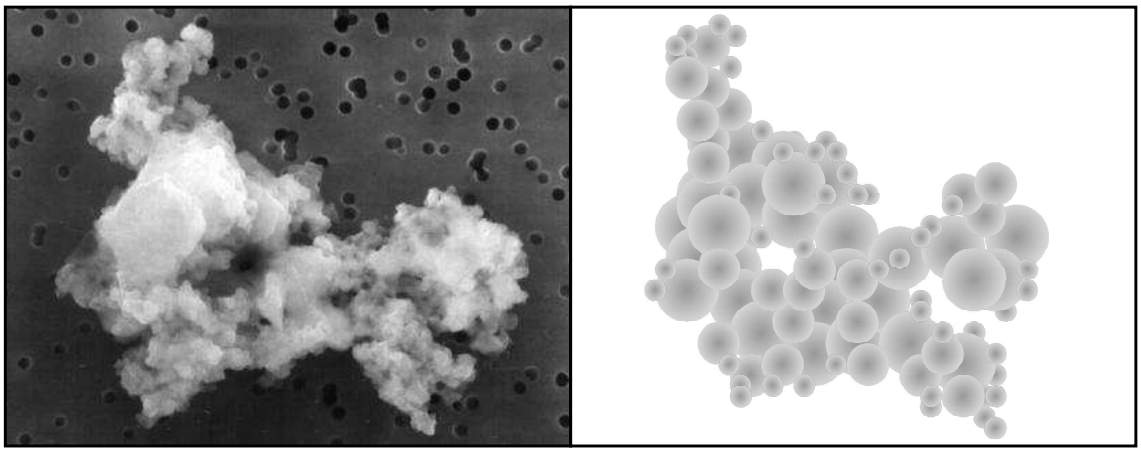

Figure 5.1: Left: Electron Scattering Microscope image of a 10 μ interstellar dust grain collected by a high-flying U2-type aircraft (Credit: NASA). Right: Approximated simulation of the same grain composed by spherical monomers of different sizes.

where $R = (R_1 R_2)/(R_1 + R_2)$ is the reduced radius of the spheres and $1/E^\star = [(1-\nu_1^2)/E_1 + (1-\nu_2^2)/E_2]$ with ν_i and E_i being the Poisson ratio and the Young modulus from the i-th sphere respectively. This situation can be applied to a collision of two spherical monomers.

5.1 Compression and Adhesion Forces

Let us now assume that two particles remain in contact after a collision and it has been long enough for the system to achieve equilibrium. If they are pulled apart with a force F, the attractive forces will apply the same force F but in the opposite direction. Using the model described by Johnson et al. (1971) this force can be described as (Chokshi et al., 1993)

$$F = \frac{4E^\star a^3}{3R} - 2\pi a^2 \sqrt{\frac{4\gamma E^\star}{\pi a}}, \tag{5.2}$$

where γ is the surface energy per unit surface.

It must be noticed that equation 5.2 is the result of solving equation 5.1 plus a term that corresponds to attraction. As the particles are pulled apart, the contact area will shrink. This shrinkage can be estimated by solving the contact area a from equation 5.2:

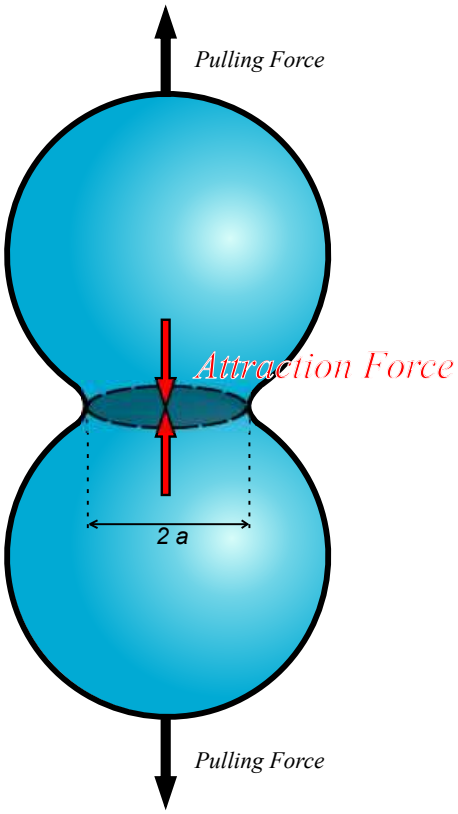

Figure 5.2: Sketch of two contacting spherical grains. The size of the contact area, with a radius a, is defined by the combination of attractive (van der Waals, dipole, etc.) and repulsive forces.

$$a = \left[\frac{3R}{4E^{\star}}\left(F + 6\pi\gamma R + \sqrt{(6\pi\gamma R)^2 + 12\pi\gamma RF}\right)\right]^{1/3} \tag{5.3}$$

It is important to note that in the case of pulling, the force F in equation 5.3 must be considered negative $(-F)$. If no force is applied $(F = 0)$ then we would obtain the radius a_0 of the contact area at equilibrium

$$a_0 = \left(\frac{9\pi\gamma R^2}{E^{\star}}\right)^{1/3} \tag{5.4}$$

If we keep pulling both particles apart, there will be a moment when the contact will break up. Since the pulling force is considered negative, solutions of equation 5.3 are real only if $12\pi\gamma RF \leq (6\pi\gamma R)^2$, that implies $F \geq -3\pi\gamma R$. Then the critical force F_c necessary to break up the contact is

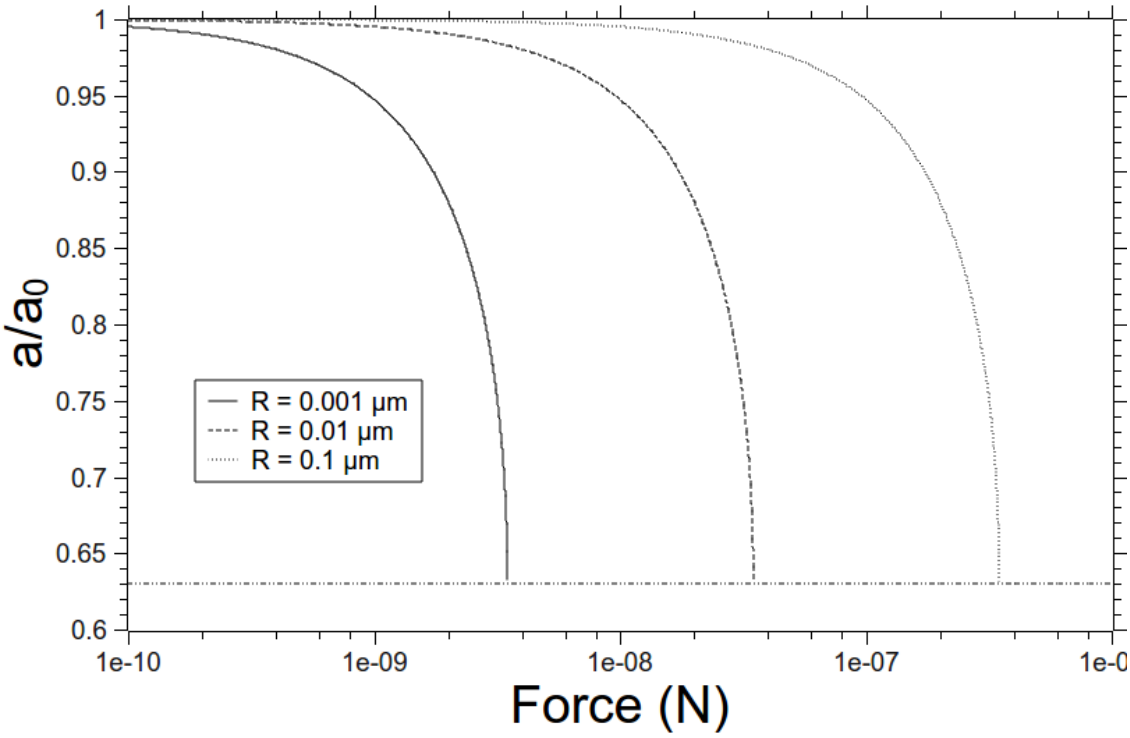

Figure 5.3: Relation of the ratio a/a_0 with the applied external pulling force. The variation of the ratio is plotted by 3 different reduced radius R, 0.001 µm (solid curve), 0.01 µm (dashed curve), 0.1 µm (dotted curve). The breakup takes place when the force is $F = -F_c$ and occurs always at a contact area ratio of $a/a_0 = 0.63$ (horizontal dotted line), independently on the reduced radius value R.

$$F_c = 3\pi\gamma R \tag{5.5}$$

Substituting $F = -F_c = -3\pi\gamma R$ in equation 5.3, gives the value of a at which the contact will break up, i.e. the smallest radius the contact can achieve before it breaks. This is $(1/4)^{1/3}a_0 \approx 0.63a_0$. Then, independently on the size of the grains, their contact will break up when the pulling force becomes high enough to make the contact area a lower than 0.63 times its value at the equilibrium state (see figure 5.3).

If the aggregates are considered to be composed by spherical monomers, the structure of the whole solid will strongly depend on how strong the contacts between them are. Pull-off forces are limited to the direction defined by the line passing through the center of masses from both particles. However, perpendicular forces to this direction may cause stress and torques able to change the contact area form

and position.

5.2 Rolling Force

The arguments exposed in this section (5.2) and the following one (5.3) are based on the model developed by Dominik and Tielens (1995, 1996, 1997) and references therein.

As in the previous section, let us consider again two spherical particles that are attached by a contact area a_0 in equilibrium. For (sub)micron particles, friction's sources such as microslip at the interface, inelastic or viscoelastic deformation of the involved materials and large surface irregularities are not considered to be important (Dominik and Tielens, 1997). If an external force perpendicular to the axis that connects the centres of each particle is applied to one (or both) sphere(-s), a resistance force at the contact area will appear acting in the opposite direction (see figure 5.4). This force causes a displacement ξ from the affected particle's center of mass perpendicular to the vertical axis. Therefore, a redistribution of forces in the contact area is induced and a net torque M_{r} appears.

As long as this displacement is not greater than a critical value ξ_c, the structure will return to its initial state once the external force vanishes. But, if the force causes a displacement $\xi > \xi_c$, the contact between atoms at the trailing edge of contact region in the rolling direction will be broken. At the same time, new contacts between atoms are formed on the leading edge of the contact area. This process keeps on until the external force lies under the above mentioned critical value.

The torque produced by the rolling force when it is displaced by a critical distance ξ_c is (Dominik and Tielens, 1995):

$$M_{\mathrm{r}} = 4F_{\mathrm{c}} \left(\frac{a}{a_0} \right)^{3/2} \xi_c \tag{5.6}$$

Though it does not appear in equation 5.6, the resistance to rolling, and therefore, the rolling torque's magnitude, depends mainly on the material surface energy. However, ξ_c is assumed to belong to the order of some atomic diameters, independently on the considered material.

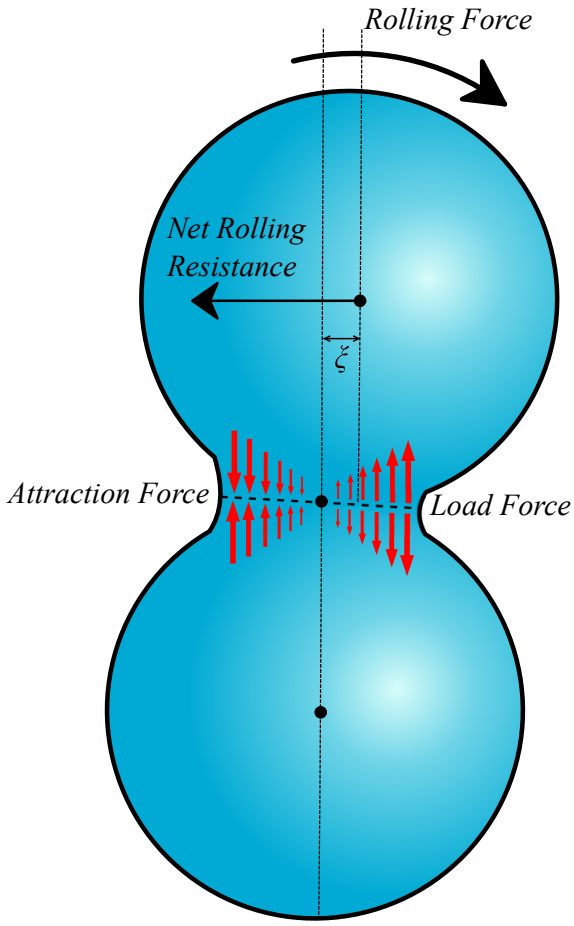

Figure 5.4: Sketch of a rolling force applied to two spherical grains. The external force is applied perpendicularly to the direction of the line that joins the center of both grains. This causes a displacement ξ of the center of mass of the upper grain. The net restoring force produced by the contact is also perpendicular to this line but opposite to the external force direction.

5.3 Sliding and Twisting Forces

As in the rolling case, sliding of particles causes the breaking up of contacts between atoms at the contact area. But through sliding processes, new contacts are formed (or old ones are broken) when atoms from the interface move over each other instead of approaching (or separating), as in the rolling movement.

For (sub)micron grains, the two main friction sources are (Dominik and Tielens, 1996):

- The surface roughness on atomic scales (steps on the surface grid of the particle material).

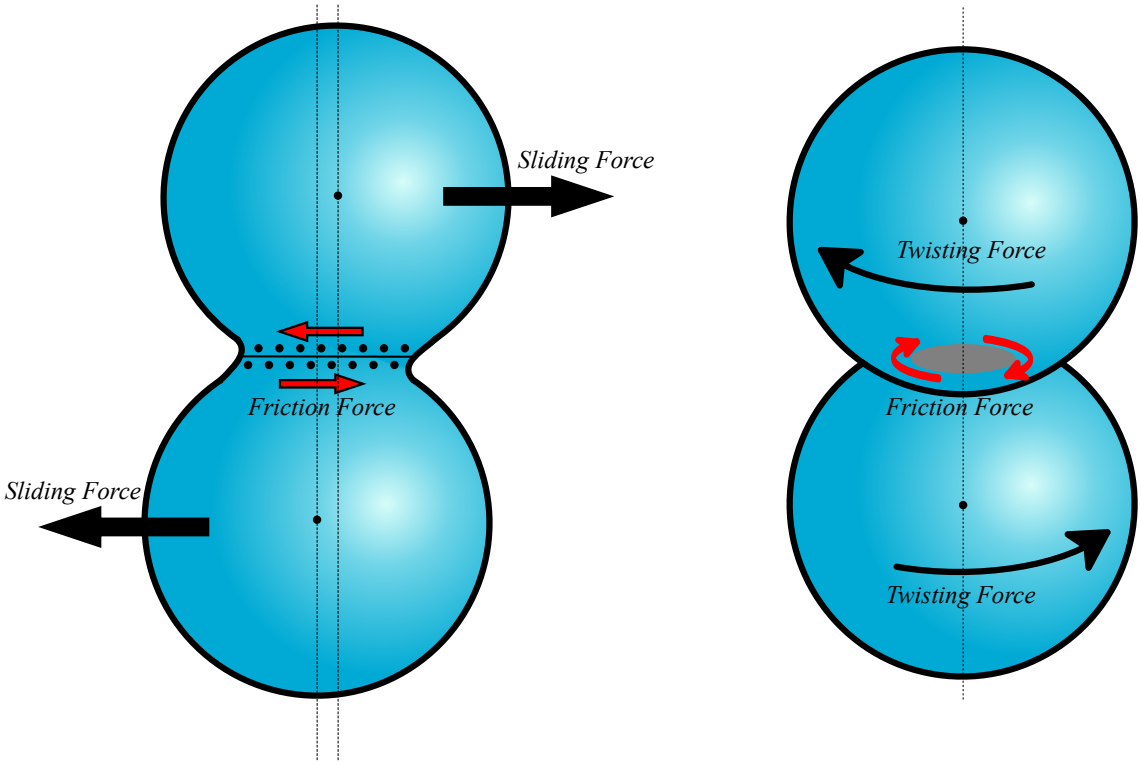

Figure 5.5: Left: Sketch of a sliding process between two spherical grains. The restoring friction force at the contact area is opposite to the direction of the external forces. Right: For the twisting case, the restoring friction force is also opposite to the twisting external force.

- The energy loss by instabilities caused by the sliding motion for individual atoms.

The first contribution may be expressed as:

$$F_{\mathrm{fr}}^{\mathrm{steps}} = \frac{G}{2\pi}\pi a^2 \tag{5.7}$$

where $G^{-1} = G_1^{-1} + G_2^{-1}$ is the reduced shear modulus (the rest of parameters are already given above).

The second source of sliding friction is caused by the following assumption: an atom sliding over a step-free region, is affected by the interaction with the other atoms belonging to the same grain which it forms part (A-A) and, at the same time, with the surface's atoms of the other grain upon which it is displacing (A-B). If the interaction with the other atoms (A-B) is negligible compared to the forces

with the atoms in the grain to which it belongs (A-A), then the sliding movement won't produce any energy dissipation -unless the particles are heavily pressed to each other-. If A-B interactions are of the same order of A-A interactions, the displacement will be conditioned by the surface's atoms of the other grain. This effect is associated to a force induced by the caption of the considered atom in a potential well, produced by the atoms on the surface. If the pressure on the contact area, tangential to the surface, exceeds a critical value p_c, then the associated critical force may be estimated as:

$$F_{\text{fr}}^{\text{slide}} = \frac{1}{3}F - \frac{\pi a^2}{3}p_c, \tag{5.8}$$

being F the force in the vertical direction. The critical pressure depends on the considered material and it may be calculated as:

$$p_c = \frac{2.67}{\pi}\frac{b^3}{\sigma^3}G - \frac{24.72}{\pi}\frac{b^4}{\sigma^5}\gamma. \tag{5.9}$$

Here, b is the main distance between atoms in the grain's material and $\sigma\sqrt[6]{2}$ is the equilibrium distance in the pair potential model for A-B interaction.

Since interaction between atoms and molecules of metallic materials are driven by metallic bonds, and water ice molecules interact via dipole and hydrogen bonds, this second mechanism is strong enough not to be negligible. In contrast, surface interactions between atoms and molecules of materials like silicates and graphite, take place via van der Waals forces, which are much weaker than the bonds between their own bulk bodies (Si-O and C-C bonds). That implies for this kind of materials, that the second mechanism may be discarded. According to this idea, the sliding friction force may be written as:

$$F_{\text{fr}} = \frac{G}{2\pi}\pi a^2 + \begin{cases} 0, & \text{silicate, graphite, etc.} \\ \dfrac{1}{3}F - \dfrac{\pi a^2}{3}p_c, & \text{metal,ice.} \end{cases} \tag{5.10}$$

In this section, the sliding process is considered to occur along the surface as a straight displacement. However, sliding can also happen if the grains rotate around their common vertical axis at different angular velocities (see figure 5.5), causing a twisting motion. The treatment of this case is similar to that of sliding, the

only change is the direction in which the atoms move. Analogously to the pulling-off, rolling and sliding cases, in twisting motion exists a critical angle beyond which contacts are broken up and new ones are formed. The torque associated to a twisting motion caused by the steps on the surface grains may be computed as:

$$M_{\mathrm{tw}}^{\mathrm{steps}} = \frac{Ga^3}{3\pi} \tag{5.11}$$

and the contribution associated to the single atomic break-up and formation contact is:

$$M_{\mathrm{tw}}^{\mathrm{slide}} = \frac{\pi}{3} F_{\mathrm{c}} a_0 \left[\frac{3}{4} \left(\frac{a}{a_0} \right)^4 - \left(\frac{a}{a_0} \right)^{(5/2)} \right] - \frac{2}{9} \pi a^3 p_c. \tag{5.12}$$

As mentioned, the contribution of $M_{\mathrm{tw}}^{\mathrm{slide}}$ is negligible for silicates and graphite particles. As a result, the total critical torque of twisting motion may be written as:

$$M_z^{\mathrm{c}} = \frac{Ga^3}{3\pi} + \begin{cases} 0, & \text{silicate, graphite, etc.} \\ M_{\mathrm{tw}}^{\mathrm{slide}}, & \text{metal,ice.} \end{cases} \tag{5.13}$$

Chapter 6

Experiments on Water Ice Sublimation: Implications for The Snowline

As pointed out in section 4.1, condensation of water in specific regions of PPDs is a fundamental process for the formation and evolution of the first planetesimals. The enhancement of solids close to and beyond the radial and atmospheric snowline seems to be a key factor to the ulterior planetary growth. The same way as water condensation (among other less abundant volatiles) is very important, ice sublimation plays a fundamental role.

According to my personal research, the study of ice sublimation's importance in PPDs regarding to planet formation has been almost exclusively investigated from a theoretical point of view (e.g. Hayashi, 1981; Ciesla and Cuzzi, 2006; Eisner, 2007; Grigorieva et al., 2007; Machida and Abe, 2010; Sirono, 2011a; Saito and Sirono, 2011; Ros and Johansen, 2013). In this chapter I will introduce the experimental methods I carried out in order to compare some of the existing models with the results I obtained in the laboratory.

It has already been mentioned that solid bodies (large enough) decouple from the gas and drift inwards towards the central star. This process is applicable to icy aggregates as well. Large aggregates drift inwards from the colder regions of the disc where the dominant mass fraction of solids is ice. Saito and Sirono (2011) suggest a model where dusty cores mantled by ice sublimate when they cross the

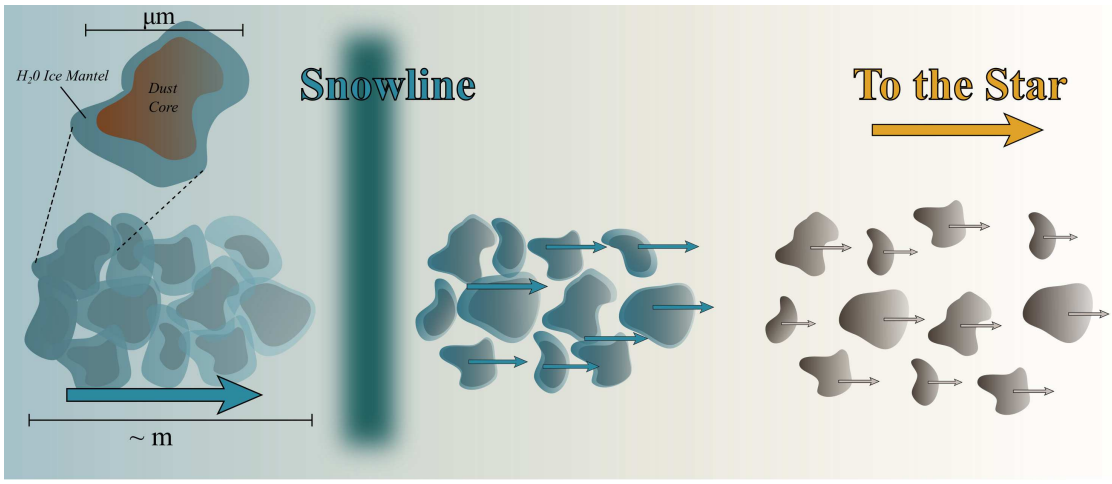

Figure 6.1: A meter sized icy aggregate, formed by multiple dusty grains embedded in ice, drifts toward the star in a protoplanetary disc. When the aggregate crosses the snowline starts to sublimate. Sublimation causes the fragmentation of the icy aggregate into smaller bodies. After the complete ice sublimation, the dusty cores are released close to the snowline. This enhances the concentration of dust for the planetesimal formation. The final structure of the released dusty aggregates depends on how the larger body sublimates.

snowline in their infall and during this phase fall apart in several pieces. Only the dusty cores embedded within the aggregates survive and, due to the fragmentation process, a larger number of small particles or aggregates gather at or close to the snowline. Since the fragments are smaller compared to their progenitor, the drift velocity is much smaller and the particles concentrate around the snowline. As a consequence, this might boost the formation of planetesimals. In fact, large reservoir of small particles increase the hit-stick growth efficiency (Blum and Wurm, 2008) for large bodies and are fundamental ingredient for models based on sweep-up processes (Windmark et al., 2012).

The study of water ice sublimation is not only applicable to planetesimal formation context. The seasonal cycles on Mars cause the condensation and later sublimation of water on its surface with special relevance on the poles (Montmessin et al., 2007). The presence of ice boulders in cometary tails that become detached from the comet's nucleus, is also mainly caused by water ice sublimation (Hadamcik et al., 2013).

6.1 Experimental Procedure

In order to study the effects of ice sublimation on the planetesimal formation at the snowline, the following setup was developed. The aim of the setup developed for this experiment, described in section 6.1.1, is to levitate water ice aggregates in order to observe their mutual interaction while suffering the effects of sublimation.

6.1.1 Experimental Setup

The setup sketched in figure 6.2 consists mainly of a Peltier element of 5×5 cm^2 situated inside a vacuum chamber. In order to levitate the ice aggregates 2 main conditions are needed: **1**- low pressure ($\sim$ 1 mbar) and **2**- a temperature gradient between the lower and upper regions where the aggregates are placed. The mechanism of particle levitation is exposed in section 6.1.3. The chamber was hermetically closed and connected to a vacuum pump. The Peltier element was connected through the chamber walls to a DC power supply. To dissipate the heat produced on the warm side of the Peltier, it was located on a hollow copper platform which was cooled by a water circuit system.

To produce the temperature gradient, the aggregates were situated on an aluminium plate, which at the same time lies on the Peltier element. Its upper surface was slightly concave in order to keep the aggregates inside a limited area. The temperature on the plate was low enough to keep the ice aggregates at temperatures well below their melting point. The top of the chamber was covered by a special lid with a container attached to its lower face. With the lid lying on the top of the chamber, the bottom of the container remained situated to a distance of 5 cm from the aluminium plate. Filling the container with liquid nitrogen, the temperature at the bottom of the container could be cooled down to 77 K (once equilibrium was achieved). The maximum temperature gradient between the plate and the container applicable to the experiment was 196 K. Ice aggregates would melt if temperatures on the plate were higher.

To observe the phenomena taking place in the chamber, a high speed camera attached to an objective was employed. The upper lid was drilled along the vertical axis to allow the observation from above. The hole on the top of the lid was covered by a glass tap in order close the chamber hermetically. At the same time, two sides

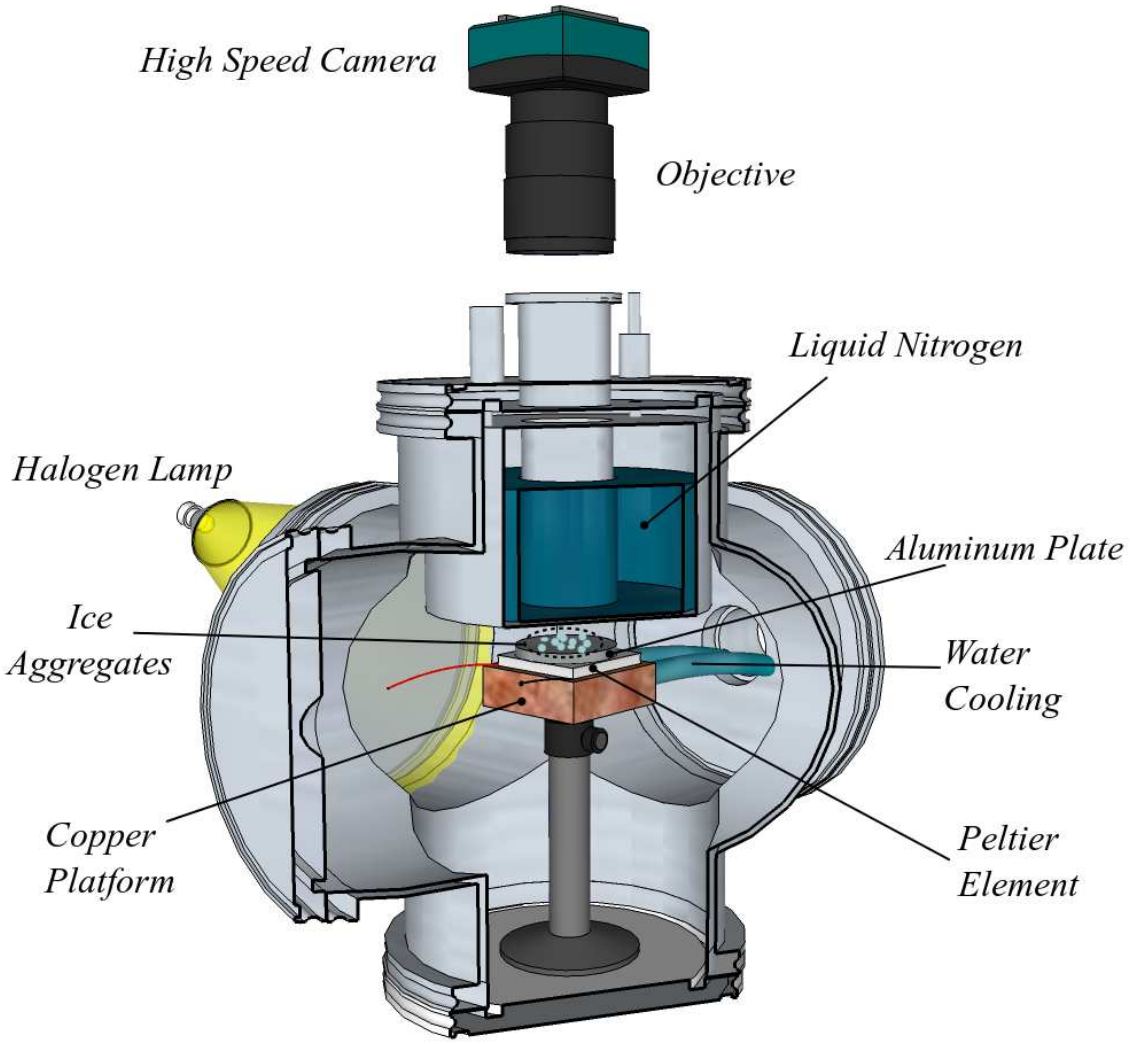

Figure 6.2: Sketch of the experimental setup. In a vacuum chamber, ice aggregates are placed on an Aluminum plate. The plate is located on a Peltier element at 260 K, cooled by a copper-water cooling system. On the top of the chamber, a lid with a liquid nitrogen container is placed in order to produce a temperature gradient. The setup is illuminated by an external halogen lamp through one of the chamber walls made of glass.

of the chamber were covered by glass to permit the illumination and observation of the interior.

6.1.2 Aggregate Generation and Manipulation

The ice aggregates were created by condensation. Water vapour from the air condensate on the surface of a tube cooled by liquid nitrogen. After a few minutes a thin layer of condensed ice formed and its structure, similar to fluffy aggregates, can

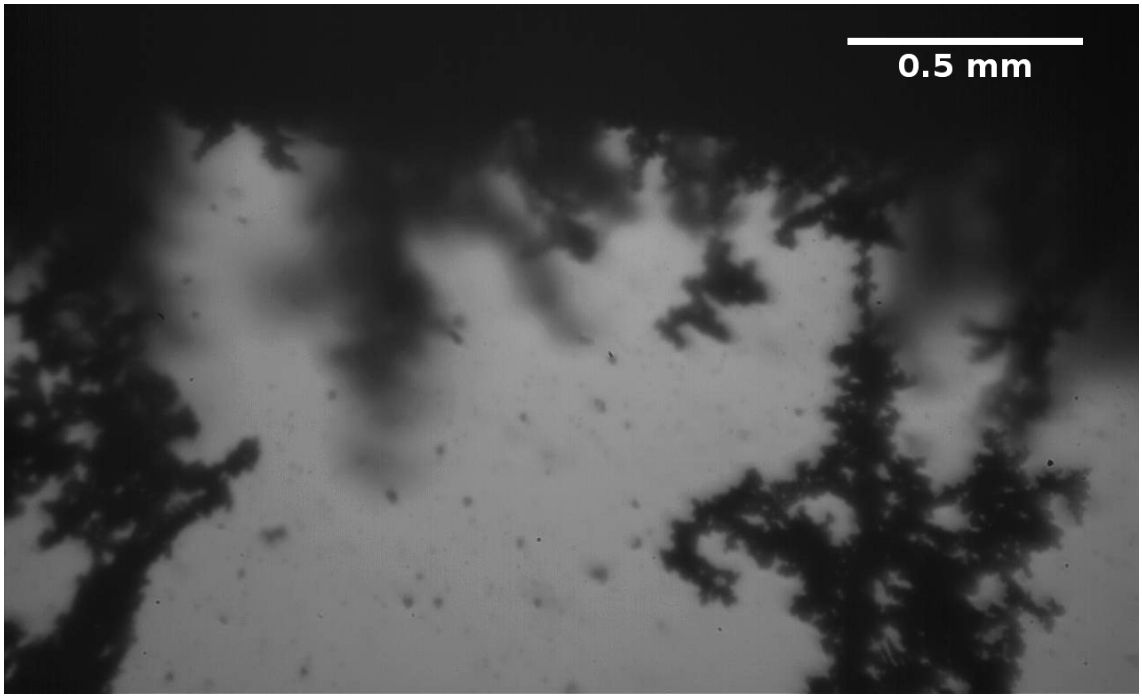

Figure 6.3: Long microscope image of ice aggregates used for the experiment. The picture shows a section of the lower part of a tube cooled by liquid nitrogen. The air's water vapour condenses into ice and forms a thin layer icy aggregates around the tube. In the image some chains can be observed, this is due to the effect of the gravity that pulls the condensed grains downwards, forcing the aggregates to adopt the observed shape.

be observed with a long range microscope. Since the aggregate formation process is always the same, it is assumed that their properties are almost identical. An example of the aggregate's formation process may be observed in figure 6.3.

It is difficult to establish which is the exact morphology or structure of the individual ice grains of which aggregates are made. In this experiment, the condensation of water vapour from the air takes place at temperatures much lower than 273 K. This is comparable to the process that occurs during the formation of dry snow in the atmosphere. For that reason, it is reasonable to assume that the ice density formed in the laboratory is very similar to the non-pressed snow density formed in the atmosphere $\rho_S = 50 - 100$ Kg m^{-3} (Petrenko and Whitworth, 1999). That implies a porosity $\eta = 1 - (\rho_S/\rho_{bulk}) \approx 0.9 - 0.95$, where ρ_{bulk} is the bulk density of water ice (≈ 0.92 Kg m^{-3}), or a volume filling factor $\phi = 1 - \eta = 0.05 - 0.1$. The ice layer formed around the pipe has a typical thickness of ≈ 5 mm and I assume that possible variations of physical properties through the layer's thickness are not significantly affected. Icy structures formed this way are a reasonably appropriate

model for larger aggregates in PPD, which are also presumably to be formed by aggregation (Blum and Wurm, 2008).

Once I have enough amount of fluffy ice on the pipe, some of it is collected by a previously cooled small spoon and deposited on the aluminium plate through the hole situated on the upper part of the top lid. Since the plate is at $\approx$ 260 K, no significant physical changes on the ice are expected.

6.1.3 Aggregate Levitation

Before the arrangement of the ice aggregates into the chamber, the lid's container is filled with liquid nitrogen to establish the temperature on the top of the working region at 77 K. Once the aggregates are placed on the aluminium plate at 260 K, the evacuation of the chamber starts. When the chamber is at $\sim$ 1 mbar of pressure, the evacuation is interrupted. Under such conditions, the aggregates start to levitate over the plate. The levitation is possible if the aggregates are light and small enough to overcome the gravity force. It is difficult to establish for which exact magnitude or weight the icy bodies start to float, but typical levitating aggregate sizes observed are about 5 mm. It must be pointed out that independently from the size of the floating ices, all of them waft at the same height of $\sim$ 0.2 mm from the plate. A top view photo of some ice aggregates floating on the aluminium plate can be observed on the left side of figure 6.4. In the same figure, on the right side, an approximately 1 mm large aggregate levitates directly on the Peltier element.

The mechanism by which the aggregates levitate is a combination of different processes, mainly caused by a low pressure and a temperature gradient. The different phenomena that may contribute to this effect are presented below.

Knudsen Compressor Effect

The mechanism known as *Knudsen Compressor* was first described in detail by Knudsen (1909). Let us assume two chambers containing the same gas at different temperatures $T_1 < T_2$, communicated by a tube of diameter d_t. The Knudsen number Kn can be defined as the ratio between the mean free path of the gas molecules and a specific length scale, $\lambda_\mathrm{g}/l_\mathrm{s}$. Let us now consider that l_s is the diameter of the tube that connects both chambers d_t. If the mean free path of the

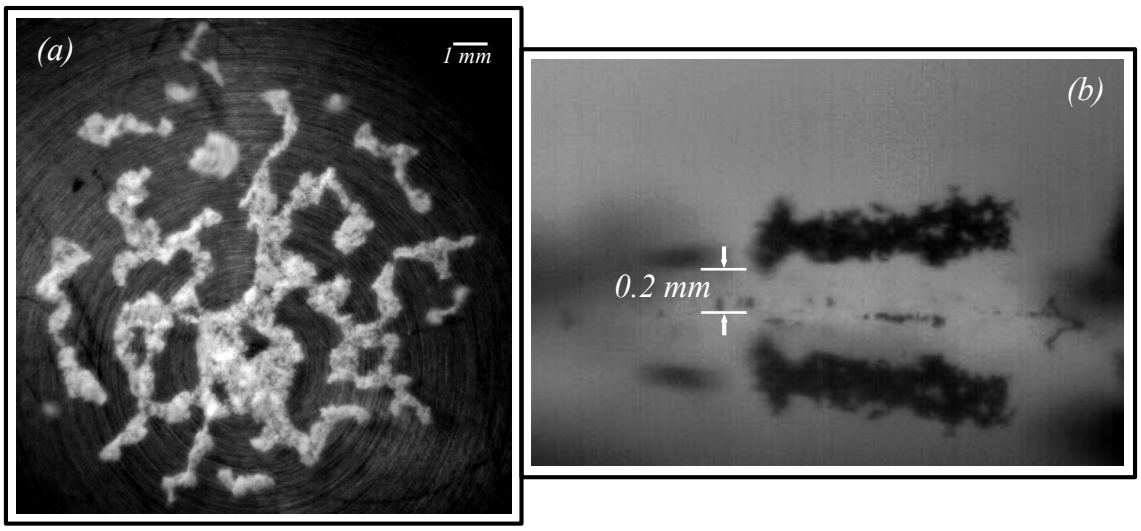

Figure 6.4: (a) Upper view of an ensemble of ice aggregates on the aluminum plate. The whole icy structure can be treated as a 2D body since its extension is much larger than its thickness. (b) Side view of one of the aggregates that is part of the whole ensemble.

gas molecules $\lambda_g \ll d_t$, then the pressure in both chambers is the same ($P_1 = P_2$). On the contrary, if $\lambda_g \gg d_t$ then a thermal creep takes place and an overpressure on the warmer side is produced (see figure 6.5). In thermal equilibrium, this process follows the relation

$$\frac{P_2}{P_1} = \sqrt{\frac{T_2}{T_1}} \tag{6.1}$$

but if the system is not in equilibrium state and $\lambda_g \sim d_t$, then the overpressure created between both sides is (Muntz et al., 2002)

$$\Delta P = P_{\text{avg}} \frac{Q_T}{Q_P} \frac{\Delta T}{T_{\text{avg}}} \tag{6.2}$$

where T_{avg} and P_{avg} are the the average temperature and pressure respectively; Q_T/Q_P is the ratio between the transpiration (creep) and back flow of the gas and $\Delta T = T_2 - T_1$ is the temperature difference between the chambers.

We can consider the structure of a millimetre aggregate like a solid icy body with multiple pores that act like channels as it is represented in figure 6.1.3 (Kelling and Wurm, 2009). The amount and size of the channels depend on the porosity of the material. Since the aluminium plate is much larger than the aggregates and the

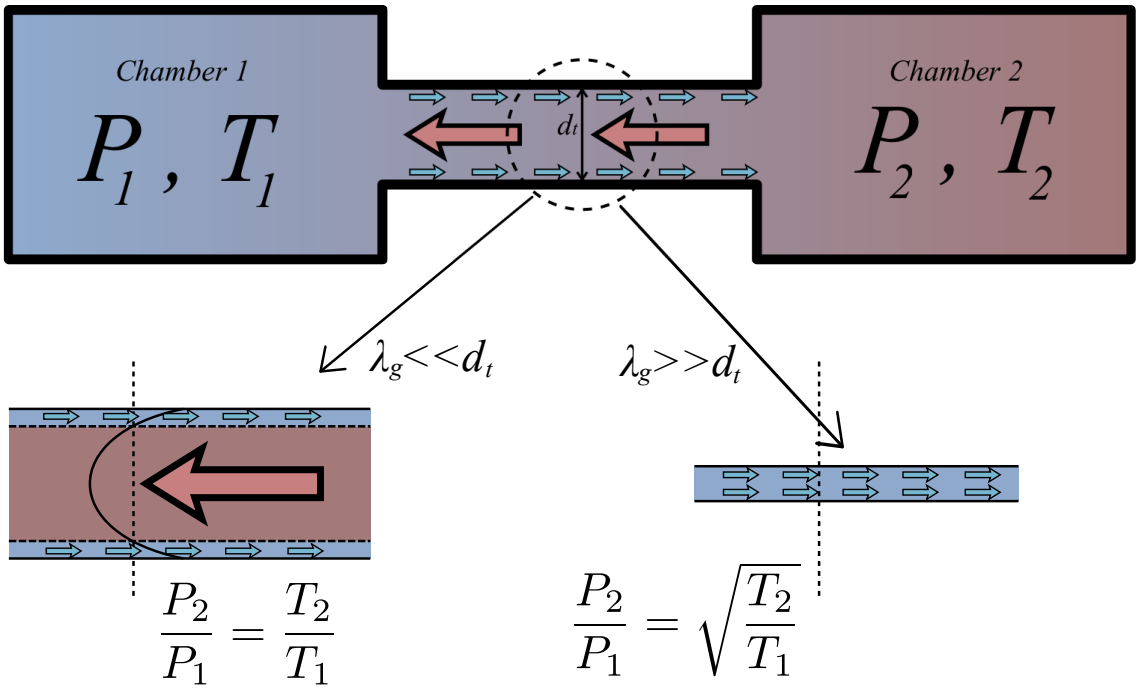

Figure 6.5: *(Up)* Sketch of two chambers at different pressures and temperatures P_i and T_i, separated by a tube of diameter d_t. *(Lower-left)* If the mean free path of the gas molecules λ_g is much smaller than the tube's diameter, the gas flows through the tube from cooler to warmer regions until the equilibrium is achieved. *(Lower-right)* If the mean free path of the gas molecules is much larger than the tube's diameter, thermal creep takes place causing an overpressure on the warmer side.

levitation height, if we consider that the reflectivity of ice is negligible at wavelengths corresponding to a blackbody emission at 260 K ($\sim 11.14\mu$m) (Warren, 1982), then the temperature at the bottom of the floating icy aggregates is the same that the temperature of the plate (260 K). It is possible to calculate the temperature at the top of the aggregate by taking the radiation through it as an effective conduction process (Bauer, 1993) and it is $\kappa_R = 4\sigma\epsilon n^2 T^3 d_p$, where n is the refractive index of the gas; ϵ is the emissivity and d_p the pore size. If ϵ=1, n=1, T=260 K and d_p=50 μm, then $\kappa_R = 2 \times 10^{-4}$ W m^{-1} K^{-1}. The thermal conductivity κ_S of snow depends basically on density (grain size and filling factor) and slightly on temperature (Satyawali and Singh, 2008). Its value varies from $0.02 - 0.07$ W m^{-1} K^{-1} for a density $\rho_S = 100$ Kg m^{-3} to $0.35 - 0.7$ W m^{-1} K^{-1} for a density $\rho_S = 400$ Kg m^{-3} (Petrenko and Whitworth, 1999). Even at its lowest value, it is 2 orders of magnitude higher than κ_R, implying that temperature on the top of the aggregate is mainly determined by conduction through κ_S.

Considering that the top part of the aggregate cools down by radiation until the

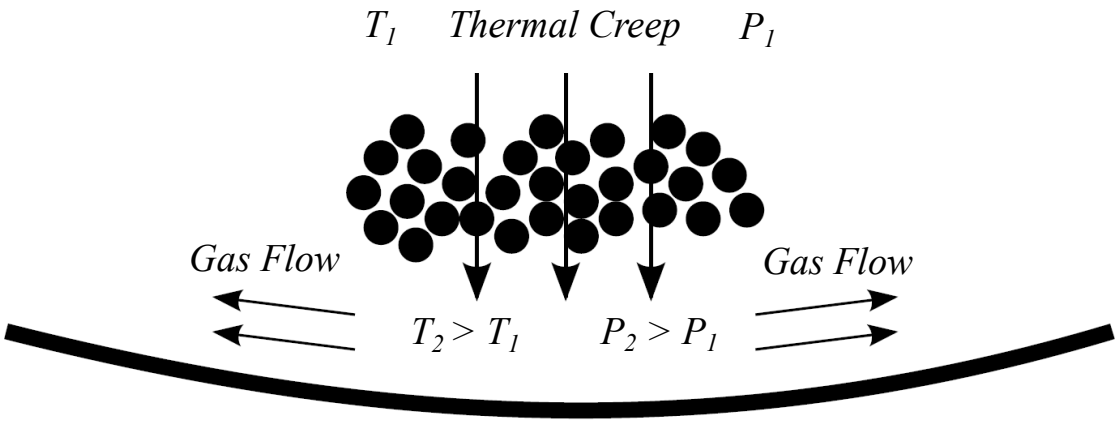

Figure 6.6: Sketch of an aggregate levitation produced by Knudsen compressor effect according to Kelling and Wurm (2009). The aggregate placed on a slightly concave plate in a vacuum chamber which is evacuated to pressures of 1 mbar. The Peltier element is set to $T_2 = 260$ K. Thermal radiation cools the surface of the aggregate to T_1. The aggregate levitates by a pressure difference established through thermal creep (Knudsen compressor effect).

radiative loss is compensated by conduction through the aggregate, the temperature T_1 on the top can be estimated as $\sigma T_1^4 = \kappa_S(T_2 - T_1)/d_a$, where d_a is the aggregate's thickness. For $T_2 = 260$ K, $\kappa_S = 0.02$ W m^{-1} K^{-1} and $d_a = 200$ µm, then $T_1 = 257.7$ K. In order to levitate the icy aggregate, the force produced by the Knudsen compressor effect must overcome the gravity force $F_g = A\rho_I d_a g\phi$, where A is the aggregate's bottom surface; $\rho_I = 920$ Kg m^{-3} the bulk density of ice and $g = 9.8$ m s^{-2} the acceleration of gravity. Taking $d_a = 200$ µm, the minimum pressure difference between the upper and lower surface of the aggregate must be

$$\Delta P_{min} = 1.8\phi \text{ Pa}. \tag{6.3}$$

Since the snow's ϕ is difficult to establish, it will be considered as a free parameter for the moment.

To know whether the aggregate is going to levitate or not by the Knudsen effect, ΔP from equation 6.2 must be solved. The ratio Q_T/Q_P depends on the value of the Knudsen number Kn and the structure of the channels. Assuming that the channels are cylindrical tubes, then Q_T/Q_P can be tabulated as in table 1 from Muntz et al. (2002) and it is plotted in figure 6.7.

The mean free path of a gas is $\lambda_g = 1/(\rho_g \sigma_g)$, being ρ_g and σ_g the density and the

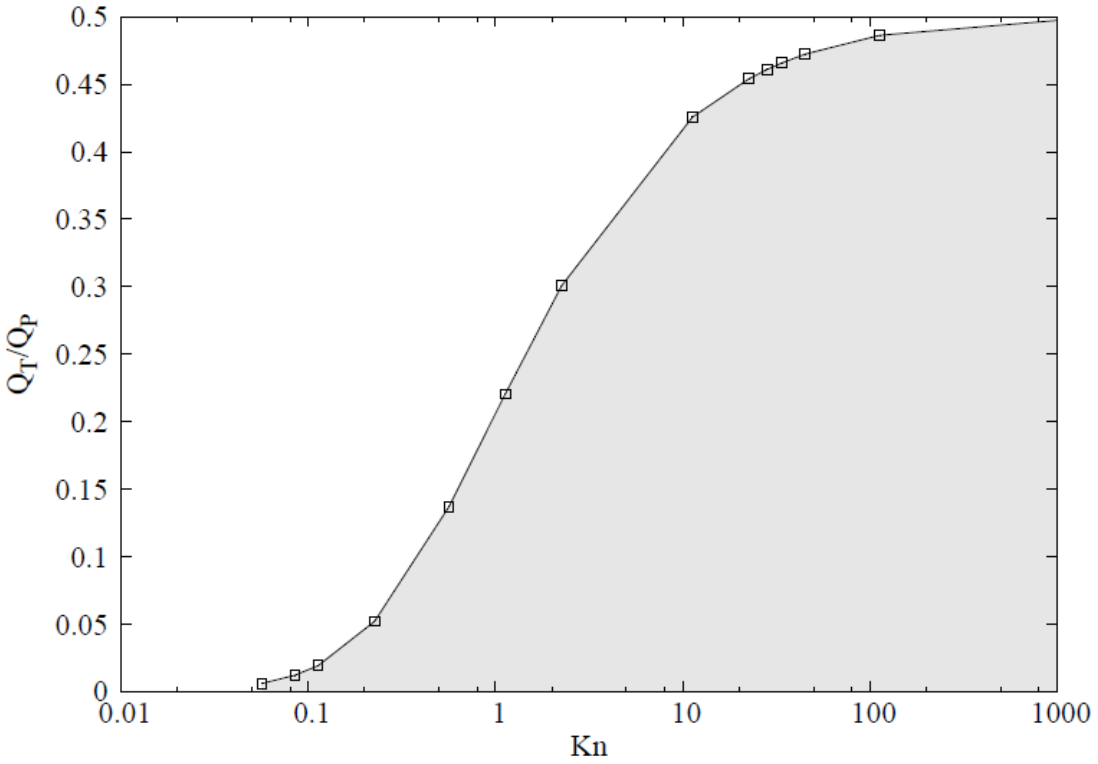

Figure 6.7: Variation of the Q_T/Q_T ratio as function of the Knudsen number Kn according to Kelling and Wurm (2009).

cross section of the gas respectively. The density of air can be written as $\rho_{air} = P_{air}/(k_B T_{air})$, where $k_B = 1.38 \times 10^{-23}$ J K^{-1} is the Boltzmann constant. The cross section of air molecules is $\sigma \approx 1.21 \times 10^{-18}$ m^2 if nitrogen molecules are considered the dominant component. Then, the mean free path of air is $\lambda_{air} = 1.14 \times 10^{-5}\, T_{air}/P_{air}$ meters. Under the conditions used in the experiments ($P = 100$ Pa, $T = 260$ K) this is $\lambda_{air} \sim 3$ µm.

Assuming that the mean pore diameter is ~ 10µm, then $Kn = 0.3$ and $Q_T/Q_P = 0.1$. From equation 6.2, it corresponds to a $\Delta P = 0.09$ Pa, what implies that an ice aggregate levitates if the filling factor is $\phi \leq 0.05$ (see equation 6.3). Since the ice agglomerates used for the experiments are similar to those of fresh dry snow, with a filling factor of $\phi = 0.04 - 0.07$, it is reasonable to assume that Knudsen effect may contribute to the levitation of the icy aggregates.

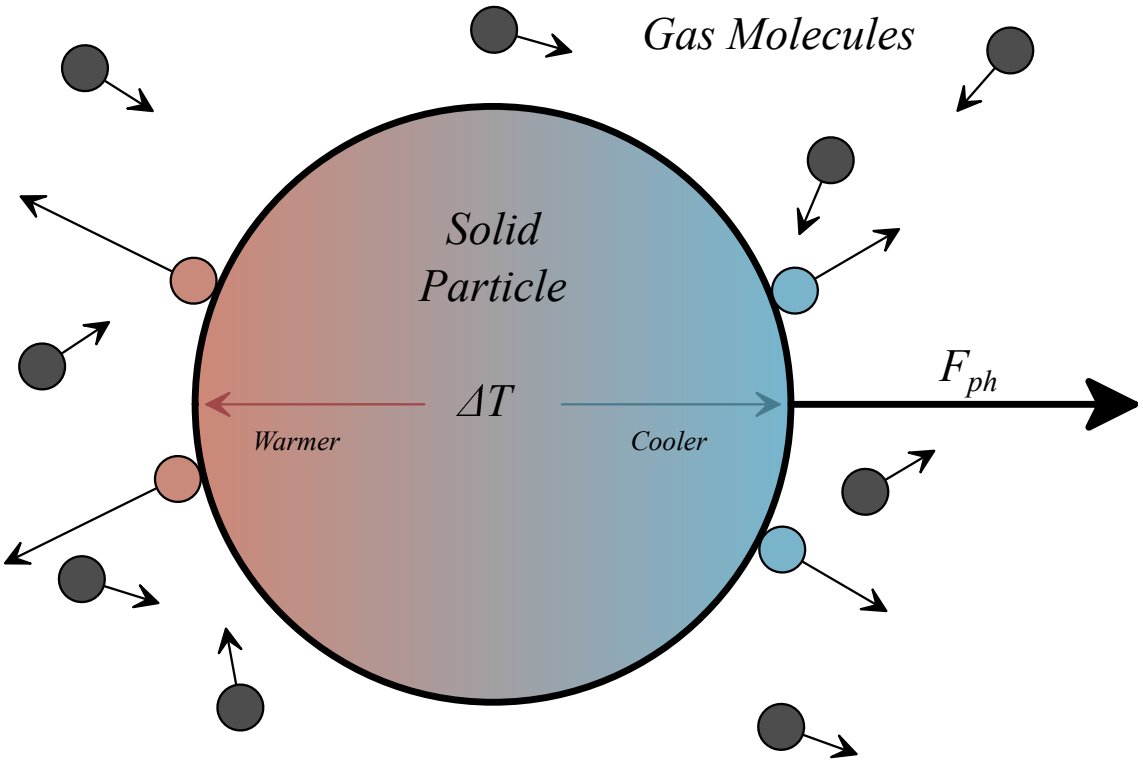

Figure 6.8: Principle mechanism of photophoresis. A temperature gradient within a particle is induced by irradiation. The gas molecules that interact with the warmer side of the particle leave the surface with more velocity than the ones on the colder side. That produces a net momentum transfer to the particle.

Photophoresis

To make it simple, let us assume a spheric solid particle embedded in a rarefied cool gas. Initially, the temperature of the gas and the particle is the same and they are found in equilibrium. Supposing that the particle is radiated on one side. The particle's temperature on the irradiated side becomes higher than the non-radiated by absorption. When gas molecules come into contact with the particle surface, they leave it with higher velocity on the warmer side than on the cooler one. By the momentum conservation, a net acceleration to the non-radiated side of the particle appears.

For a spherical particle of radius a_p, the photophoretic force can be estimated as follows (Rohatschek, 1995):

$$F_\mathrm{ph} = 2F_\mathrm{max}\left(\frac{p_\mathrm{max}}{p} + \frac{p}{p_\mathrm{max}}\right)^{-1} \tag{6.4}$$

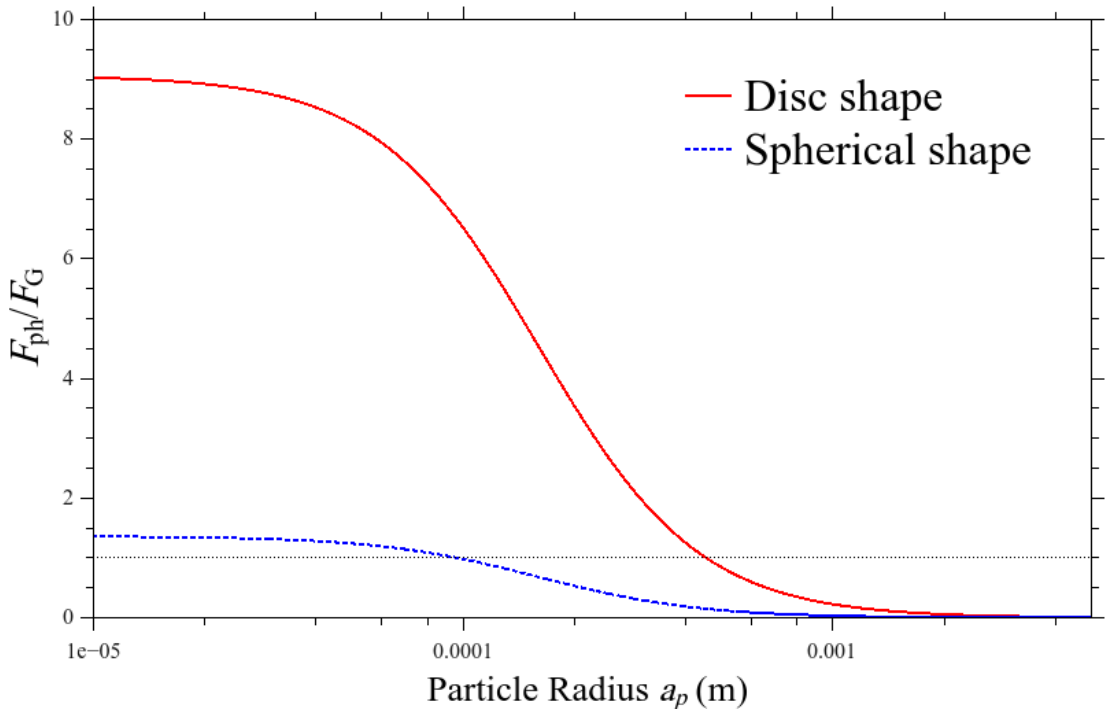

Figure 6.9: Variation of the ratio between photophoretic and gravitational forces $F_{\mathrm{ph}}/F_{\mathrm{G}}$ over the aggregate radius a_{p}. The plot shows the behaviour of the ratio for two different shapes: spherical (blue dotted curve) and disc like (red solid curve).

$$p_{\max} = \frac{\eta_{\mathrm{v}}}{a_{\mathrm{p}}}\sqrt{\frac{12RT_{\mathrm{avg}}}{M_{\mathrm{a}}}} \tag{6.5}$$

$$F_{\max} = \frac{\pi\eta_{\mathrm{v}}a_p^2\sigma T_2^4}{2\kappa_{\mathrm{S}}}\sqrt{\frac{R}{3T_{\mathrm{avg}}M_{\mathrm{a}}}}. \tag{6.6}$$

Here $\eta_{\mathrm{v}} = 1.7 \times 10^{-5}\ \mathrm{kg\,m^{-1}\,s^{-1}}$ is the air viscosity; $R = 8.3\ \mathrm{J\,mol^{-1}\,K^{-1}}$, $T_{\mathrm{avg}} = 258.8\ \mathrm{K}$ the average air temperature from both particle sides; $M_{\mathrm{a}} = 0.029\ \mathrm{kg\,mol^{-1}}$ the molar mass and $\kappa_{\mathrm{S}} = 0.02\ \mathrm{W\,m^{-1}\,K^{-1}}$ the snow thermal conductivity. The ratio between the photophoretic force and the gravitational force in function of the particle size is shown in figure 6.9. I assumed a volume filling factor of $\phi = 0.05$, a density of $\rho_{\mathrm{S}} = 920\ \mathrm{kg\,m^{-3}}$ and a thickness $d_{\mathrm{a}} = a_{\mathrm{p}}/5$.

For typical sizes of ~ 1 mm or larger, the photophoretic force is not able to make the aggregate levitate. As it can be seen in figure 6.9, this depends on the shape of the particle as well. Since levitation has been observed on aggregates larger

than 5 mm, photophoresis should be discarded as main active process as levitation starts. However, it cannot be neglected for particles smaller than a few tenths of mm. Considering that aggregates are formed by an ensemble of single 1-10 µm particles, the photophoretic force would be able to levitate a whole 5 mm aggregate if we assume that it applies to every single particle. Experiments on $\sim$ 100 μm icy particles, which were created in identical conditions as the particles used in this case, show how photophoresis and thermophoresis can satisfactorily levitate them at much higher heights ($\sim$ 2 cm) than those observed in this work (Kelling et al., 2011; van Eymeren and Wurm, 2012).

Thermophoresis

A particle can be accelerated by thermophoretic forces when it is embedded in a fluid medium with a temperature gradient. The fluid molecules from the warmer part impact on the particle's surface with more momentum than those which do it from the cooler side. This causes a net force on the particle towards the cooler part of the gas (see figure 6.10)

The force produced by thermophoresis on a spherical particle can be calculated by (Zheng, F., 2002)

$$F_{\mathrm{th}} = -f_{\mathrm{th}} \frac{a_{\mathrm{p}}^2 \kappa_{\mathrm{a}}}{\sqrt{2 k_{\mathrm{B}} T_{\mathrm{avg}} / m_{\mathrm{a}}}} \nabla T, \tag{6.7}$$

where f_{th} is a dimensionless factor which depends on Kn; $\kappa_{\mathrm{a}} = 0.02 \mathrm{W\,m^{-1}\,K^{-1}}$, the conductivity of air; $m_{\mathrm{a}} = 4.8 \times 10^{-26}$ kg is the air molecular mass and $\nabla T = 1.15 \times 10^4 \mathrm{K\,m^{-1}}$ the temperature gradient over the particle. As mentioned before, it is very difficult to establish the size of the grains which compose the aggregates. Assuming an ice particle of $a_{\mathrm{p}}^2 = 10^{-6}\,\mathrm{m}$ and considering the conditions above mentioned, the resulting thermophoretic force is $F_{\mathrm{th}} \approx 6 \times 10^{-13}\,\mathrm{N}$. Comparing this with the corresponding gravitational force of the same particle ($F_{\mathrm{g}} = 10^{-14}\,\mathrm{N}$), it is clear that thermophoresis is more than enough to lift a micrometre ice particle. Since thermophoresis in a very open structured aggregate pulls on each individual constituent, as shown in the photopheresis case, different size aggregates are related to different forces. The larger the aggregate, the larger the force. Due to non-sphericity of the grains, there are some force variations which cannot be adjusted to

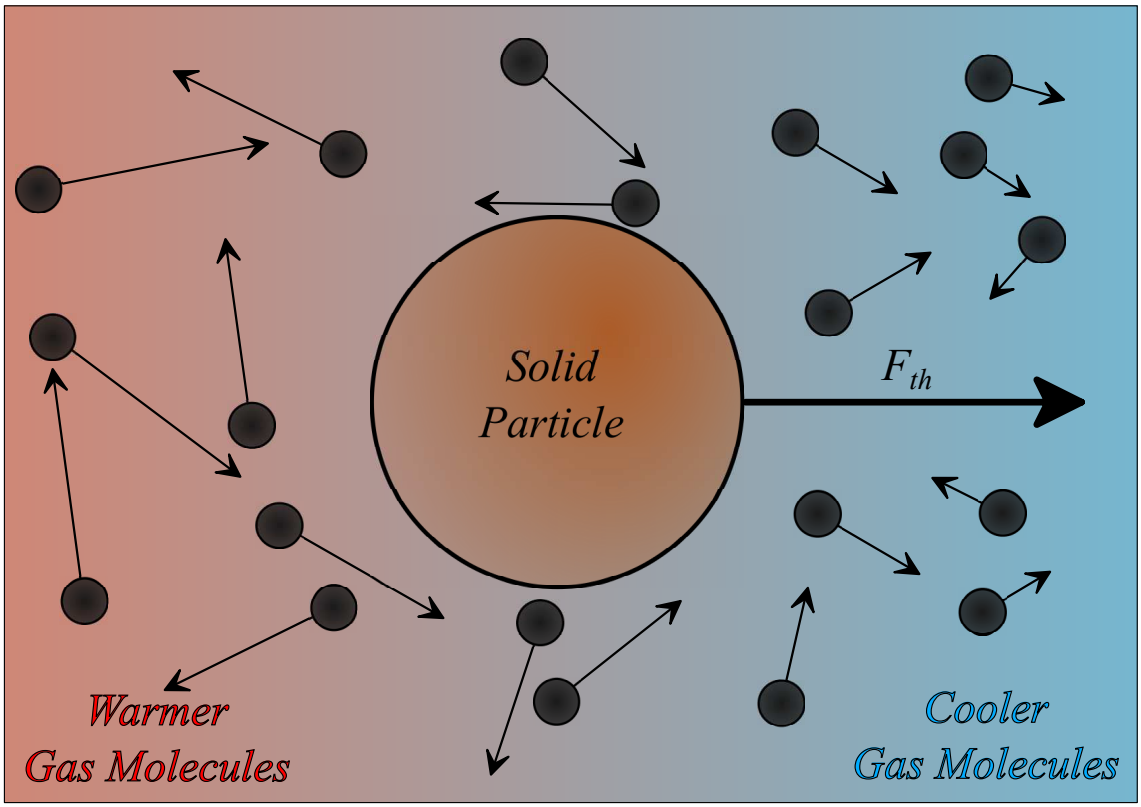

Figure 6.10: Spherical particle affected by thermophoresis. The temperature gradient causes that the gas molecules impact with the grain with higher velocity on the warmer side than on the colder side. This creates a net acceleration directed to the colder side of the particle.

a high degree, but they show some random components. Taking this into account, thermophoresis would definitely contribute to the levitation of the aggregates. It fits the results presented in Kelling et al. (2011) where thermophoresis is the main process of particle lifting.

Sublimating Gas Pressure

When water molecules sublimate, each detached molecule carries some kinetic energy to the whole aggregate towards the opposite direction in which it is ejected. The mass of a single water molecule is negligible compared with the whole aggregate mass, but depending on the sublimation rate, the total amount of momentum carried by the expelled molecules may be important.

The sublimating molecules which move upwards and to the sides can freely follow their path, but those which are forced to go downwards collide with the plate,

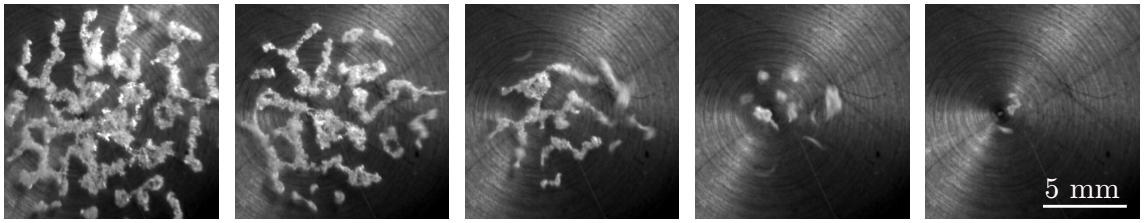

Figure 6.11: (From left to right) sequence of the sublimation process during a single experiment. The time gap between each frame is 11 seconds. The image of the aggregates may at times seem blurred because of the camera exposing time and the aggregate movement.

forming a water gas layer that may cause overpressure enough to make the aggregate levitate. Furthermore, the temperature below the aggregate is higher than at the top of it (as it has been shown previously), causing a higher kinetic energy distribution below the aggregate than above it. This would create an even higher overpressure on the lower part of the aggregate. However, ice aggregates' levitation has been observed at temperatures of $\sim 200\,\mathrm{K}$. At these temperatures, the sublimation rate is not enough to produce an overpressure to overcome gravity. Aggregates under these conditions have been observed levitating during more than one minute, implying a very low sublimation rate. For this reason, sublimation gas pressure would not contribute to the levitation of the aggregates.

6.2 Results: Fragmentation of Ice Aggregates by Sublimation

At pressures of $\sim$ 1 mbar, the ice laid on the plate sublimates in a few minutes. Sublimation progress was recorded for 20 ensembles of aggregates from a top position with an optical system composed by a high speed camera and an objective. In figure 6.11 a sequence of 45 seconds from a single experiment is shown.

For this experiment, the optical system was configured to take movies at 18 frames per second (fps) rate and a resolution of ($21.8\ \mu\mathrm{m\,pixel}^{-1}$). All movies were programmed to have the same duration, storing the last 45 seconds of data once the whole aggregate was completely sublimated. From figure 6.4 it can be seen that the typical thickness of the aggregates is much smaller than its typical total coverage area extension ($\sim$ 10 mm). It is then a reasonable approximation to consider the aggregates as an 2D structure which can be easily observed from the top of the

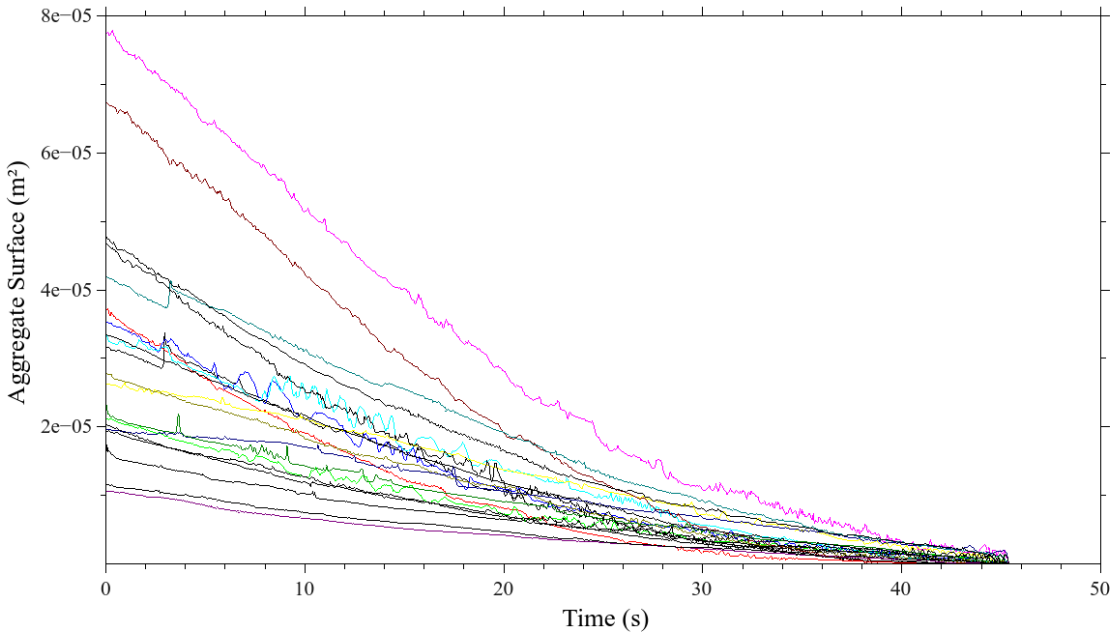

Figure 6.12: This plot shows the rates at which the measured area of different ensemble of aggregates change with time (sublimation rate). All the 20 experiments are plotted simultaneously. In some cases, the measured area increases suddenly. This is due to the entrance of single aggregates which were located outside the field of view of the camera when the sequence started.

setup (see figure 6.2). In figure 6.4 can be also observed that the aggregates are not perfectly uniform along its whole area. That causes a slightly variation on the total time needed to sublimate the whole aggregate and, therefore, slightly different starting ice coverages for each experiment. The shrinkage of the icy aggregates are shown in figure 6.12.

Fitting an appropriate rate's function for each experiment, it is a difficult task because its evolution through time is slightly different. In some, cases a grade two polynomial expression fits properly but for other cases a linear function describes the process more accurate. In order to analyse all the cases, a simple decaying linear fit function has been chosen. However, some of them present a slope change at around 25 seconds after the starting of the recording. In figure 6.13, an evaporation rate plot with a slope change and another with constant linear decrease are shown. Then, the sublimation rates may approximately be described as:

$$b_{\mathrm{a}} = \frac{\mathrm{d}A_{\mathrm{agg}}}{\mathrm{d}t} = \text{constant} \tag{6.8}$$

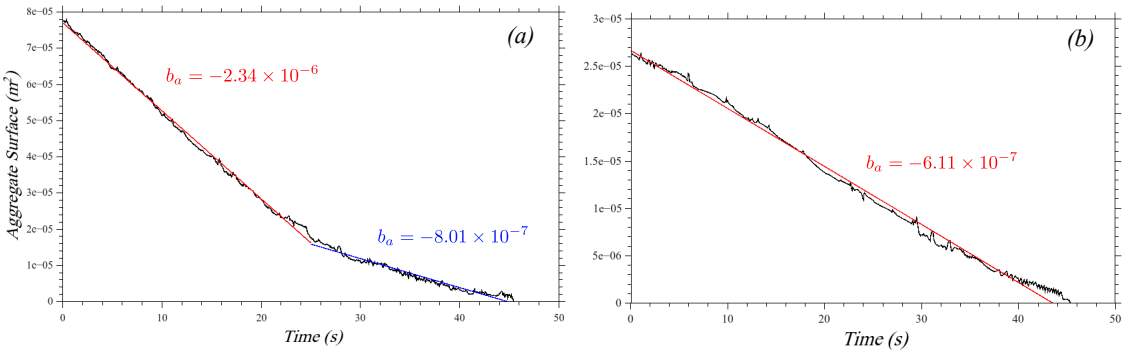

Figure 6.13: Sublimation rates of two single experiments. Left: example of aggregate's ensemble which sublimation rate can be approximated by two different constant slopes. Right: the sublimation rate of this experiment is well described by a single constant slope.

where b_a is the slope of the sublimation rate (or area shrinkage in function of time) $\mathrm{d}A_\mathrm{agg}/\mathrm{d}t$. For the cases where the rate is divided into two regimes, initial b_a values of $0.9-2.4(\times 10^{-6})$ $\mathrm{m^2\,s^{-1}}$ are after the slope change reduced by a factor 3. This feature is common to each experiment where the slope change takes place independently from its starting sublimation rate. For the experiments corresponding to a simple decreasing linear decay, rate values $b_\mathrm{a} = 4.17 - 9.69(\times 10^{-6})$ $\mathrm{m^2\,s^{-1}}$ are measured.

Some empty regions and contact bridges in the coverage area are present and as sublimation goes on, the holes become larger and the contact bridges thinner. Although gravity is compensated by the pressure difference, aggregates' irregularities cause minor lateral forces that may lead to the breakup of contact bridges (if they are thin enough). With the resolution of the optical system employed, it was not possible to establish the typical neck radius at which aggregates parts break apart, but under similar conditions this radius appears to be $\sim 1 - 10$ nm (Aumatell and Wurm, 2014). It is possible to determine the contact radius at the moment of the breakup if the acceleration of the affected parts could be measured. However, the fps rate is to low to appreciate a net acceleration from the separated parts after a breakup.

Breakups are counted during the sublimation of the whole aggregate. That's possible with the subsequent analysis of the movies recorded. In figure 6.14 a sequence of a typical breakup is shown. Observable breakups are counted, where one part of the aggregate completely separates from another part. The optical contrast between the aggregates and the plate is high enough to easily see the separation with the eye. Breakups where two parts of the aggregate separate but remain connected at

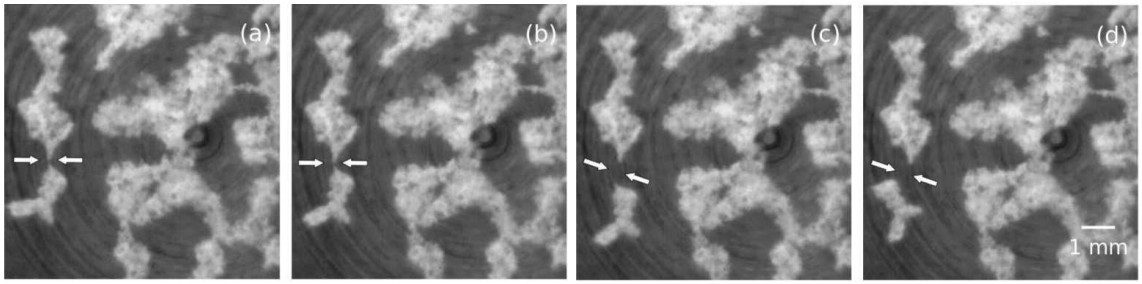

Figure 6.14: Left to right: sequence of an aggregate's breakup. The point where the fragmentation takes place is pointed by two arrows. (a) the aggregate present a neck between its two main parts. (b) the lower part of the aggregate rotates a few degrees but still remains attached to the upper part. (c) the breakup takes place and the two parts drift apart. (d) now both parts are single aggregates that move separately.

another location are counted too. However, such kind of breaks are less than 10 per cent of the whole breakup amount. Although the ice structure is very porous and almost completely flat, vertical breakups and later compaction in regions where thickness is slightly higher may occur, but are expected to be rare. The cumulative breakup rate corresponding to the same single experiment from figure 6.13.(a) is shown in figure 6.15.

From figure 6.15 it can be seen that the breakup rate presents a slope change at about 25 seconds too. This fact indicates a possible dependency of the breakup rate and the sublimation rate. This feature is explained below in more detail.

To compute the total number of breakups of a given size, the breakup rate and the total time an aggregate takes to completely sublimate from the initial size are measured. As aggregate's initial size, is advisable to consider the 2D radius of gyration of the structure at the beginning of the experiment. The radius of gyration is the equivalent radius that an aggregate would have if it would be perfectly circular. This can be defined as:

$$r_{\mathrm{gir}} = \sqrt{\frac{\sum_i (r_i - r_{\mathrm{s}})^2}{N_{\mathrm{p}}}} \tag{6.9}$$

where r_i are the coordinates of the $i-$th pixel covered by ice; r_{s} the coordinates of the center of mass and N_{p} the total number of pixels with ice coverage. The dependence of the ice surface coverage A_{agg} on the size r_{gir} is plotted in figure 6.16.

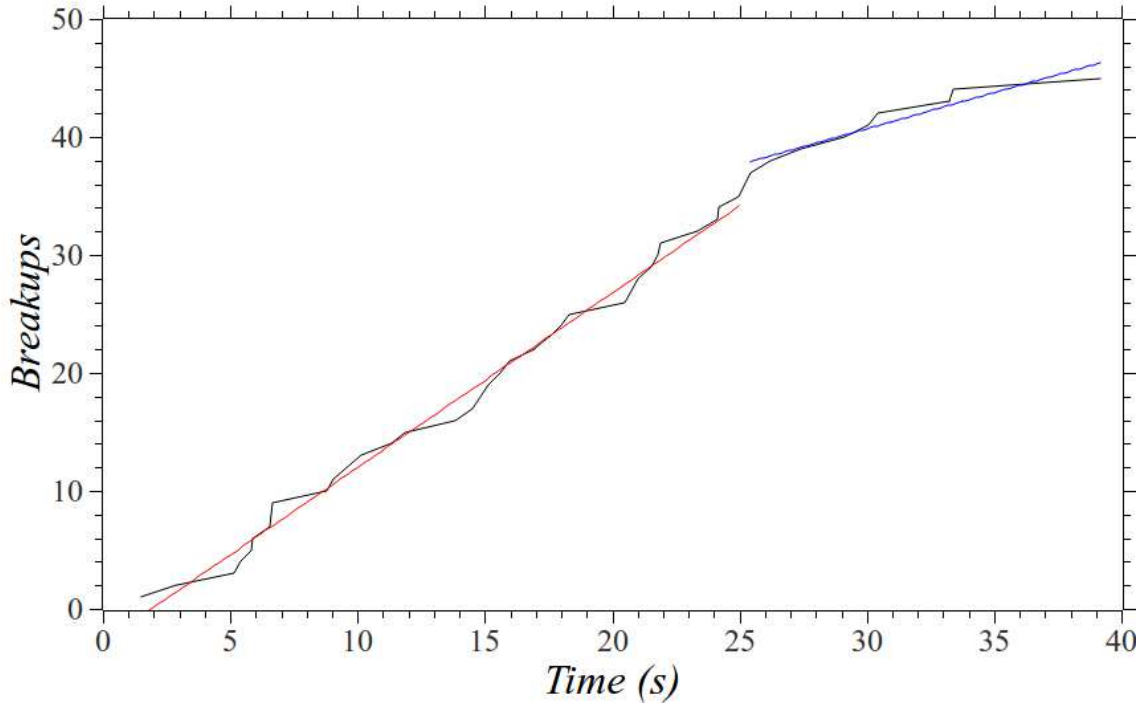

Figure 6.15: Number of breakups over time. Also here a linear dependence can be observed which is split in time in two parts. The split is correlated to the split in evaporation rate of the same experiment (see the left plot of figure 6.13).

The approximated aggregate's area may be expressed as a power law

$$A_{\text{agg}} = c r_{\text{gir}}^{d} \tag{6.10}$$

The best fit from figure 6.16 data corresponds to a $d = 2.0 \pm 0.2$ and $c = 2.20 \pm 0.26$, which is consistent considering the aggregates as porous structures but uniformly extended in 2D, independently of its size.

In some cases, like sublimation rates, breakup rates present two different regimes. In these cases, the second breakup rate is related to the size of the aggregate at the moment of rate's change. If this change is not observed (specially for the smaller aggregates), only one initial size and average breakup rate is taken into account. Figure 6.17 shows how the breakup rate depends on the aggregate's size. In this plot it can be seen that data is gathered into two main populations. The average breakup rate from each population differs approximately by a factor 3, which is the same factor found in the evaporation rate exposed above. It shows a clear correlation between both variables that, in these experiments, do not seem to show

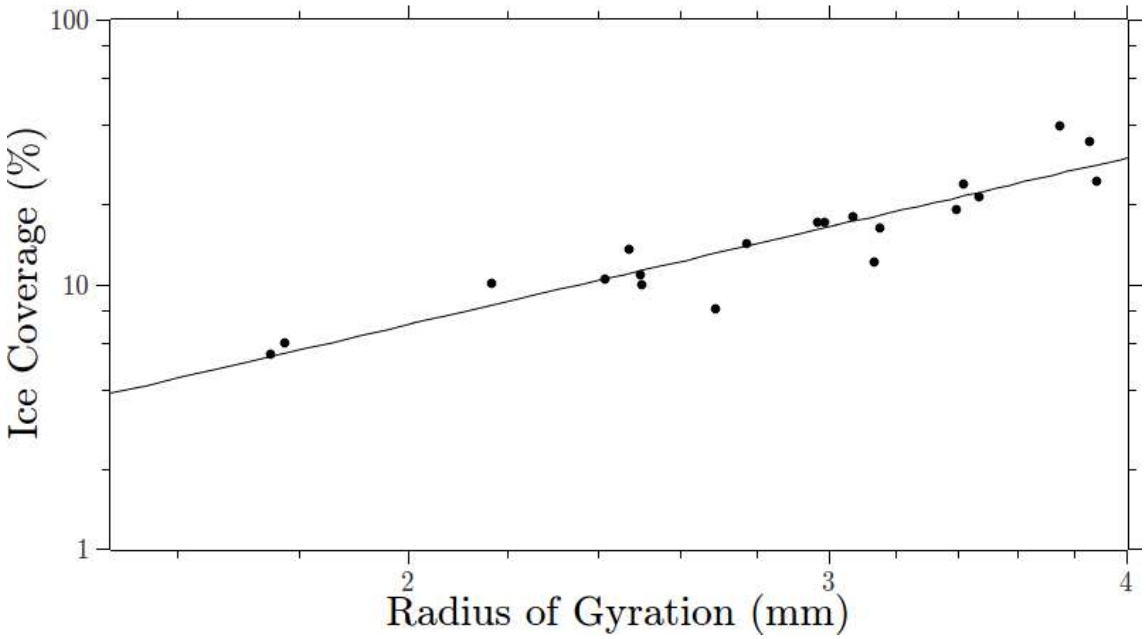

Figure 6.16: Area covered by ice versus the size of an aggregate at the beginning of an experiment. Each data point represents an individual experiment. Both axis are plotted in logarithmic scales.

a clear dependence on size.

However, it must be remarked that these features have been found for the present work. The same experiment, applied to ice aggregates grown using a different technique, may yield other results. In this particular case, individual grains have size distribution ranged between several and a few tens of microns, though the latter might already be small aggregates (see firgure 6.3). That directly implies a distribution on the contact areas or necks between the contacting icy grains. This distribution determine the breakup rate in detail and, for the present experiments, it forces the breakups to proceed continuously in time with some statistical variation. These contact areas are smaller than 0.1 μm (Aumatell and Wurm, 2014) and cannot be resolved by optical methods, for these reasons an average value of the breakup rate is assumed for all the experiments. Individual experiments with similar initial sizes differ in a factor 3 in some cases, as it can be seen in figure 6.17, and a more complex breakup rate dependency on size would be possible within the uncertainties of the data, but the considered simplification allows us to estimate the total number of breakups for a given aggregate's size and to extrapolate it to larger icy bodies.

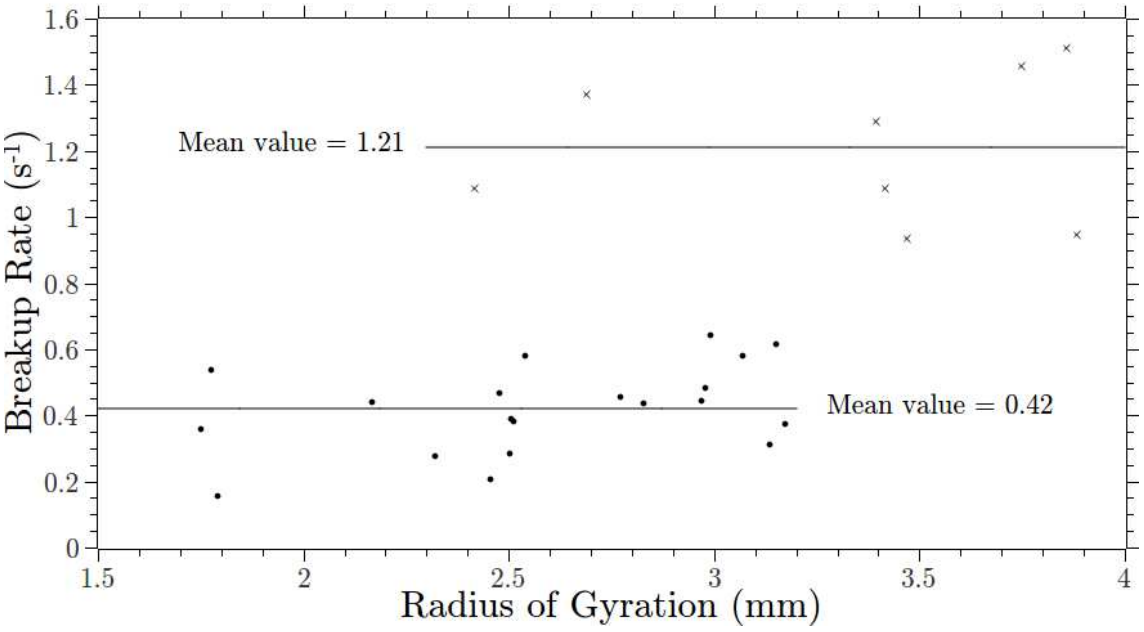

Figure 6.17: Breakup rate for ice aggregates with different initial size. Upper and lower values are correlated to the difference in sublimation rate. Each data point corresponds to a different experimental run. Solid lines mark average rates.

6.3 Discussion

6.3.1 Analysis of Sublimation

As it has been proposed by Saito and Sirono (2011) and by Sirono (2011a) -the later including sintering-, ice aggregates fragment when they sublimate. This would produce a number of smaller aggregates which eventually are reduced to single dust cores with an icy mantle. The experiments described in the sections above support this scenario where breakup is indeed a process which would increase the density of solid particles close to the snowline.

It is expected that the total number of breakups does not depend on the time that the aggregate takes to sublimate, nor the sublimation rate neither the breakup rate. Assigning an average breakup rate $n_{\rm br}$ for each regime, the total number of breakups $N_{\rm br}$ after a certain time t can be written as:

$$N_{\rm br} = n^{\rm br} t, \tag{6.11}$$

where t is the time during which the aggregate fragments at a breakup rate n^{br}. Integrating equation 6.8, the time t may be stated as $t = A_{\mathrm{agg}}/|b_{\mathrm{a}}|$, where A_{agg} is the aggregate's surface. As it has been pointed out, the aggregte's surface may be expressed as $A_{\mathrm{agg}} = cr_{\mathrm{gir}}^2$ (see equation 6.10), then the sublimation time for a given breakup rate is $t = cr_{\mathrm{gir}}^2/|b_{\mathrm{a}}|$. Substituting this in equation 6.11, the total number of breakups is

$$N_{\mathrm{br}} = \frac{n^{\mathrm{br}} cr_{\mathrm{gir}}^2}{|b_{\mathrm{a}|}}. \tag{6.12}$$

It must be noticed, that the breakup rate n_{br} scales with a factor 3 for each regime. This is correlated with the sublimation rate b_{a} which scales with the same factor. That implies that equation 6.12 is only dependent on the initial size r, as it has been mentioned above. Defining the constant parameter $\chi = n^{\mathrm{br}} c/|b_{\mathrm{a}}|$, the total number of breakups is

$$N_{\mathrm{br}} = \chi r^2 \tag{6.13}$$

Using the measurements obtained from the experiments, the defined constant takes the value $\chi \simeq 2\,\mathrm{mm}^{-2}$.

The aggregate samples from the experiment are effectively a 2 dimensional scenario with a bi-dimensional projection of ice which is proportional to the square of the size. As it has been pointed out in section 3.1, during the first steps of planetesimal formation, particles in a PPD grow via cluster-cluster aggregation (CCA) (Blum and Wurm, 2008). This process leads to the formation of aggregates with a fractal structure. Experimental results show that fractal dimension of 3 dimensional millimetre sized aggregates formed this way is $\sim 1.7 - 1.9$. Since the projected surface of a 3 dimensional structure with a fractal dimension $D_f = 2$ it is also scaled with dimension 2, it is plausible to extrapolate the observed results form the present experiment to the aggregates in a PPD. Taking this into account, the total number of pieces which a CCA cluster will breakup into, can be estimated once the sublimation process starts, i. e., when the aggregate crosses the snowline inwards (fig. 6.18)

This principle is not applicable to all sizes. The structure of icy aggregates change when they grow and the fractal dimension does not remain constant. Although here cm-sized aggregates have been studied, fractal growth could continue to much

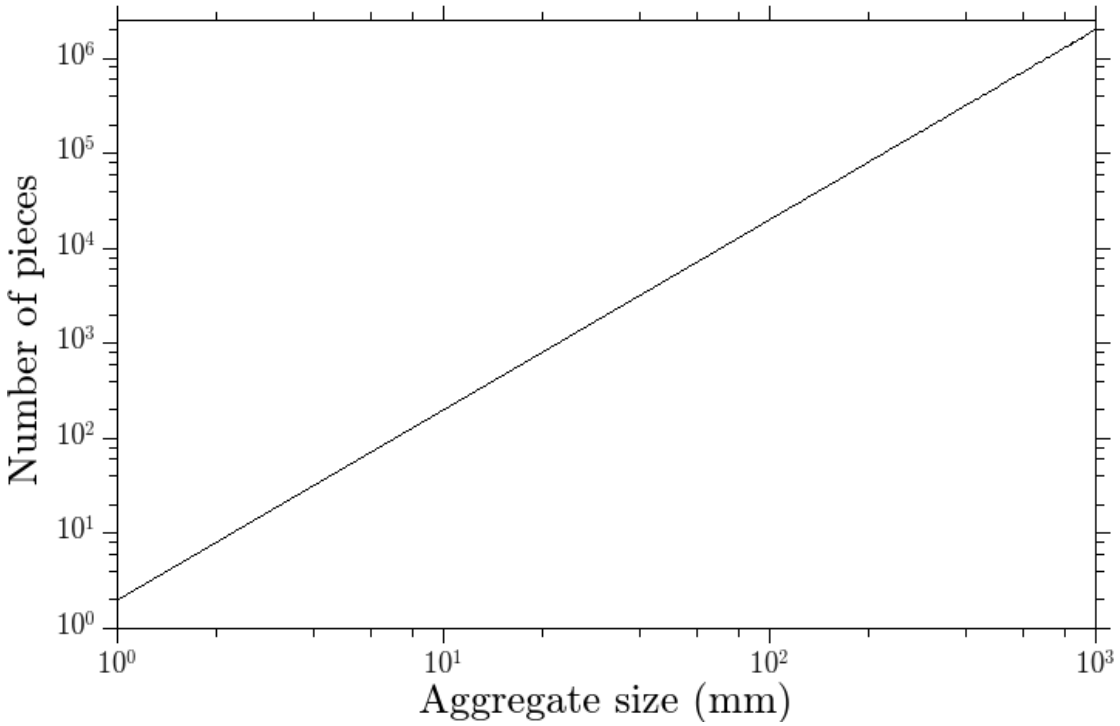

Figure 6.18: Number of fragments due tu sublimation over the initial aggregate's radius. The plot follows the relation 6.13.

larger sizes (Okuzumi et al., 2012). Collision events, which lead to coagulation, may increase the filling factor of the resulting aggregates by restructuring processes if the impact energy is high enough. This yields a higher aggregate's fractal dimension that could modify the sublimation and fragmentation rate of the whole structure.

Other processes related to water ice in PPD like condensation (Ros and Johansen, 2013; Sirono, 2013), sintering (Sirono, 2011a) and amorphous-crystalline phase transition -both ice phases have been observed around a type II YSO (Schegerer and Wolf, 2010)-, modify the structure of the growing aggregates. The changes in the structure affects the whole aggregate's effective ice surface and consequently the sublimation and fragmentation rate.

The aggregates generated for this experiment are assumed to be closely resembling drifting solids in PPD. In detail, the total number of breakups and resulting fragments may differ from the experimental results obtained. However, equation 6.13 might be a suitable approximation. Here, I have assumed that the ice aggregates dust particles are embedded in ice mantels (see figure 6.1). But through the experiments it is not possible to determine the final structure of the released dust

aggregates.

The main idea suggested by Saito and Sirono (2011) and Sirono (2011a) is that the resulting released aggregates drift slower inwards. The drift velocity of a solid body depends on the gas-grain coupling time. Since the gas-grain coupling time for an overall CCA size does not change (Blum and Wurm, 2008), their drift velocity would remain constant. This fact may be explained arguing that the gas-grain coupling time is directly proportional to $M_\mathrm{a}/A_\mathrm{a}$ being M_a the aggregate mass and A_a the aggregate cross-section. For compact solids, the mass scales as $M_\mathrm{a} \propto r^3$, thus $M_\mathrm{a}/A_\mathrm{a}$ changes linearly with the overall radius of the aggregate. This would imply that smaller fragments drift slower than the original large icy body.

Independently from the details that ice aggregate morphology imply in the sublimation and breakup rate (including dust cores), it is evident that fragmentation of ice aggregates due to sublimation close to the snowline will inevitably occur, leading to a density enhancement of solid material on this region of the PPD.

6.3.2 Analysis of Collisions

The characteristics of the obtained data are not suitable for a deeper study of collisional effects. However, during the sublimation process, many collisions between mm fluffy aggregates have been observed. Although the study of collisions of water ice projectiles has been mainly done by theoretical methods (e. g. Dominik and Tielens, 1997; Schäfer et al., 2007), as mentioned in section 4.1, some experiments have been carried out in order to study the outcome of icy bodies collisions. In almost all this works -except for Shimaki and Arakawa (2012)- no net aggregation has been observed. The most obvious explanation to this fact is that the targets used for the impacts have no or very low porosity. However, results from Shimaki and Arakawa (2012) show that for cm sized ice spheres with a filling factor $\phi \leq 0.4$ sticking events with restructuring take place. The sticking probability decreases with the velocity and the projectile mass (see figure 3.4).

In the present work, the maximum hit velocity in such events is $\sim 2\ \mathrm{cm\,s^{-1}}$, what corresponds to low velocity collisions in terms of protoplanetary disc and planet formation. The filling factor is assumed to be $\phi < 0.1$ (from the ice formation method), with masses that do not exceed 10^{-12} kg (or are not larger than 1 mm in size). Considering the above mentioned conditions for events where sticky impacts

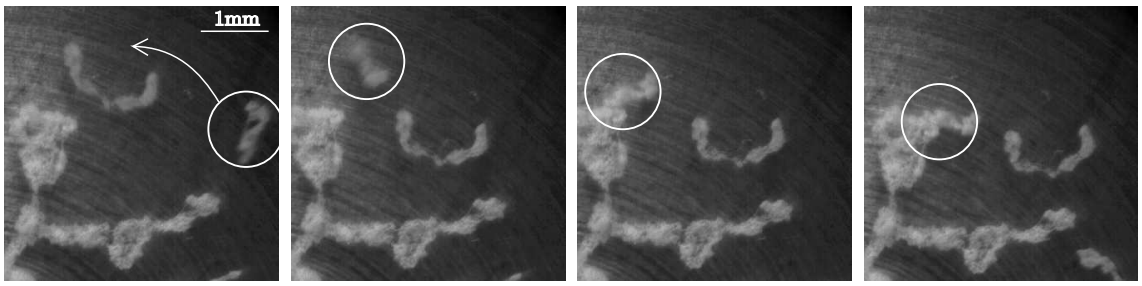

Figure 6.19: From left to right: sequence of a collision between two aggregates. A 1 mm aggregate (white circle) impacts with a larger structure at $\sim 2\,\mathrm{cm\,s^{-1}}$ and remains attached.

have been observed, collisions of ice aggregates within the present work would lead to a high stick efficiency. In fact, no bouncing event have been registered during the analysis of all recorded experiments. This implies a 100 % stick efficiency for impacts between mm size ice aggregates and $\phi \leq 0.1$ at velocities of 2 $\mathrm{cm\,s^{-1}}$ or lower. Restructuring of the aggregates has not been studied due to the resolution of the optical system employed. However, no structural change has been observed on the particles after collisions. In any case, these events are not expected to cause any change within the core structure of the aggregate at low impact velocities.

Considering these results, it is plausible to assume that planetesimal growth during the first epoch close to the snowline should be relatively quick. In the coagulation model proposed by Ros and Johansen (2013), mm ice particles can grow up to dm ice boulders in 1000 years. Nonetheless, in this model, collisions are not considered and particles are treated as massive spheres. It has been seen that for solid particles of size 1 mm, their relative velocity would be $\sim 1\,\mathrm{m\,s^{-1}}$ (e.g. Windmark et al., 2012). Shimaki and Arakawa (2012) reports that collisions between ice aggregates with a $\phi = 0.3$ and a radius of 1.5 cm, can result in stick events at velocities of $4\,\mathrm{m\,s^{-1}}$. If mm porous particles are considered, their relative velocity would be even lower than $1\,\mathrm{m\,s^{-1}}$ because they are stronger coupled to the gas (Blum and Wurm, 2008). Including collisional events, under these conditions, in the model proposed by Ros and Johansen (2013), the growth rate would be even larger.

Another important effect that should be considered in collisional processes is sintering (Sirono, 2011a). Since the influence of sintering in the present experiments does not seem to affect the results clearly, it should also be taken into account in growth models if relative large timescales are considered. Sintering broadens the contact areas between the grains, providing more rigidity. This causes a higher resistance

to roll and twist (Dominik and Tielens, 1997). Collisions between ices considering sintering have been carried out by Shimaki and Arakawa (2012), but from their results there is no clear inference of sintering on impact outcomes. However, it should be expected that the probability of bouncing events increases as the colliding ice aggregates are longer exposed to sintering.

6.4 Conclusions

When ice aggregates beyond the snowline exceed the gas coupling critical size, they start to drift inwards. If they cross the snowline, a large number of embedded dust particles will be released as the ice mantle sublimates (Sirono, 2011a; Saito and Sirono, 2011). The released dust particles are much smaller than the original aggregate and their drift velocity is dramatically reduced. For a MMSN model, at 3 AU of distance, with a surface mass density $\Sigma = 1700\,\mathrm{g\,cm^{-2}}$ and a temperature profile of $T = 200(r/1\mathrm{AU})^{-1/2}\,\mathrm{K}$, the radial velocity drops from $30\,\mathrm{m\,s^{-1}}$ for a 100 cm solid to less than $1\,\mathrm{m\,s^{-1}}$ for a 1 cm body. Through more frequent sticking collisions or due to gravitational instabilities, a dust density enhancement close to the snowline will occur. This increases the likelihood of planetesimal formation. The fragmentation process caused by sublimation proposed by Saito and Sirono (2011) would lead to the release of embedded dusty particles. The laboratory experiments presented in this chapter verify that ice aggregates breakup upon sublimation and, furthermore, the fragmentation in a larger number of smaller aggregates has been observed.

As theoretically expected, the total number of breakups (and so remaining fragments), is independent on the sublimation and breakup rate. Specifically, putting this into PPD context, a 10 cm CCA solid would fragment into $\sim 2 \times 10^4$ pieces (see equation 6.13). It must be pointed out that this experiment has been carried out only with water ice aggregates. If dust particles would have been present, it is difficult to predict which would be the final structure of the remaining aggregate after the sublimation of the ice.

Regarding the growth rate, it has been seen that for fluffy ($\phi \leq 0.1$) millimetre water ice aggregates, low collisions lead to a 100 % stick efficiency. If this fact is considered for icy planetesimal growth models based on condensation (Kuroiwa and Sirono, 2011; Sirono, 2013; Ros and Johansen, 2013), the growth rate would be considerably

enhanced. However, larger icy aggregates formed by collisional processes would have larger filling factor, due to restructuring compaction. If, in addition, sintering effects are also considered, bouncing events between equal sized icy aggregates collisions are expected (Shimaki and Arakawa, 2012). Furthermore, if the impact velocity is relative high, fragmentation events would also be frequent. Therefore, fast and effective growth of ice aggregates via collisions, as it has been observed in the present work, are only applicable at regions where CCA ice aggregates are generated via hit-and-stick processes at the very beginning of planetesimal formation.

Chapter 7

Experiments on Contact Forces between Ice Aggregates

The importance of aggregation in the context of planet formation has already been shown in this work. There is a general acceptance among all specialists that the *seeds* of the first planetesimals are fluffy aggregates that form via hit-and-stick processes resulting on CCA aggregates. As it has been mentioned in section 3.3 the outcome of collisions between aggregates depends on several variables and it is difficult to compute. One of these variables is the force of the contacts between the grains from which the impacting bodies are formed. For dusty aggregates, van der Waals forces keep particles together, while for ice grains, dipole forces apply a higher attraction on contact regions (Wang et al., 2005). The strength of these contact forces determine the threshold beyond which the aggregates may restructure or even breakup under different interactions like collisions or gas pressure differences induced by sublimation and temperature gradients.

In chapter 5 are exposed the theoretic aspects on which the actual aggregation models are based. Since interactions regarding to contact forces present three degrees of freedom, specific models have been proposed to explain the face-on case (e.g. Johnson et al., 1971; Chokshi et al., 1993; Krijt et al., 2013), the rolling case (Dominik and Tielens, 1995) and the sliding/twisting cases (Dominik and Tielens, 1996). Some other models consider all possible degrees of freedom to apply them to a single coagulation theory (e.g. Dominik and Tielens, 1997; Wada et al., 2007). However, it is not clear what is the smallest size to which models can be applied. To prove their range of validity, laboratory studies have to be performed in order to compare the

both theoretical and experimental results. Some experiments have been carried out to determine the pulling contact forces (or stickiness) between micrometre spherical solid particles (e.g. Heim et al., 1999; Poppe et al., 2000) and seem to be in relative agreement with models. Rolling experiments also present a relative good accordance with theoretical predictions (Heim et al., 1999; Ding et al., 2007), as well as for sliding and twisting processes (Sümer and Sitti, 2008). Excluding face-on interactions, there is a lack of laboratory studies if water ice is put into contact forces context regarding rolling (Gundlach et al., 2011), sliding and twisting.

To my knowledge, data related to twisting, specially on the nm-scales, is not available yet. At such scale sizes, the equipment employed to determine contact forces is based on atomic force microscopy. A typical handicap of atomic forces microscopes (AFMs) is that the cantilever used for the measure of the force, as used by Heim et al. (1999), is fixed and not able to rotate freely. In this chapter I describe a new method to measure the minimum values of torsion and rolling torques as well as breakup forces for water ice aggregates. It must be pointed out that measures reported here are applicable to contacts of nm-scales for water ice, but the extrapolation to other contact sizes and materials are discussed in the present chapter.

7.1 A Thermal Gradient Force Microscope

AFMs measure the deflection of a laser beam produced by the bending of a cantilever under a certain load (see figure 7.1). AFM are characterized by a very well defined contact forces applied under pulling or loading forces. Since the sample is fixed in two points and it is not able to rotate freely around a single contact, twisting around a single contact doesn't have an easy measurement.

In order to study the rotation around a contact, the probing "tip" has to be able to rotate freely, i.e. following the motion of a particle being in contact with a surface or another particle. At the same time, the "tip" has to be able to apply a force and also a torque if torsion motions are the object of study. In this case, a free floating probe would act as a cantilever assuming an AFM analogy. This probe has to be attached to the measuring contact and external force field has to induce a pulling impulse and provide a torque. Instead of a cantilever, the easiest way to track the motion of the probe is by using an optical microscope.

The pull-off force of a contact F_c can be determined by observation of the probe's linear acceleration a_p if the contact breaks and its total mass m_p is known. This can be written as:

$$F_c = m_p a_p \tag{7.1}$$

The torque M may be calculated measuring the probe's angular acceleration α_p around a defined axis and its moment of inertia I_p around the same axis. This can be expressed as:

$$M = I_p \alpha_p \tag{7.2}$$

The considered axis depends on which torque it has to be measured. For the rolling case, the oscillations around horizontal axis is considered, while for twisting motions the rotation around vertical axis is chosen (see below). With the setup used in this experiment (see figure 7.2), microscopic motions of the probe are required to detect the movements. The breakup force can only be measured once the studied probe is detached from the whole sample and, after that, the probe in question cannot be recovered.

7.2 Experimental Setup

For this experiment, the setup used is very similar to the one described in the previous chapter (see figure 6.1.1). The upper lid with the liquid nitrogen attached was modified (see figure 7.2). Further modifications made to the setup are:

- The Peltier element and the cooling system was completely removed.
- An horizontal oriented copper plate is attached to the liquid nitrogen reservoir at 4 cm below. On the bottom side of the plate, a heating foil is adhered in order to create a temperature gradient above the plate.
- A 2×4 mm cylindrical temperature sensor is situated just above the plate and acts as a target for the aggregating ice particles. That allows to have a solid

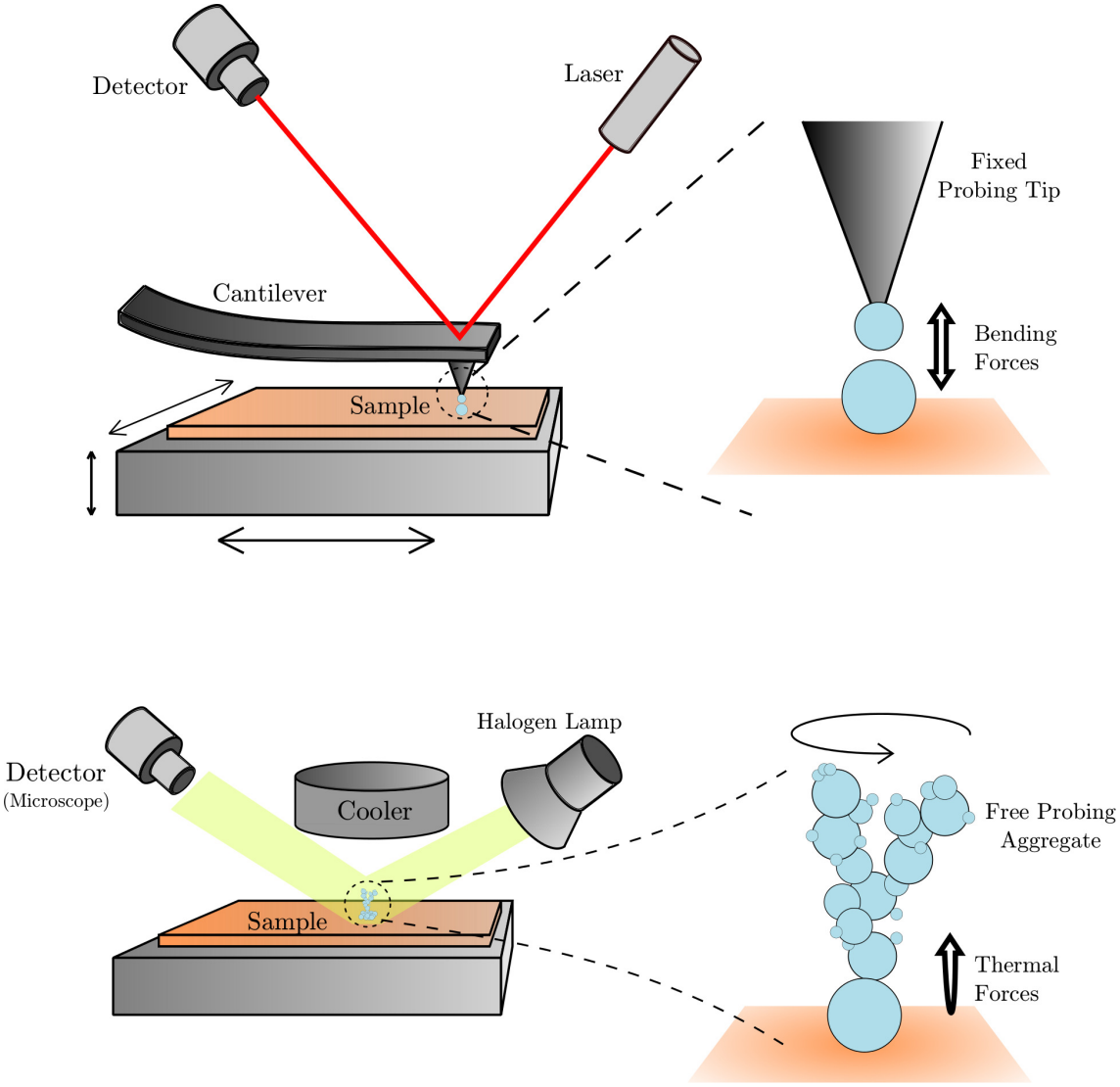

Figure 7.1: Comparison between an AFM and the thermal gradient force microscope. While an AFM works by the light deflection produced by the reflection of a deforming cantilever, the thermal gradient microscope uses a free floating probe (aggregate) to measure pull-off force, rolling torque and twisting torque.

platform where ice particles coagulate for a later observation and to know at which temperature the formed aggregates can be found.

The main vacuum chamber was attached to a water droplet generator (commercial electric inhaler) used to create the ice aggregates (see section 7.3). The temperature sensor, which acts as condensation target for the ice aggregates, is placed in the region where the temperature gradient is generated, i.e. between the bottom part of the liquid nitrogen depot and the copper plate. The ice aggregates are imaged

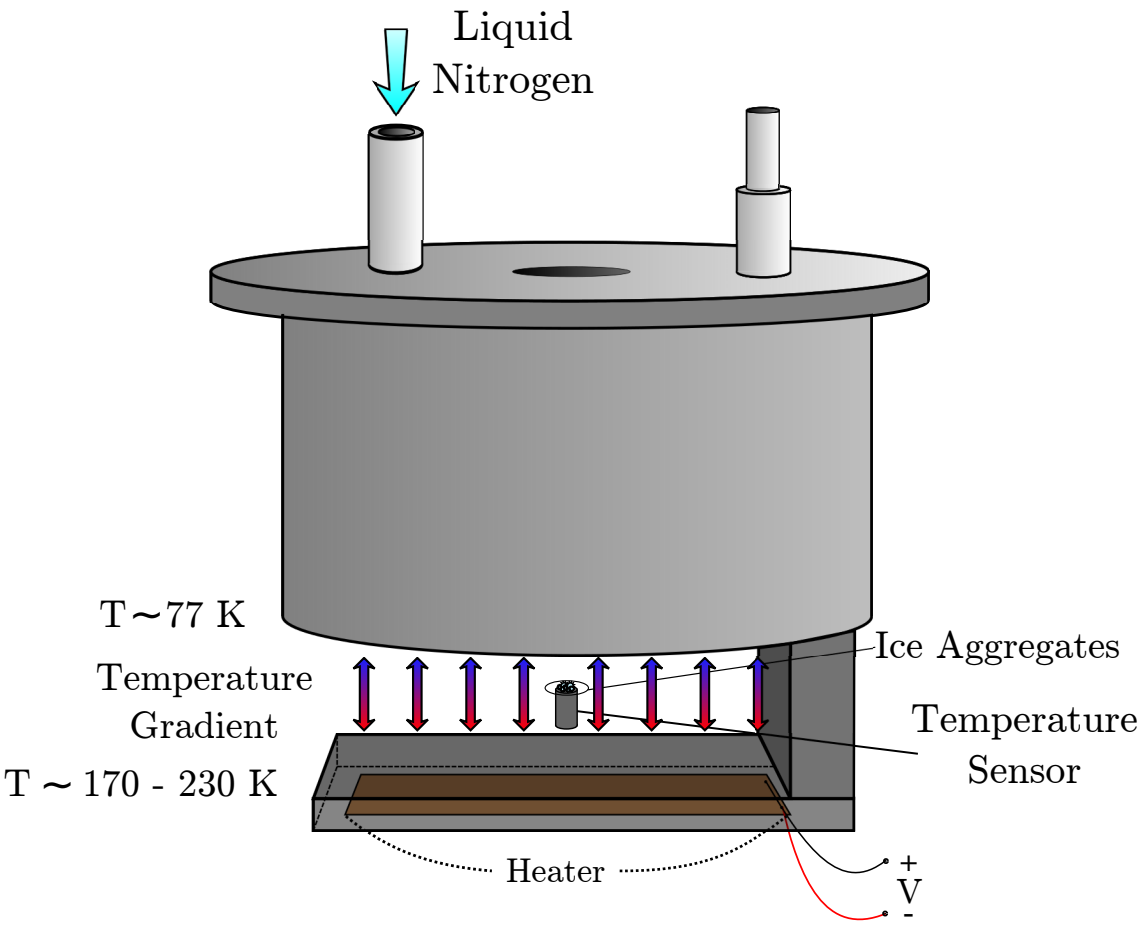

Figure 7.2: A container attached to the upper lid is filled with liquid nitrogen. An aluminum plate, attached to the container, is placed at a few centimetres under the liquid nitrogen reservoir. On the inferior side of the plate a heat foil is adhered in order to produce a temperature gradient between the plate and the container. The analysed ice aggregates are formed on the temperature sensor that is located on the gradient field. The sensor's position and the distance between the plate and the container could be regulated to optimize the thermal gradient forces.

by a long distance microscope with a working distance of 18 cm. Aggregate images are based on a bright field (created by a halogen lamp) with the particles being the silhouette in front of the light source. Depending on the desired interaction to analyse, the camera's frame rate was manipulated between 2 frames s^{-1} (for the study of sublimation rate), to high-speed observations at 800 frames s^{-1} (for the analysis of rotation and breakup events). A general sketch of the complete experimental setup can be seen in figure 7.3.

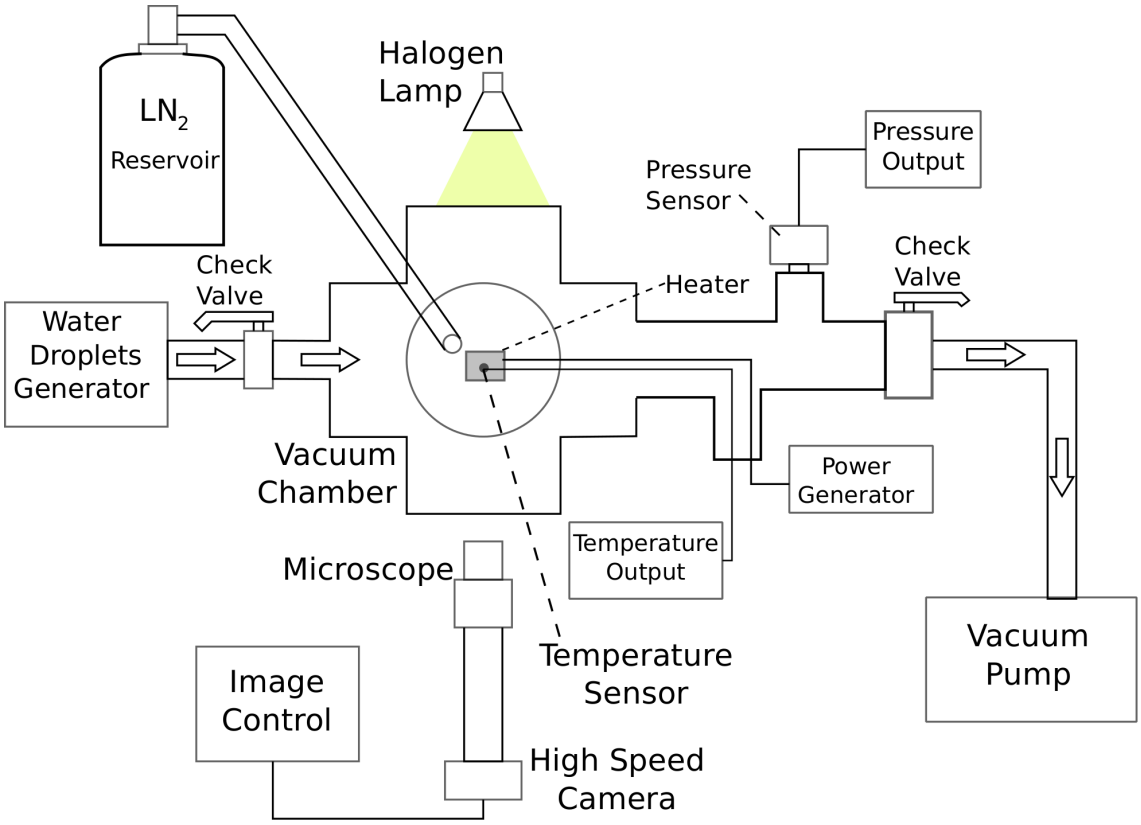

Figure 7.3: Overview of the main experiment components.

7.3 Generation of Ice Aggregates

With the water droplet generator, liquid droplets are introduced into the vacuum chamber through a tube of 10 cm length. The chamber was previously cooled down to temperatures of $\sim$ 180 K and pumped to pressures of $\sim$ 0.1 mbar. Under this conditions, the water droplets become frozen particles when they enter into the chamber. In figure 7.4 it can be seen the size distribution of the droplets formed by the generator, showing a peak of the fitted function at 2.1 µm.

Short after the droplets' injection, the pressure inside the chamber increases up to atmospheric values ($\sim$ 1000mbar). Under these conditions, turbulence inside the chamber leads to collisions between ice particles and the subsequent growth of aggregates via hit-and-stick events begins. After a few minutes of injecting droplets the surface of the temperature sensor that acts as a target (like other regions of the chamber), is covered by a layer of ice aggregates. The thickness of this aggregate layer depends basically on the deposition time and on the injection rate, with sizes ranging between some μm to a few mm. A sample of ice aggregates generated

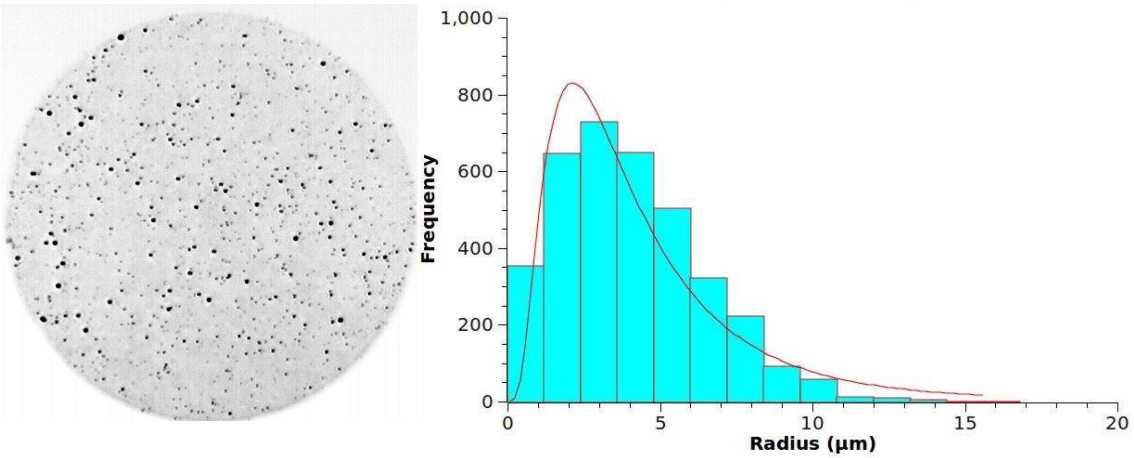

Figure 7.4: Left: example of liquid water droplets, generated by the droplet generator, used to form ice aggregates. Right: size distribution of water droplets.

following this method is shown in figure 7.5. As the temperature sensor is used as substrate for the ice aggregates, the temperature of the aggregates is known at any moment. After the formation of the aggregates, the chamber is evacuated to pressures between 0.1 and 1 mbar. Under these conditions thermophoretic forces act on the ice particles in a measurable magnitude (see section 7.4). During the evacuation of the chamber, it has been observed that the shape of the ice aggregates slightly changed. The average particle thickness increases a few microns due to internal pressures. This expansion ceases once it is achieved a pressure equilibrium between ice particles internal pressures and external pressures air pressure inside the chamber.

7.4 Thermophoretic Forces

As shown in detail in figure 7.1, thermophoretic forces caused by a thermal gradient is used as an external force field on an aggregate in a low-pressure ambient ($\sim$ 0.1 - 1 mbar). This process is described in detail in section 6.1.3. According to equation 6.7, the force applied to a 1 µm ice grain for this experiment is $\approx 2.3 \times 10^{-13}$ N, enough to accelerate the ice aggregates.

Since microscopic ice aggregates are used as probes and the probe is made of the same material as the model sample, it actually provides the contacts. The ice aggregates used are non-symmetric. This means that thermophoretic forces also

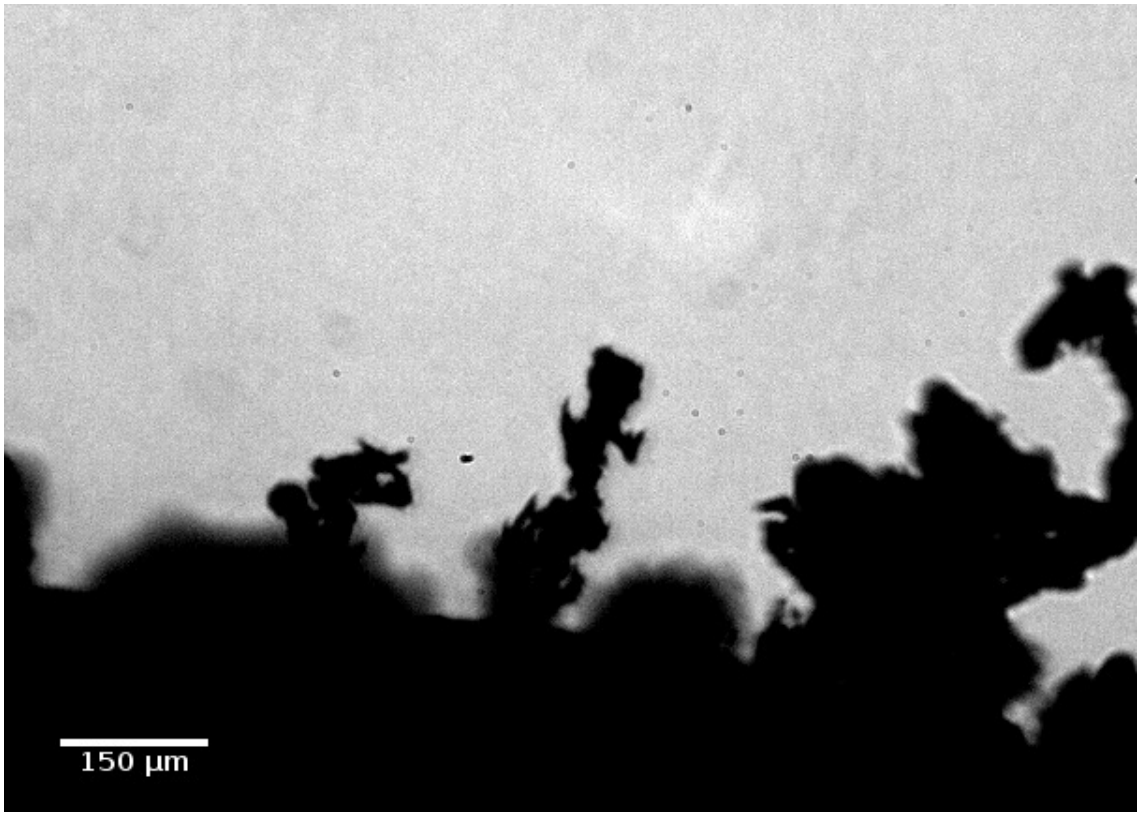

Figure 7.5: Sample of ice aggregates generated on the temperature sensor.

show components perpendicular to the direction of the temperature gradient. This always leads to a small random twisting torque around the vertical (direction of temperature gradient; van Eymeren and Wurm (2012)). It is this torque the one which allows a measurement of the strength of a contact with respect to twisting. Besides contact physics (the focus in this chapter), the observations also provide means to study the thermophoretic forces and torques and from rotation frequencies in equilibrium, the rotational gasgrain coupling times. More detailed description on this aspect is sketched in section 7.8.2.

7.5 Sublimation

For pressures at which the experiment takes place and at temperatures of 180 K, the sublimation rate of ice solids is not high enough to be appreciated visually (for μm sized aggregates at time-scales of seconds). In this experiment, sublimation is used to reduce the contact size between particles but the temperature gradient is kept

constant. Using this method, the contact area between particles keeps decreasing until the applied torques and pulling forces, produced by the temperature gradient, are higher than the contact strength. For aggregates which presented twisting motion, it may contribute to the contact size reduction between the onset of twisting and the moment at which the aggregate breaks up (see figure 7.7, top). The contact size difference during this interval is measured and calculated as follows. Aggregated particles forming aggregates are considered to be homogeneous spheres generated by frozen water droplets. Saito and Sirono (2011) demonstrated that the radius of a water ice homogeneous sphere R_{p} varies through time as:

$$\frac{\mathrm{d}R_{\mathrm{p}}}{\mathrm{d}t} = -\frac{P_{\mathrm{ev}}(T) - P_{\mathrm{H_2O}}}{\rho_{\mathrm{H_2O}}}\sqrt{\frac{m_{\mathrm{H_2O}}}{2\pi k_{\mathrm{B}} T}} \tag{7.3}$$

where $P_{\mathrm{H_2O}}$ is the partial H_2O vapour pressure; $\rho_{\mathrm{H_2O}} = 0.92$ is the density of the water ice; $m_{\mathrm{H_2O}} = 3 \times 10^{-26}$ Kg the mass of a water molecule; T the ice sphere temperature and P_{ev} the equilibrium vapour pressure which has a temperature dependence (Yamamoto et al., 1983)

$$\begin{aligned}\log_{10} P(T)_{\mathrm{ev}} = &- 2445.5646/T + 8.2312 \log_{10} T - 0.01677006T \\ &+ 1.20514 \times 10^{-5} T^2 - 3.63227\end{aligned} \tag{7.4}$$

Equation 7.3 shows that the radius reduction of the ice sphere doesn't depend on the absolute radius of the particle. The shrinkage of various individual ice droplets were tracked in order to determine the sublimation rate for the conditions under which the experiments were carried out. Measuring the required time Δt for the droplet to shrink from a radius R_1 to a radius $R_2 < R_1$, the sublimation rate found at 203 K and a chamber pressure 0.66 mbar, is $\mathrm{d}R_{\mathrm{p}}/\mathrm{d}t = 0.032 \pm 0.014$ $\mu\mathrm{m\,s^{-1}}$. Taken from equation 7.4 where $P_{\mathrm{ev}} = 0.025$ mbar if $T = 203$ K. Substituting this value into equation 7.3, the partial water pressure $P_{\mathrm{H_2O}}$ is almost indistinguishable from P_{ev}, implying practically saturated conditions.

However, equation 7.3 is only valid for sub-μm or larger particles. Ice particles associated to the contact forces on breakup, rolling and twisting forces measured in the present work, give sizes of the order of $\sim$ nm (see section 7.6). At this size scale, vapour pressure and hence the sublimation rate depend strongly on the surface

curvature K_c. For such cases, the equilibrium vapour pressure P_s is (Sirono, 2011b)

$$\ln\left(\frac{P_s}{P_{ev}}\right) = K_c \frac{\gamma v}{k_B T}, \tag{7.5}$$

where γ is the ice's surface energy and v the molecular volume. In this case, the vapour pressure P_{ev} must be replaced by P_s instead. Assuming that the curvature of the nm-contacting particles is $K_c \sim 1/R$, being R the reduced radius of the contacting grains, the sublimation rate can be written as

$$\frac{dR_p}{dt} = -\frac{\sqrt{\frac{m_{H_2O}}{2\pi k_B T}}}{\rho_{H_2O}} \left(P_{ev} e^{(A/R)} - P_{H_2O}\right) \tag{7.6}$$

where $A = \frac{\gamma v}{k_B T}$. Equation 7.6 is used to estimate the size of the contacting grain sizes when twisting motion sets in. The usual time interval between the twisting onset and the breakup moment for a same aggregate is ~ 0.1 s. Sublimation during this time gap does not modify the structure of the whole aggregates which are at least several microns in size. Hence, it is reasonable to consider that forces and torques induced by thermal gradient do not change during this short time period. This has been visually validated by observing no appreciable change on the aggregate structure during the recording of 0.5 s image sequences at 800 frames per second.

7.6 Determination of Breakup Force

The temperature gradient is defined to be positive if it increases from lower to higher temperatures, i.e. from colder to warmer regions. In this case, as defined by equation 6.7, the net thermophoretic force points from warmer to colder regions. In the used setup frame, this corresponds to upwards vertical direction. Breakup of contacts and ejection of the "probe" aggregates take place sooner or later due to sublimation, depending on the weakest contact with a contact area a_0. For the conditions under which the breakup events are observed, the experiment is stopped once all the ice aggregates generated on the target a have been broken up or ejected by the thermal gradient forces. Some of the recorded aggregates do not show any additional motion before the breakup event occurs. They just move upwards and leave the observable field of view (see figure 7.6 below)

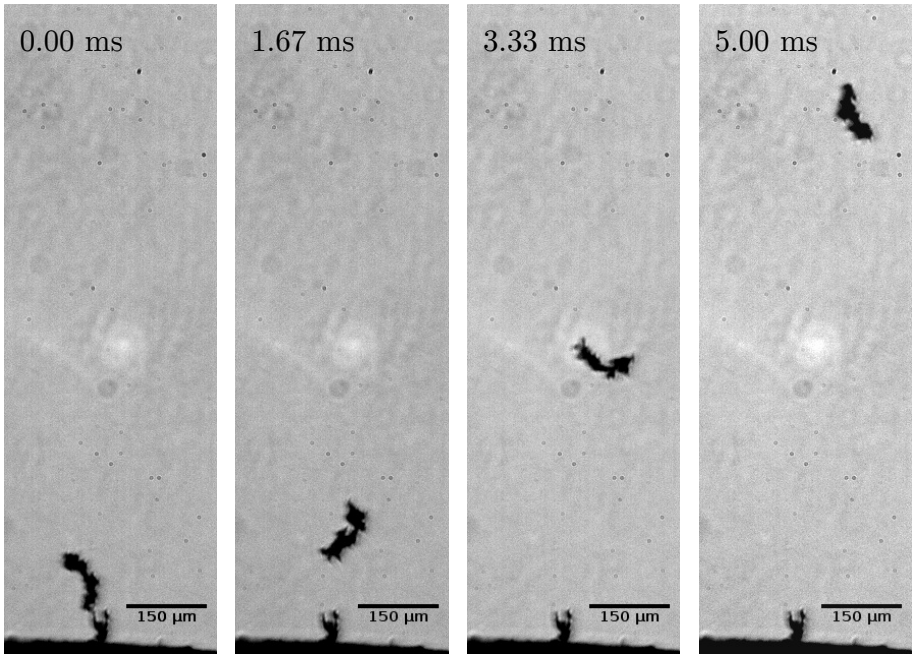

Figure 7.6: From left to right: sequence of a breakup event for a single aggregate. Time in milliseconds.

Many of the aggregates, on the contrary, present additional motions before the breakup. These motions correspond to oscillations on a plane perpendicular to the final breakup pointing direction (see top picture of figure 7.7), twisting motions around the axis along the final breakup direction (see bottom picture of figure 7.7), or occasionally a combination of both of them. The observed time interval between the onset of oscillation (associated to rolling motion between grains at the contact point) or twisting motions and the final breakup of the aggregate, may vary considerably from case to case.

Breakup forces are calculated applying Newton's second law $F = ma$ to the aggregate's displacement after it breaks up. The critical force can be calculated as follows. The static equilibrium conditions, $\sum_i F_i = 0$, just a moment before the breakup it can be written as:

$$F^{\text{push}} = m_{\text{agg}} g + F^{\text{cont}} \tag{7.7}$$

where F^{push} is the pushing force caused by the temperature gradient, and F^{cont} the contact force. Now, using the identity $\sum_i F_i = ma$ just at the moment of the breakup:

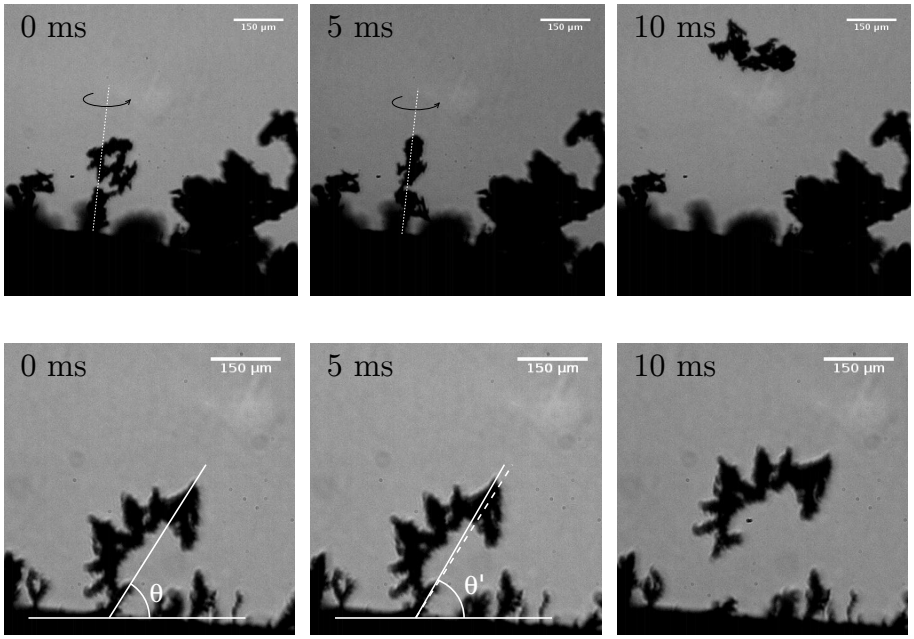

Figure 7.7: From left to right: sequences of twisting (top) and rolling (down) events. In both cases, the breakup of the contact and the following displacement is also shown. Time passing is shown again in milliseconds.

$$F^{\text{push}} - m_{\text{agg}}g = m_{\text{agg}}a \rightarrow F^{\text{push}} = m_{\text{agg}}g + m_{\text{agg}}a \tag{7.8}$$

Considering that the pushing force just before and at the breakup moment is the same, the critical force at the breakup instant $F_{\text{c}}^{\text{cont}}$ can be obtained subtracting equation 7.8 from equation 7.7 giving

$$F_{\text{c}}^{\text{cont}} = m_{\text{agg}}a. \tag{7.9}$$

Accelerations were estimated by measuring the displacement of the aggregate's center of mass (while it was completely visible) on each frame and time interval between frames. The measure of the force is completed once the mass of the aggregate (m_{agg}) is known. The aggregates' mass was calculated by the method described in the following section.

7.6.1 Determination of Aggregate Mass

Many of the aggregates presented twisting motions around their vertical axis. That made possible the imaging of their silhouette from different angles along the line of sight. The 3D reconstruction based on perspective was dismissed because the aggregates presented compact regions which were not possible to resolve from any angle of vision. As alternative, aggregate masses were estimated by a 3D reconstruction as an approximation. This implies the approximation of the face-on projected area A_{agg} of the aggregate multiplied by a thickness x. Then, the total mass of the aggregate can be estimated as:

$$m_{\text{agg}} = \rho_{\text{ice}} A x \tag{7.10}$$

where $\rho_{\text{ice}} = 0.92$ g cm^{-3} is the density of water ice at temperatures under which the breakup events take place ($\sim$ 200 K).

Imaging a complete 360° rotation sequence, two frames were chosen. The first one, with the maximal cross-section A_{agg} (face-on) and the second one, with the minimal cross-section A'_{agg}, which normally coincides with a 90° rotation with respect to the face-on frame. The thickness x is defined as $x = A'/L$, being L the aggregate's length along the twisting axis. An example of this procedure is shown, in figure 7.8. For the non-twisting aggregates, the thickness x was statistically extrapolated from the ratio between the face-on area, A, and the corresponding thickness, x, of each observed aggregate. For both types of mass determination (presenting twisting motion or not), invisible hollow parts of aggregates were not taken into account. That implies that estimated masses are an upper limit of their real value, but it can be corrected if a filling factor $\phi < 1$ is assumed. A filling factor value close to 1 is implausible, because it would imply a solid rigid and it does not fit with the ice generation method used here (where ice grain aggregation, sublimation, sintering and condensation processes takes place). For the same reasons, a very low filling factor is not suitable as well. Since the exact estimation of the filling factor is not possible with the equipment we had, a value of $\phi = 0.4$ is chosen and a factor 2 of associated uncertainty is assumed. Upper and lower values for derivative values are constrained.

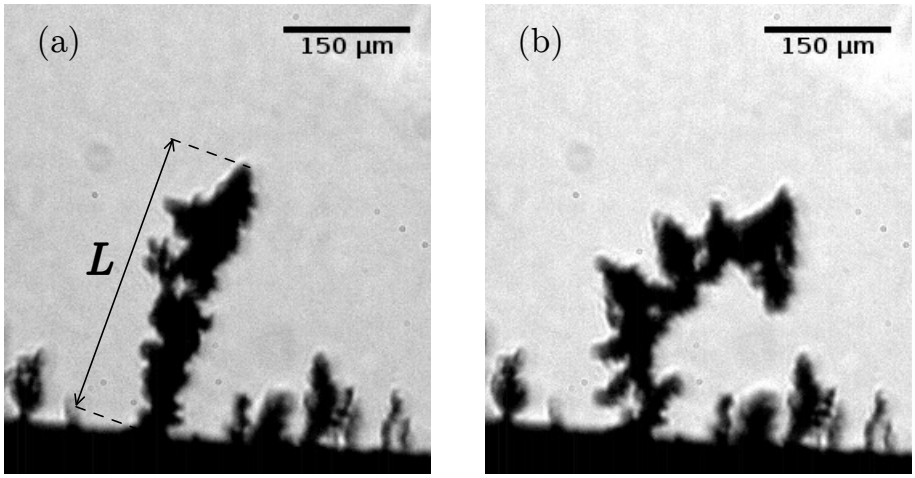

Figure 7.8: Two images from a rotation sequence used for mass determination; (a) 90^o rotated for thickness and length L measurement, (b) largest cross-section.

7.6.2 Ice Aggregates under Thermal Gradient Forces

Since the ice aggregates generated for this experiment are highly porous, it is assumed, at first approximation, that gas can freely flow around ice grains which are considered as constituents. This suggests that the upward pushing force is proportional to the total amount of constituents -considering a monodisperse distribution- or to the aggregate's mass under the same pressure and temperature gradient conditions.

The method used to measure the critical force of the aggregates is described in section 7.1. However, some corrections and considerations have been taken into account for a more accurate result. After the breakup, most of the aggregates do not only present a completely vertical trajectory, but also a horizontal component is observable as well (see figure 7.6). This issue is resolved if in equation 7.8 the component $m_{\text{agg}}g$ is substituted by $m_{\text{agg}}g\cos\psi$, where ψ is the projected angle formed by the acceleration direction of the aggregate's trajectory and the vertical direction (opposed to the gravity acceleration component). It is very important to note that this correction can only be applied to the plane on which the image is focused. With the used equipment it is not possible to establish if there is an acceleration component perpendicular to the focal plane. This issue reduces the measured acceleration to a lower limit of the real one. However, the measured acceleration values are assumed to be close to the real ones because the angles ψ, observed for all the aggregates, didn't exceed 10°, which can be extrapolated to the depth dimension. In addition

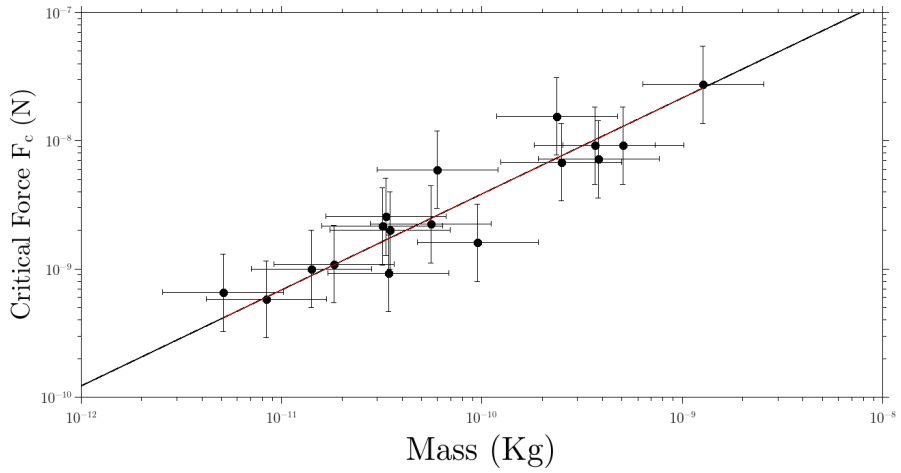

Figure 7.9: Measured critical termophoretic force needed to breakup a contact over aggregate's mass. The line indicates a linear dependence.

to it, aggregates which deviate at least 10° depth from the focal plane should show a non-focused shape when they are situated at the top position of the field of view after the breakup. This was not observed in the experiments presented here. In figure 7.9 it is shown the relation between the associated breakup critical force, F_c, extrapolated from the estimated mass and measured acceleration.

In figure 7.9 it can be noticed that the larger the particle is, the stronger the thermal gradient forces must be in order to breakup the contacts. That implies that larger aggregates provide stronger contact forces. This method is suitable to be applied in the mass range presented here. It wouldn't be suitable for much larger, and hence, heavier bodies to which the thermal gradient force provided by the setup is not enough to lift them.

Once the experimental F_c is established, equation 5.5 and 5.4 can be used to estimate the reduced radius and the contact area at the breaking point. The surface energy γ varies between 0.1 and 0.37 $\mathrm{J\,m^{-2}}$, depending on the literature reference (Dominik and Tielens, 1997; Wada et al., 2007; Gundlach et al., 2011; Kataoka et al., 2013).

Since all derived equations in chapter 5 depend exclusively on the variable R, it is important to calculate its magnitude accurately. The values presented in table 7.1 are mainly enclosed by the factor 2 uncertainty of the aggregate's mass. The theory on which these estimations are based (Johnson et al., 1971; Chokshi et al., 1993) seems to agree with experiments based on μm dust particles (Heim et al., 1999). It must be noticed how the R and a_0 values change depending on which value of γ has.

Table 7.1: Parameters for ice contacts at break-up moment: break-up force F_c, reduced radius R and contact radius a_0, for surface energy $\gamma = 0.1$ and 0.37 J m^{-2}. Uncertainties are estimated to be a factor 2 and result from the mass uncertainty. A filling factor of 0.4 is assumed.

Id	Mass (pg)	F_c (nN)	$R(\gamma = 0.1)$ (nm)	$a_0(\gamma = 0.1)$ (nm)	$R(\gamma = 0.37)$ (nm)	$a_0(\gamma = 0.37)$ (nm)
1	508	9.18	9.74	4.25	2.63	2.74
2	366	9.16	9.72	4.24	2.63	2.74
3	237	15.5	16.4	6.01	4.45	3.89
4	31.8	2.15	2.28	1.61	0.62	1.04
5	34.8	2.00	2.07	1.51	0.56	0.98
6	382	7.16	7.60	3.60	2.05	2.33
7	1272	27.4	29.1	8.81	7.86	5.69
8	60.0	5.93	6.30	3.18	1.70	2.05
9	33.2	2.55	2.71	1.81	0.73	1.17
10	95.2	1.60	1.70	1.33	0.46	0.86
11	34.1	0.93	1.00	0.92	0.25	0.59
12	8.40	0.58	0.62	0.67	0.17	0.44
13	55.6	2.23	2.37	1.66	0.64	1.07
14	248	6.81	7.22	3.48	2.00	2.25
15	14.1	1.00	1.10	1.00	0.30	0.64
16	5.11	0.65	0.69	0.73	0.19	0.47
17	18.3	1.09	1.15	1.01	0.31	0.66

A priori, this variation doesn't seem to have any physical involvement but only a mere value. However, it can be seen that for some cases a_0 is very close to R, and for some other cases (principally when $\gamma = 0.37\,\mathrm{J\,m^{-2}}$), the contact area is even larger than the reduced radius. Considering the model described in figure 5.2, the reduced radius can be expressed as $1/R = 1/R_1 + 1/R_2$. Since the radius of the two particles which form the contact at the breaking point is unknown for all the experiments, it is reasonable to assume that $R_1 = R_2 = R'$. That would imply $R = 2R'$. If the radius of a single particle is lower than the contact area between monomers, the present model wouldn't have any physical sense. This limit is achieved if $a_0 \geq R/2$.

From equation 5.4 and for $E = 0.7\,\mathrm{N\,m^{-2}}$, the limit value is $a_0 \approx 10^{-10}$ m, for $\gamma = 0.1\,\mathrm{J\,m^{-2}}$ and $a_0 \approx 4 \times 10^{-10}$ m for $\gamma = 0.37\,\mathrm{J\,m^{-2}}$. For $\gamma = 0.37\,\mathrm{J\,m^{-2}}$, at least 5 experimental cases (11, 12 15, 16 and 17) correspond to the mentioned critical limit and some other cases are close to it. This is not the case if $\gamma = 0.1\,\mathrm{J\,m^{-2}}$, where no experiment present the $a_0 \geq R/2$ condition. For this reason, $\gamma = 0.1\,\mathrm{J\,m^{-2}}$ is the chosen magnitude to compute derived variables which depend on the surface energy from now on.

Since the agreement between the experimental results and the model used depend on the parameter γ, the validity of the theoretical studies applied to the present work is an open question. As mentioned above, this model agrees with experimental results for μm dust particles, but for aggregates formed by icy particles with a contact area of $\sim 0.2 - 5$ nm, experimental results do not seem to agree with theoretical expectations.

7.7 Rolling

7.7.1 Description and Data Acquisition

Oscillations along the perpendicular direction of the pulling force has been observed in some experiments (see figure 7.7). This effect can be compared to an upside down inverted pendulum. The contact forces between the particles which compound the aggregates are strong enough to consider them as rigid bodies. This reduces the motion to a rotation at the contact point and can be directly related to rolling events along the contact area. The oscillation amplitudes are much smaller than the aggregates' size (between 1° and 10°), but still measurable. The determination

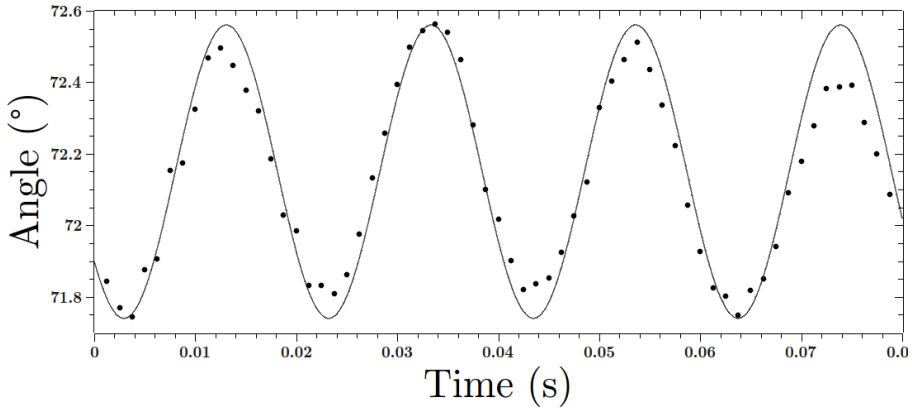

Figure 7.10: Oscillation (rotation at a contact) of an aggregate. The solid line corresponds to a harmonic function fitted to the data.

of the amplitude was determined tracking the movement of the pixel situated at a maximum distance from the contact point. This way the pixel's position uncertainty is minimized. In figure 7.10 the plot of an oscillating event is shown.

Since all oscillating events present a frequency that can be considered constant, the data obtained fits harmonic sinusoidal functions. That implies that in all events the following features are present:

- an exciting torque, probably originated by the physical vibration of the temperature sensor (used as substrate) produced by laboratory environment or probably originated by the thermal gradient forces.
- a restoring torque linear with the displacement.
- a damping torque.

In figure 7.11 they are represented the forces which affect the aggregate and they are potentially the origin of the restoring and damping torques.

The interactions presented in figure 7.11 have the following roles in the general picture of the oscillation motion:

1. Restoring torque
   (a) Pushing thermal gradient force component when the aggregate is displaced from its equilibrium position. This process is analogous to gravity

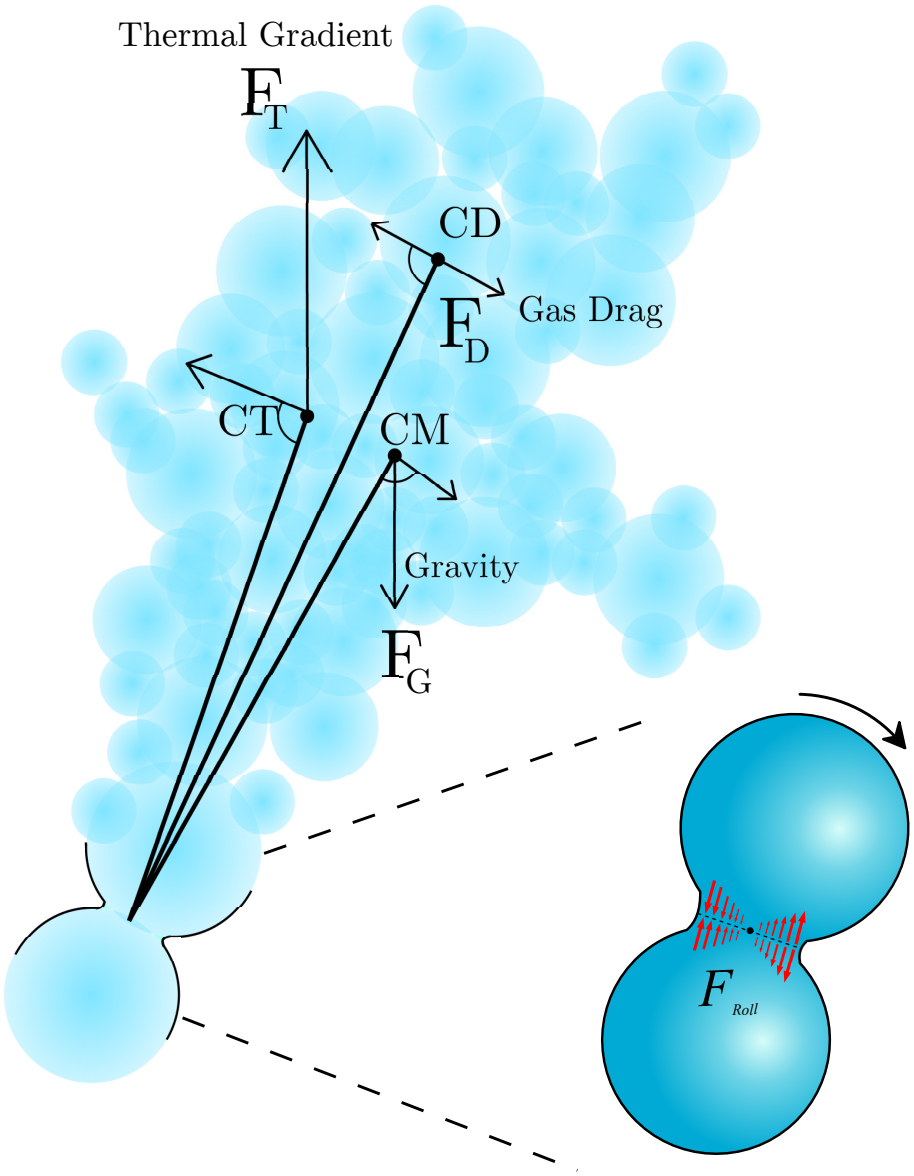

Figure 7.11: Representation of forces and torques involved in a rolling motion. F_{G}, F_{T} and F_{D} are the forces produced by gravity, thermophoresis and gas drag respectively. C_{G}, C_{T} and C_{D} are, in the same order, the points where each force is applied. F_{roll} is the rolling force in this case.

as restoring component for a usual pendulum, but with an inverted force direction.

(b) Elastic bending at the contact area presenting resistance to rolling.

2. Gravitational torque and thermal gradient torque cancel each other in equilibrium position if there is not any resistance at the contact. However, displaced aggregates can present gravitational torques that vary with the inclination.

3. Damping

   (a) Resistance within the contact area when displacements are large enough to overcome the elastic regime.

   (b) Drag or friction with the gas present in the chamber, produced by the aggregate displacement during the oscillation.

Assuming that the damping and the excitational components of the periodic motion are mutually compensated averagely, the experimental restoring torque can be measured from the observed oscillations by using the equation 7.2, where the moment of inertia I_{P} is estimated as

$$I_{\mathrm{P}} = \sum_i m_i r_i^2. \tag{7.11}$$

Here, the the index i refers to each pixel of the imaged aggregate; r_i is the distance of the i^{th} pixel to the contact point and m_i its mass. It is not possible to establish the individual mass m_i for each pixel because the associated thickness at each aggregate point remains unknown. Assuming that all pixels have the same mass and their addition is equal to the total aggregate's mass, a pixel's mass can be written as

$$m_i = \rho_{\mathrm{ice}} A_{\mathrm{pix}} x \phi \tag{7.12}$$

where $A_{\mathrm{pix}} = 3.533 \pm 0.011 \mu\mathrm{m}^2$ is the pixel area; x the thickness defined as in equation 7.10 and the filling factor ϕ is assumed to be 0.4 with an uncertainty factor of 2.

As mentioned above, there are different possible components which contribute to the observed oscillating motion of the aggregates. The contribution of each component is calculated independently and compared to the theoretical values of the rolling torque $M_{\mathrm{r}}(theor)$, which are estimated using equation 5.6 (assuming a value of $\xi = 0.1$ nm as proposed by Dominik and Tielens (1997)). The total experimental rolling torque measured form the images defined in equation 7.2. It is referred here as $M_{\mathrm{r}}(osc)$. The contribution of the thermophoretic force and its torque $M_{\mathrm{r}}(therm)$ can be estimated in an analogous way to the computation of the gravitational torque in an ordinary pendulum. This is carried out using the measured critical force F_{c} for each aggregate which presents oscillations and it assumed to act at their center

of mass. The term a/a_0 in equation 5.6 can take a value between $0.63 - 1$ (see figure 5.3). Here, the torque is calculated when the displacement ξ reaches its critical point, therefore a/a_0 takes its minimum value because it is assumed that the pulling forces are close to their critical value -just before the aggregate breakup.-

The obtained results for the different rolling torques are exposed in table 7.2. The most remarkable aspect of the data comparison is the large value ratio between the experimentally measured torques $M_{\mathrm{r}}(osc)$ and their correspondent theoretical value $M_{\mathrm{r}}(theor)$. Far to be similar, the lowest value between experimental and theoretical ratios is over 3 orders of magnitude and in one case it exceeds the 5 orders of magnitude (aggregate 6). This is a key fact and indicates that the contribution of the contact forces to the total torque is practically negligible. Therefore, gravity and thermal gradient forces are the dominant contributors to the measured restoring torque.

Another phenomenon that reasserts this conclusion is that, in most cases, the sublimation does not observably affect oscillation's amplitude. As the ice particles at the contact point sublimate, their contact area should decrease and consequently the amplitude should increase by rigidity reduction. Even though significant amplitude's growth has not been observed.

7.7.2 Damped Oscillations

In two of the experiments in which rolling events were observed, a decay of amplitude through time was measured. This amplitude reduction can be directly related with the elastic torque produced by the resistance to rolling. Both events were observed after a rearrangement of the aggregates. It was probably produced by the breaking up of some contact close to the last remaining sustaining point, therefore causing the observed damped oscillation of the whole aggregate.

If external forces are not strong enough to produce a permanent excitation, it is possible to extrapolate the damping strength and the contact force by measuring the variability in the oscillations. The damping process is also in this case produced by the contributions mentioned above. A damped oscillation, whose force is proportional to the velocity (like gas drag), reproduces a position profile through time that is different from the one whose damping force remains constant in time (like the elastic force at the contact point). The data of one of the measured damped

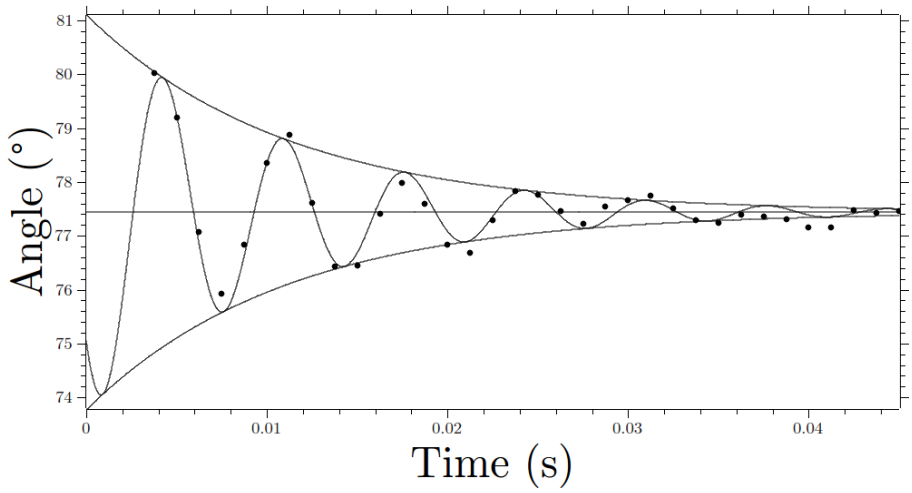

Figure 7.12: Damped oscillation (rotation at a contact) of aggregate 13. The solid line corresponds to an exponentially decaying harmonic function fitted to the data.

oscillation events is shown in figure 7.12.

Let us first assume that the decay of the amplitude is produced by the friction of the aggregate with the gas. The general equation of motion for a physical pendulum may be found in many Classical Mechanics' textbooks. Applying the damping conditions to this particular case and defining the external forces as: F_{G} -the gravity force- and F_{T} -the upwards lifting thermal force-, the equation of motion can be written as

$$I\frac{\mathrm{d}^2\theta}{\mathrm{d}t^2} + \beta\frac{\mathrm{d}\theta}{\mathrm{d}t} + (F_{\mathrm{T}} - F_{\mathrm{G}})l\theta = 0 \tag{7.13}$$

being I the moment of inertia and β, the damping constant. Here, the external forces F_{G} and F_{T} are both assumed to act at the center of mass. Positive directions are considered upwards and clockwise during rotation. Solving the differential equation 7.13, the result may be expressed as

$$\theta(t) = \theta_0 \mathrm{e}^{-\beta t/2I}\cos(\omega_0 t + \varphi) \tag{7.14}$$

where θ_0 is the amplitude of the oscillation; φ, the initial phase and the angular frequency , ω_0, is defined as

$$\omega_0 \equiv \left[(F_{\mathrm{T}} - F_{\mathrm{G}})/I - (\beta/2I)^2\right]^{1/2} \tag{7.15}$$

If we consider a constant restoring force, then equation of motion 7.13 may be rewritten as

$$I\frac{\mathrm{d}^2\theta}{\mathrm{d}t^2} \pm M_\mathrm{r} + (F_\mathrm{T} - F_\mathrm{G})l\theta = 0 \tag{7.16}$$

where M_r is the torque produced by the contact friction or elastic deformation of the contact area. The peculiarity of this case is that the sign of the torque M_r commutes every half oscillation and depends on the aggregate's direction of motion. The only possibility to solve equation 7.16 is to consider a piecewise function (Zonetti et al., 1999; Marchewka et al., 2004):

$$\theta(t) = \theta^{max}\cos(\omega_0 t + \varphi) + C \tag{7.17}$$

where here ω_0 and C are respectively defined as

$$\omega_0 = \left[(F_\mathrm{T} - F_\mathrm{G})l/I\right]^{1/2} \tag{7.18}$$

$$C = M_\mathrm{r}/I\omega_0^2 \tag{7.19}$$

The angular amplitude θ_0^{max} does not remain constant, and in each oscillation its value is reduced to a fixed amount. The constant decay of θ_0^{max} can be expressed as

$$\theta_n^{max} = \theta_0^{max} - 2nC. \tag{7.20}$$

The maximum elongation takes place at $n = 0$. It corresponds to the starting point of the oscillation. Once periodic motion starts, the aggregate keeps moving until the restoring force makes stops it. The conditions of continuity establish that at this point ($n = 1$) the oscillation goes in the opposite direction from an initial position whose amplitude is a factor $2C$ lower than at the starting point. This periodic process goes on until the aggregate remains motionless. Taking into account the continuity conditions already mentioned and the condition from equation 7.20, the equation 7.17 can be rewritten as (Marchewka et al., 2004)

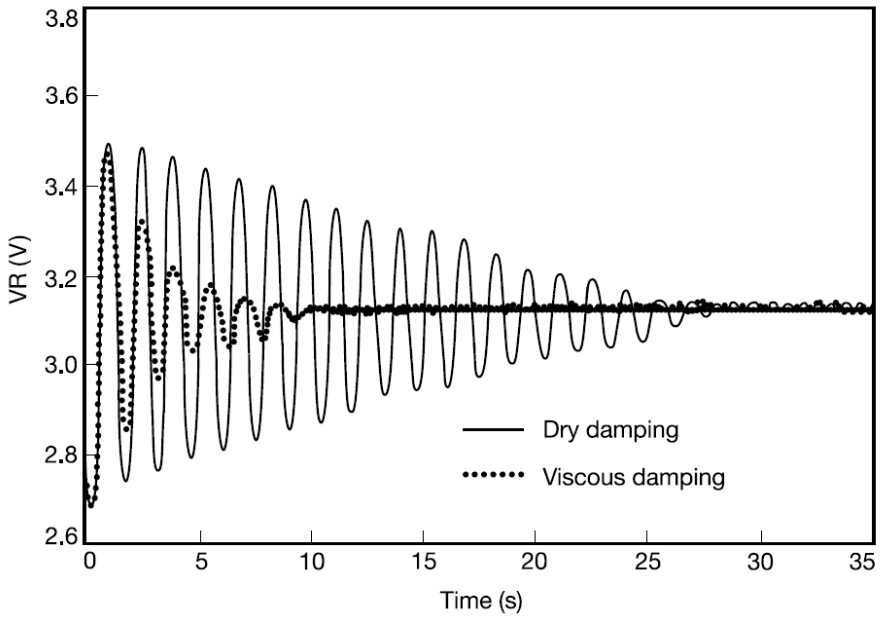

Figure 7.13: Comparison between dry damped (solid line) and viscous damped (dots) oscillations (Zonetti et al., 1999). Both damped oscillations were generated by a pendulum in two different environments: air for the dry one and water for the viscous one. The voltage on the horizontal axis is directly related to the position of a pendulum.

$$\theta(t) = (\theta_0 - 2nC)\cos(\omega_0 t) + (-1)^n C \tag{7.21}$$

The main difference between the previous case where the damping was caused by the air friction and this one, is that the amplitude decay has a linear profile in spite of an exponential one. An example of both decays is shown in figure 7.13. This plot is obtained from the study of a pendulum's motion carried out by Zonetti et al. (1999), in which the damping force is a dry constant friction force.

From figure 7.12, corresponding to the decay profile of the present experiment, it can be seen that a linear amplitude decrease is not significantly consistent, but follows an exponential profile. This indicates that the damping process from the observed oscillations is basically driven by gas drag and not by friction at the contact point. However, with the experimental data obtained, it is possible to establish an upper limit of M_{r}. Introducing the data corresponding to figure 7.12 (aggregate 13) into equation 7.20 and substituting it in equation 7.19 a value of 5.72×10^{-16} N m is obtained. This calculation can be similarly applied to the only supplementary damped case (aggregate 2). Both values are shown in Table 7.2 as $M_{\mathrm{r}}(damp)$ together with

the rest of torque contributions.

Table 7.2: Rolling torques as calculated by the model for the given contact $M_{\mathrm{r}}(theor)$ for $\xi = 0.1$ nm and $\gamma = 0.1$ J m^{-2}, as measured by the excited oscillations $M_{\mathrm{r}}(osc)$, as determined from damped oscillations $M_{\mathrm{r}}(damp)$, as estimated by the critical force F_{c} times the projected distance between the centre of mass and the contact point at maximum elongation, and the ratios between different torques. All torques shown in the table are in N m.

Id	$M_{\mathrm{r}}(theor)$	$M_{\mathrm{r}}(osc)$	$M_{\mathrm{r}}(damp)$	$M_{\mathrm{r}}(therm)$	$\frac{M_{\mathrm{r}}(osc)}{M_{\mathrm{r}}(theor)}$	$\frac{M_{\mathrm{r}}(damp)}{M_{\mathrm{r}}(theor)}$	$\frac{M_{\mathrm{r}}(therm)}{M_{\mathrm{r}}(osc)}$
1	1.84E-18	1.55E-14	-	1.34E-14	8420	-	0.86
2	1.83E-18	1.96E-14	4.31E-15	6.46E-14	10700	2350	3.29
6	1.43E-19	2.20E-13	-	-	154000	-	-
7	5.48E-18	3.37E-14	-	4.70E-13	6150	-	13.95
13	4.47E-19	2.51E-15	5.72E-16	4.92E-15	5610	1280	1.96
14	1.36E-18	2.09E-15	-	6.93E-15	1530	-	5.09

The rolling torques values extrapolated from damped oscillations are closer to the theoretical estimations, but they are still a factor 1280 higher (in the best of the cases). It must be noticed that only two cases of damped oscillations were able to be analysed and it is difficult to draw a final conclusion about the model's validity without more examples. The obtained results show that oscillations are gas-drag dominated. It is the main reason of not spending more time on the data acquisition related to damped oscillations. Nonetheless, the obtained values are still valid to assign them as upper limits of rolling torques of nanometre ice contacts.

For the theoretical estimation of M_{r}, a critical displacement, $\xi_{\mathrm{crit}} = 0.1$ nm, was assumed (Dominik and Tielens, 1997). However, Heim et al. (1999) measured experimentally the same parameter and obtained a value of $\xi_{\mathrm{crit}} = 3.2$ nm. Despite the significant difference, Heim et al. (1999) explain that this result is not unrealistic, since the measured ξ are still much below the reduced radius R values (0.475 µm in that case). If the latter $\xi_{\mathrm{crit}} = 3.2$ nm value is assumed, then the ratio between theoretical and experimental values is dramatically reduced (see Table 7.3). The ratio $M_{\mathrm{r}}(damp)/M_{\mathrm{r}}(theor)$ reduction between the damped cases and their corresponding theoretical values is even more significant (73 and 40 for the aggregates 2 and 13, respectively). This indicates how critical is the choice of ξ_{crit} and how it affects the final result on M_{r} calculation. In any case, this does not change the fact that the oscillations are basically dominated by gas drag and the validity of the experimental results here presented confirm being absolutely coherent as upper limits.

Table 7.3: Rolling torques as calculated by the model for the given contact $M_{\mathrm{r}}(theor)$ for $\xi = 3.2$ nm and $\gamma = 0.1$ J m^{-2}, as measured by the excited oscillations $M_{\mathrm{r}}(osc)$, and the corresponding ratios.

Aggregate	$M_{\mathrm{r}}(theor)$ N m	$M_{\mathrm{r}}(osc)$ N m	$\frac{M_{\mathrm{r}}(osc)}{M_{\mathrm{r}}(theor)}$
1	5.87E-17	1.55E-14	264
2	5.86E-17	1.96E-14	334
6	4.58E-17	2.20E-13	4800
7	1.75E-16	3.37E-14	193
13	1.43E-17	2.51E-15	176
14	4.36E-17	2.09E-15	48

7.8 Twisting

7.8.1 Description and Data Acquisition

Some of the observed aggregates presented a twisting motion around the breakup direction axis before they become lifted by the thermal gradient forces (see figure 7.7). This phenomenon is similar to the rotations observed in van Eymeren and Wurm (2012), where ice aggregates of 100 μm in size twist under the gas-grain coupling induced by thermal gradient forces (see section 7.8.2) and by the effect of aggregates asymmetry.

Most of the observed cases were aggregates that twisted at apparently constant frequency until they broke up. In these cases, the beginning of the twisting motion was not recorded because the equipment employed had a recording time limitation. Since the most important variable to be measured is the critical force F_{c} (because all the other variables are derived from it) the image recording stopped once the breakup took place. In most the cases, the onset of the twisting motion was not observable during this time interval, but in some cases it was possible to observe and measure the initial angular acceleration. This allows the direct estimation of the twisting torque M_{t} for these aggregates.

Equations 7.2 and 7.11 are used to calculate the twisting torque. In this case, the angular acceleration α_{P} is measured around the rotation axis. This axis coincides with the direction to which the aggregate is lifted after the breakup and points almost vertically upwards. It must be noticed that for twisting motion, r_i corresponds to the distance between the i^{th} pixel and the rotation axis. The angular motion of

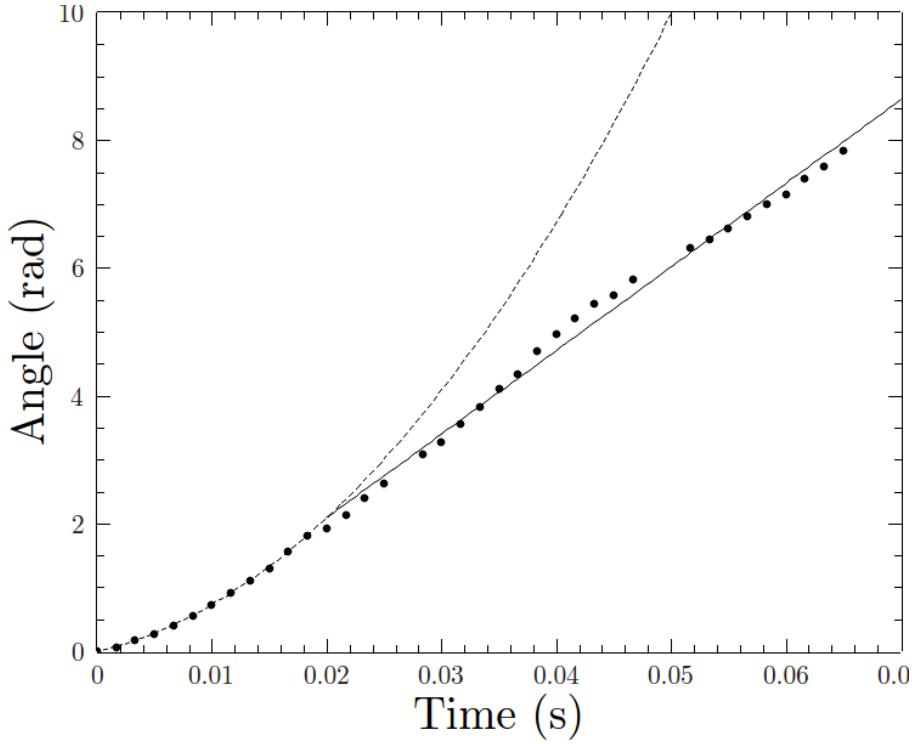

Figure 7.14: Angle of a selected aggregate pixel around the rotation axis. The obtained data is represented by black dots. The solid line represents a linear fit to the data, showing a constant angular velocity to start from a time after the twisting onset. The dashed line is a quadratic fit to the data, showing an angular acceleration at the twisting onset.

the aggregates is extracted from 2D projections corresponding to the silhouette ice produces against the background light. Tracing the motion of one pixel, its angular position can be measured by $\theta = \arcsin(x'/x)$, being x the maximum distance of the chosen pixel and the rotation axis (amplitude) and x' the actual distance between the same pixel and the same axis at any moment. If the data obtained by the pixel track is plotted through time, a curve like the one shown in figure 7.14 is obtained.

To calculate the angular acceleration it is assumed that the motion of the chosen pixel (and the whole aggregate too) describes a uniform accelerated rotation. After a certain time interval, the motion leaves the accelerated regime to turn into an almost constant rotation frequency regime that remains unaltered until the aggregate breaks up. The first stage of the curves obtained by the pixel tracking fits a parabolic function (corresponding to an angular acceleration). In the case of the figure 7.14 -which corresponds to aggregate 3- it leads to an acceleration of $\alpha = 6300 \pm 200\ \mathrm{rad\,s^{-2}}$. It must be pointed out that twisting aggregates presented angular accelerations mostly by between 6000 - 10000 $\mathrm{rad\,s^{-2}}$. There are a few cases

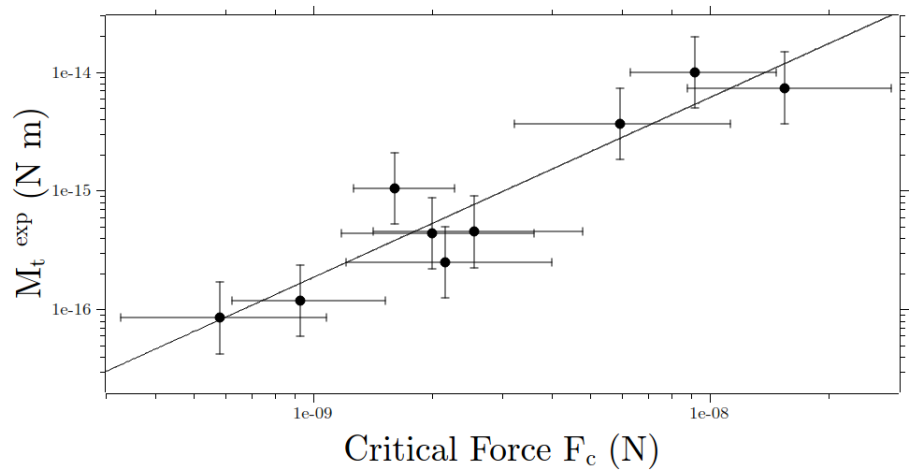

Figure 7.15: Twisting torque over break-up force. The solid line corresponds to a linear dependence fitted to the data.

where this acceleration reached 40000 rad s^{-2}. It is assumed that for a given position in the temperature gradient region, the experimented force remains constant. However, depending on the mass distribution and the structure of the aggregate on which these forces are acting, the net torque and the resulting angular acceleration that the aggregates experiment can be significantly different, as the data shows.

Since the measure of the torque, once the aggregates start to twist, is a finite value, the friction in the contact point is assumed to be suddenly reduced. It may be compared to the macroscopic friction scenario where friction in a moving object on a surface is lower than the sticking friction (if the same object still remains static). If that were not the case, the rotation would take place very slowly. It is expected that twisting torques should increase for larger contact areas (i.e. for stronger breakup critical force F_c). It basically agrees with the twisting torques measured experimentally and they can be seen in the plot in figure 7.15.

The twisting torque M_t can also be estimated by equation 5.13. For all calculations, $\gamma = 0.1$ J m^{-2}, and the following parameters from Dominik and Tielens (1997) are considered: $E = 7 \times 10^9$ N m^{-2}; $G = 2.8 \times 10^9$ N m^{-2}; $b = 3.36$ Å and $\sigma = 3.36$ Å. Values from variables F_c and a_0 correspond to the ones estimated in the experiments in section 7.6. The obtained results are are shown in Table 7.4.

A very important aspect to take into account is that the area at the the contact point is affected by sublimation during the time interval between the twisting motion onset and the breakup of the aggregate. As it has been pointed out in section 7.5,

this time interval is long enough to change the radius of the contact a. Applying equation 7.6 to the estimation of the reduced radius R at the moment of the twisting starting instant, a corrected value of the twisting torque $M_{\mathrm{t}}^{corr}(theor)$ is obtained. The results are also shown in table 7.4.

Table 7.4: Twisting Torques; as measured; as predicted by the theory at the breakup moment and as calculated at the twisting onset. The last two columns show the ratio between the experimental measured torque and its theoretical value (non-corrected and corrected by sublimation respectively). All torques are in N m.

Id	$M_{\mathrm{t}}(exp)$	$M_{\mathrm{t}}(theor)$	$M_{\mathrm{t}}^{corr}(theor)$	$\frac{M_{\mathrm{t}}(exp)}{M_{\mathrm{t}}(theor)}$	$\frac{M_{\mathrm{t}}(exp)}{M_{\mathrm{t}}^{corr}(theory)}$
2	3.97E-015	2.25E-17	2.80E-16	176.4	14.2
3	2.95E-015	6.69E-17	8.91E-16	44.1	3.31
4	9.94E-017	1.07E-18	1.14E-15	92.9	0.09
5	1.75E-016	8.61E-19	6.49E-16	203.2	0.27
8	1.47E-015	9.10E-18	4.45E-16	161.5	3.30
9	1.81E-016	1.53E-18	4.73E-16	118.3	0.38
10	4.20E-016	5.66E-19	1.13E-15	742.0	0.37
11	4.71E-017	1.69E-19	6.20E-16	278.0	0.08
12	3.39E-017	5.91E-20	9.17E-16	573.8	0.04

As it can be seen, the correction factor in some cases are close to 10^3 (or even 10^4 for aggregate 12). Since the sublimation's correction is applied identically to all aggregates, how it affects to the new calculation of the twisting torque depends on the size of the reduced radius at the moment of the breakup (the smaller the reduced radius, the larger the correction) and the time that the aggregates keeps twisting after the onset (the longer the time, the larger the correction). From the data obtained, it seems that the aggregates which suffer a larger correction are those with a smaller critical breakup force, which corresponds to smaller reduced radius. A comparison of the ratio between the experimental twisting torque and the one estimated theoretically is shown in figure 7.16 -for corrected (black dots) and not corrected cases (red squares).-

7.8.2 Gas-Grain Coupling

The aggregates are generated via hit and stick events, resulting in cluster-cluster aggregates. The same process is assumed to occur during the first stage of planetesimal formation. The way how these type aggregates couple to the gas is then of

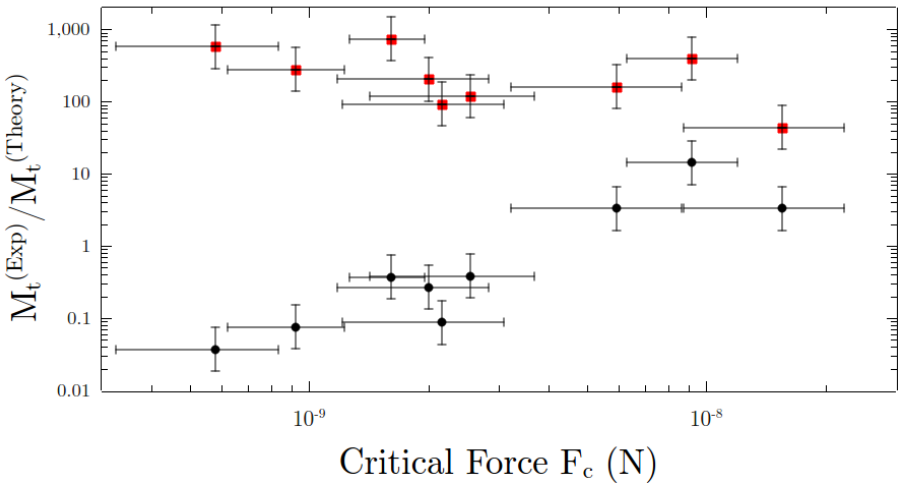

Figure 7.16: Comparison between experimental twisting torque and theoretical twisting torque $\gamma = 0.10$ J m^{-2}. Red squares: uncorrected ratios; Black circles: twisting corrected ratios for sublimation to the time twisting sets in.

sever importance. Torques induced by radiation or gas drag may cause the rotation of solid bodies with a constant velocity. The rotation might be related to alignment, and in case of collision, it could provide an important part of the resulting energy. The clue here is that rotation frequency is basically set by gas drag and there are a lack of experimental measures for this. The processes described here are directly related to the interaction of gas and μm ice grains. A possible way to provide valuable information of particle motion and collisions in PPDs, is the systematic study of cluster-cluster aggregates interactions with the gas.

For microscopic particles, the rotation of aggregates and its relation with gas drag is not easy to measure. van Eymeren and Wurm (2012) observed rotation frequencies of 1-100 Hz for 10-100 μm sized ice aggregates during their free levitation. Frequencies measured here for twisting are similar to these results. Thus, the present setup offers the possibility to study the relation between the gas and its repercussion on rotating aggregates. It especially allows to determine coupling times. Figure 7.17 shows how the twisting frequency is related to the inertia moment.

The frequency at equilibrium is $\omega = \alpha\tau_{\rm rot}$, being $\alpha = 10^4$ rad s^{-2} the angular acceleration and $\tau_{\rm rot}$ the coupling time. At a pressure of 0.5 mbar, $\tau_{\rm rot} = 0.04$ s. Let us compare this result to the linear coupling time for spherical particles of the aggregate masses at the same pressure. This can be expressed as (Blum et al., 1996):

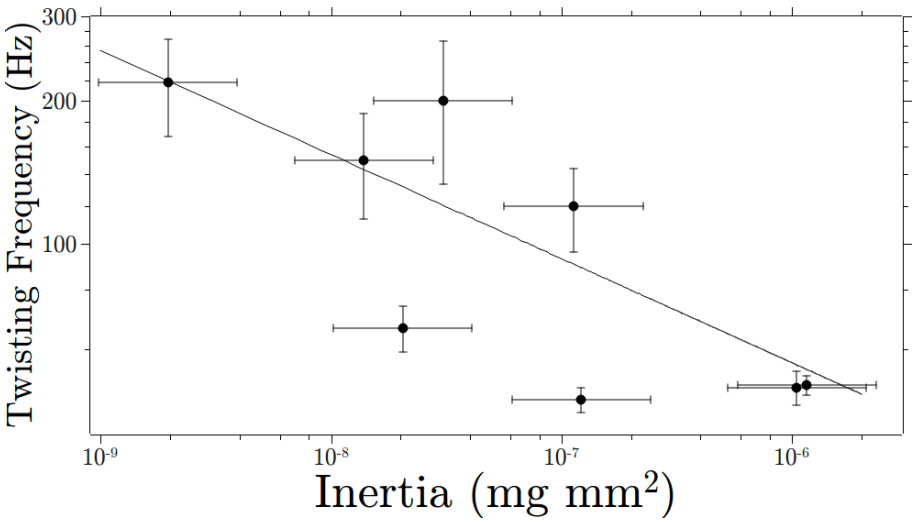

Figure 7.17: Measured twisting frequency over their moment of inertia.

$$\tau_f = \varepsilon \frac{m}{\sigma_\mathrm{a}} \frac{1}{\rho_\mathrm{g} v_\mathrm{m}} \tag{7.22}$$

where $\varepsilon = 0.68$ is a constant; m the aggregate's mass; σ_a is the cross-section; ρ_g the gas density and v_m the mean thermal velocity of the gas molecules. If the corresponding experimental parameters are introduced, then the linear coupling time is $\tau_f \sim 0.10$ s. This value is of the same order; then, the setup allows the possibility to calculate these properties. However, this topic is beyond the scope of the present work.

7.8.3 Discussion

After the observation of the twisting events and the comparison of some physic variables between their experimental values and their theoretical counterparts, some aspects remain open and need to be discussed.

- It is remarkable the fact that twisting aggregates show a continuous spinning motion while the contact still holds the whole structure, despite the application of a pulling thermal force. This effect is not expected to be observed on macroscopic scenarios, where the break of a contact by sliding or twisting would produce the immediate lift under the thermal force. As Dominik and Tielens (1997) suggested, it would imply that at the contact point of the

aggregates studied here, the friction induced by twisting is certainly provided by a stepwise motion of atoms from potential wells that are successively broken and formed during the sliding/rotation. Therefore, during the inelastic regime of twisting motion, only part of the sticking properties will be lost, at least for time intervals short enough not to be significantly affected by sublimation.

- Regarding the free spinning motion mentioned above, another possible explanation lies on the fact that the particles at the contact point were fluid. Johnston and Molinero (2012) showed through molecular dynamics computer simulations that at 200 K, water ice droplets smaller than 1.4 nm could turn into liquid. This is the size of the reduced radius obtained in some experiments (see Table 7.1). The amount of experiments depends on the value of the surface energy γ considered. *A priori*, it seems a good argument to explain the spinning of the aggregates with the smallest contact radius. But the reduced radius is much larger at the moment of the twisting onset and therefore it would not be liquid. Additionally, rotating aggregates with larger contact radius are not under the melting threshold and they are considered as completely solid here.

- While non-corrected experimental values seem to be a factor between 50 and 800 higher than the theory, the same ratio shows much lower results when the correction by sublimation is considered. In some cases, specifically those which the F_c lower than 3×10^{-9} N, the theoretical value of the torque exceeds the experimental measure while they keep this value lower for larger values of F_c. Since the same correction method based on a simple sublimation model has been applied for every case, the aggregates with smaller F_c are much more sensitive. The main conclusion from the data obtained after correction is that for water ice aggregates corresponding breakup forces $F_c > 3 \times 10^{-9}$ N, the experimental twisting torque would be a factor ~ 10 higher than the theoretical one.

- The model considered for the contact physics is based on spherical particles, but real contact areas may be formed by irregularly shaped monomers (Mo and Szlufarska, 2010). As the aggregate spins, the contact area may change in form and size. That may cause deviations in the measure of parameters related to the angular motion like the twisting torque. It may explain the periodicity with which the plotted data deviate from the fitted line corresponding to a

constant angular velocity observed in figure 7.14. In some experiments it has been observed that the spinning motion stops completely. This could be explained by the influence of gravity over non-symmetrical bodies, but another possibility could be the existence of more than one contact point, separated by very short distances, providing a much larger torque. If this were the case, when one of the contacts breaks and the other/s contact/s are not strong enough to counter the thermal gradient torque, the aggregate would start spinning with a determined angular acceleration.

- Another process that may also influence the twisting motion (and other related particle contact properties) is the sintering of water ice. This would affect the motion providing a higher torque and it would explain the jumping to the definite acceleration observed after the elastic regime is exceeded. However, they have been observed some aggregates which started twisting after being readjusted by rolling due to thermal pulling forces along the lift-off direction. In these cases, contacts would not be affected by sintering so far.

Assuming that at least one of the above considerations were valid, the measured twisting torques would be upper limits, as in the rolling motion case. However, the periodical variation of spinning velocity observed in some aggregates, as shown in figure 7.14, would remain without explanation. The previous breakup of an existing extra contact or produced by sintering, cannot explain this phenomena, implying that the measured torques are directly related by a single contact.

In some experiments, the estimated contact area is lower than 1 nm. Depending on the chosen value of γ, the contact area calculated for some cases would be even ~ 0.5 nm (see Table 7.1). Taking into account that the diameter of water molecules is 0.29 nm, only a few molecules would hold the whole aggregate (20 μm) under the pulling force. In this hypothetical case, quantum effects at the contact point would not be meaningless. Although the uncertainty of the measured critical force F_c is assumed to be a factor 2, the size contact area at the breakup instant would still be at scales in which quantum effects would be considered.

According to my personal research, there isn't any other theory at hand to compare the experimental data here presented. Since it is not possible to resolve the size of the contact are directly, it must be extrapolated by an analytic equation with the uncertainty of knowing the validity of its application. However, using the model described in chapter 5, the analytic expressions reported to calculate the forces are

self-consistent if a potential correction factor and an uncertainty of factor 2 in most of derived physical variables which were considered. A model of molecular dynamics containing all the possible aspects that should be taken in to account at such small scale would be ideal but not yet available, even though some recent works are making some progress in this topic (e.g. Tanaka et al., 2012).

7.9 Conclusions

As it was mentioned at the beginning of this chapter, much work on the study of planetesimal formation has been done during the last years. Theoretical models represent the larger part of the research, but experimental studies are being added to fully understand the very first stages of planet formation. Throughout this chapter I have provided new experimental results on processes in which contact forces are relevant, specifically breakup, rolling, sliding and twisting of water ice aggregates at nm scale. These processes, as well as material properties like composition and porosity, determine the outcome of aggregate collisions, which are believed to be the main growth mechanisms during the first formation stage. Experimental measurements of breakup and rolling exist for silicate grains which are μm in size (Ding et al., 2007; Heim et al., 1999), furthermore, some results have been obtained at nm-scale pulling and in adhesion (Moore and Houston, 2010). At μm sizes, the model explained in chapter 5 fits with the experimental results, but sliding and twisting measurements based on this theory are rare.

Interstellar grains are believed to be formed by nm-sized particles (Mathis, 1986; Dwek et al., 2004). In addition, no experimental results are reported for contact physics of water ice. With the development of the technique and experimental procedure, here presented, together with the results obtained, the achieved objectives are:

- The determination of forces between nm-size particles and the observation of twisting processes.
- The study of induced thermal gradient forces on aggregates.
- The study of rotational gas-grain coupling.

- The calculation of breakup forces and its relation with rolling and twisting torques.
- Upper limits of torques produced by nm-ice particles by rolling resistance.
  - Experimental results are a factor 50-4000 larger than the models developed by Dominik and Tielens (1997), depending on the value of the energy surface γ chosen. Since these results are considered upper limits, they are still consistent with the model, but real torques with factor 50-4000 larger than the ones predicted by the theory cannot be excluded.
- Measured torques opposing to twisting are a factor $\sim$ 10 than theoretical expectations.
  - In this case, the data would be in good agreement with the model, but unexpectedly for critical forces $F_c \lesssim 3 \times 10^{-9}$ N. Sublimation corrections causes experimental torques to lie below the estimated theoretical predictions. However, lacking of an alternative model, the validity of the measurement rely on the existent theory.

7.9.1 Astrophysical Aspects

Interstellar clouds and protoplanetary discs are the main scenario where the present work can be applied. Principally on planet forming regions around stars, coagulation of aggregates is a fundamental mechanism from which breakup, rolling, sliding and twisting are major processes. Since water ice seems to put up more resistance to twist (and probably to roll), it implies that icy aggregates would be less likely to restructuring. This would be in agreement with the simulations of Kataoka et al. (2013) and they would tend to form fluffy icy aggregates up to meter sizes. Furthermore, this fact should be taken into account for the modelling of larger particles' evolution discussed for coreshine (e.g. Steinacker et al., 2010; Pagani et al., 2010). In addition, the modelling of some experimental results of aggregate compression needs to assume a more rigid contact between particles by sliding in order to fit theory and laboratory observations (Seizinger et al., 2012). Since sliding and twisting are formulated from the same type of interaction, the modifications introduced by Seizinger et al. (2012) would support the results presented above.

Generally, the growth of dusty and icy aggregates would yield on bodies of different porosity depending on the size. With the present results, it might be interpreted just as speculation, but transitions in planetesimal formation that separates coagulation from bouncing (or even rupture of aggregates) could be shifted to larger sizes. This is possible if smaller particles and/or ice are considered (Teiser and Wurm, 2009b; Windmark et al., 2012; Kelling et al., 2014). It would cause the growth of bodies with sizes large enough to concentrate in turbulent discs and to be captured by posterior gravitational collapse (Chiang and Youdin, 2010). This way, the results might slightly shift the picture of planetesimal formation.

The gas-flow through and around aggregates can be produced by thermal creep. In a dry environment, the gas-flow may cause the inner and outer erosion of icy bodies (if sublimation is present). Contact forces apart, using a similar setup, it may be observed how large and highly porous ice aggregates would evolve in a gas-flow.

7.9.2 Future Work

The study of the contact forces exposed here has been carried out with the use of thermophoretic forces. The combination of thermophoresis with low sublimation rates of ice is ideal to measure contact interactions. It is possible to apply this method to other materials like metallic nm-particles. However, since sublimation conditions for such materials are difficult to achieve in the laboratory, the thermophoretic force should be manipulated. Changes in temperature and pressure in order to modify the thermal gradient can be a good way to start. In fact, how these variations affect the results hasn't been deeply studied yet and it could be a possible way to reduce the gas damping in oscillations. Temperature control is fundamental, a faster control would be optimal to prevent rotating aggregates from continuous sublimation and breakup for longer time interval observations. Since sublimation rate is one of the uncertainties' origin for correction of twisting torques, it would be convenient to study it controlling different parameters in more detail.

It is desirable to discern until what extent the contact dynamics from external forces influence the aggregate motions. A possible way to achieve this is to excite the substrate at the aggregate resonance frequency. This should cause an increase of the oscillation's amplitude and it would make the rolling torque measurable even when thermophoretic forces are present. Some tests have been carried out, but the results

obtained are not concluding yet. Analysis of mass and motion of the ice aggregates can be improved by generating ice aggregates with a well defined structure (like fractal aggregates) and observing them with a better time and spatial resolution. Aggregates' observations from different angles would improve the imaging of its 3D structure.

Although electrical charging effects are considered too weak to affect the measures here exposed, the influence of charged particles should not be completely discarded. Future experiments are expected to expose the probe under electrical and/or magnetic fields. Additionally, a speculative perspective is the construction of well-defined microprobes which could be attached to the ice aggregates and could be subjected to the electric or magnetic fields generated.

The principal aim to achieve after the present studies is to quantify the contact dynamics of water ice particles with higher accuracy. The application of similar techniques in other materials -in order to measure the same parameters (breakup force, rolling and twisting torques)- would be the next stages to understand how contact forces determine the growth of planetesimals.

Chapter 8

Summary and conclusions

This work is focused on the understanding of how water ice may affect the growth of planetesimals in a protoplanetary disc. The data presented here, obtained by laboratory experiments, it is a contribution to the existing models. Through induced temperature gradients in a low pressure environment (0.1-1 mbar) created in a vacuum chamber, processes like levitation, sublimation, fragmentation and aggregation of water ice aggregates were observed. In this chapter I summarize how the obtained data is related to the planetesimal formation and why it is relevant.

8.1 Sublimation close to the Snowline

In protoplanetary discs, if solid bodies are large enough to decouple from gas, they drift inwards (Weidenschilling, 1977), achieving a maximum velocity where they are ($\sim$ 1 m) large. Saito and Sirono (2011) proposed a model where dust particles ($\sim$ 1 μm) are embedded in icy mantles forming larger aggregates ($\sim$ 1 m). When such aggregates cross the snowline, sublimation would cause the fragmentation into smaller bodies and the release of the dust cores. It causes the concentration of these solids close to the snowline because smaller bodies drift inwards slower. Therefore, the planetesimal formation would be enhanced.

The fragmentation of water ice due to sublimation has been observed in the laboratory. The study of 20 ensembles of levitating ice aggregates show that the number N, of resulting icy grains, depends only on the initial aggregate radius, r. Specifically, an ice aggregate formed via cluster-cluster aggregation would fragment into

$N = \chi r^2$ pieces, with $\chi = 2\,\mathrm{mm}^{-2}$. Further details are expected to be investigated in the future. However, the main idea that sublimation close to the snowline may enhance the probability of planetesimal formation, is definitely supported by the experimental results presented in this work (see chapter 6).

8.2 Coagulation of Ice Aggregates

During the sublimating process of the ice ensembles, many $\lesssim 1$ mm fragment collisions have been observed. Impact speeds up to 2 $\mathrm{cm\,s^{-1}}$ have been measured. **100%** of the impacts result in aggregation. This is expectable since, according to the results obtained by Shimaki and Arakawa (2012), adhesion has been observed for much larger spherical ice aggregates ($r = 1.5$ cm) with a much higher filling factor ($\phi = 0.3$) at velocities of 4 $\mathrm{m\,s^{-1}}$. The collisional outcome from Heißelmann et al. (2010) show no evidence of coagulation for similar sized ice spheres. However, in this case, the colliding icy bodies hat a filling factor $\phi = 1$.

In protoplanetary discs, relative velocities between mm compact particles are expected to be ~ 1 $\mathrm{m\,s^{-1}}$. This value is reduced if fluffy aggregates are considered, because they are stronger coupled to the gas. Then, the formation of the first planetesimals close to, but beyond the snowline should be very fast. In particular, Ros and Johansen (2013) estimate that decimetre-sized pebbles could be formed from millimetre-sized grains via condensation close to the snowline in about 1000 years. It is very important to remark, that aggregation is not taken into account. Adding the coagulation process to this model, planetesimal growth close to the snowline would be even faster.

8.3 Contact Forces between Icy Grains

The outcome of a two-body collision depends strongly on the force between their constituents. A solid aggregate can be taken as an ensemble of individual grains attached by molecular forces. These forces take place at the contact regions between the grains. Some models for micrometre-sized spherical grains have been developed to understand the contact physics (e.g. Johnson et al., 1971; Dominik and Tielens, 1997; Wada et al., 2007). Considering two grains in contact, four different degrees of

freedom are possible: 1.Compression/Adhesion, 2.Rolling, 3.Sliding and 4.Twisting.

Excluding face-on collision experiments, there is a lack of laboratory studies for water ice in this topic (Gundlach et al., 2011). In order to investigate the contact physics between water ice grains, a Thermal Gradient Force Microscope was developed. According to the model from Dominik and Tielens (1997), I describe below the main conclusions obtained.

Compression/Adhesion

The measured acceleration of ice aggregates after their breakup permits the estimation of the critical force F_c between the grains. Depending on the surface energy γ chosen, some of the obtained results seem to be in disagreement with the theory. In particular, if $\gamma = 0.37\,\mathrm{J\,m^{-2}}$, 5 experimental results show that the half of the reduced radius R is smaller than the contact radius a_0 (see table 7.1), which wouldn't have any physical sense. This issue is partially solved if $\gamma = 0.1\,\mathrm{J\,m^{-2}}$ is assumed.

The agreement between the experimental results and the model used depend strongly on the parameter γ, therefore, the validity of the theoretical studies applied to the present work is an open question. As mentioned above, this model is in a satisfactory agreement with experimental results for μm dust particles, but for aggregates formed by attached icy particles by a contact area of $\sim 0.2 - 5$ nm, experimental results do not seem to show much agreement with theoretical expectations.

Rolling

Some aggregates presented oscillating motions before their contact breakup. This movement can be described as an inverted pendulum upside down. Measuring the oscillation's angular acceleration and its moment of inertia, the torque applied at the contact point can be estimated. The experimental results are compared with the theoretical values predicted by the model developed by Dominik and Tielens (1997). The first results show that some experimental torque calculations are a factor 10^4 higher than described by the model. But observed damped oscillations reduce this factor down to 100-1000.

The results obtained experimentally are upper limits of the real torque applied at the contact point. The observation of multiple aggregates oscillating, in the same

sequence with almost the same frequency and the torque's value caused by thermophoretic forces, indicates that the restoring torque is mainly caused by gas drag. However, these results are upper limits and real torques 100-1000 times larger than predicted by the model should not be discarded. In addition to it, if a critical displacement, $\xi = 3.2$ nm, is considered (Heim et al., 1999) instead of $\xi = 0.1$ assumed by (Dominik and Tielens, 1997), the ratio between experimental and theoretical rolling torques decreases to 50-100. However, $\xi = 3.2$ nm was measured for silicate grains and, although Dominik and Tielens (1997) assume the same $\xi = 0.1$ nm for all materials, it is probable that the value of ξ may differ considerably in the case of water ice. This subject remains as an aim for future studies.

Twisting

No linear sliding has been detected. In some cases, twisting motions of aggregates before their breakup have been observed. The determination of the twisting torque applied at the contact point can be estimated if the aggregate's moment of inertia and the rotation's angular acceleration are measured. The twisting motion presents two regimes: 1. acceleration and 2. twisting at constant velocity. It is remarkable that, in many cases, the aggregate keeps rotating during several loops before the breakup takes place.

Comparing the experimental twisting torques with their theoretical expected values, it can be seen that the laboratory measurements obtained are a factor 10 larger than the predictions. In this case, it fits better than in the rolling case. However, if sublimation corrections are considered, the theoretical torques are larger than the estimated results by the experiments. This happens for aggregates with a critical breaking force $F_c \lesssim 3 \times 10^{-9}$ N. As mentioned above, the model doesn't fully fit the experimental results below a certain grain size. However, lacking an alternative model, the validity of the measurement relies on the existent theory.

Bibliography

Adams, F. C., F. H. Shu, and C. J. Lada (1987, September). The Disks of T Tauri Stars with Flat Infrared Spectra. In *Bulletin of the American Astronomical Society*, Volume 19 of *Bulletin of the American Astronomical Society*, pp. 1096.

Anders, E. and N. Grevesse (1989). Abundances of the elements: Meteoritic and solar. *Geochimica et Cosmochimica Acta 53*(1), 197 – 214.

Andre, P. (2011). Spectral classification of embedded stars. In M. Gargaud, R. Amils, J. Quintanilla, I. Cleaves, HendersonJames (Jim), W. Irvine, D. Pinti, and M. Viso (Eds.), *Encyclopedia of Astrobiology*, pp. 1549–1553. Springer Berlin Heidelberg.

Andre, P. and T. Montmerle (1994, January). From T Tauri stars to protostars: Circumstellar material and young stellar objects in the rho Ophiuchi cloud. *Astrophys. J. 420*, 837–862.

Andre, P., D. Ward-Thompson, and M. Barsony (1993, March). Submillimeter continuum observations of Rho Ophiuchi A - The candidate protostar VLA 1623 and prestellar clumps. *Astrophys. J. 406*, 122–141.

Andre, P., D. Ward-Thompson, and M. Barsony (2000, May). From Prestellar Cores to Protostars: the Initial Conditions of Star Formation. *Protostars and Planets IV*, 59.

Arakawa, M. (1999, November). Collisional Disruption of Ice by High-Velocity Impact. *Icarus 142*, 34–45.

Armitage, P. J. (2010). *Astrophysics of Planet Formation*.

Armitage, P. J. (2011, September). Dynamics of Protoplanetary Disks. *Ann. Rev. Astron. Astrophys. 49*, 195–236.

Aumatell, G. and G. Wurm (2011a, November). Breaking the ice: planetesimal formation at the snowline. *Mon. Not. R. Astron. Soc. 418*, L1–L5.

Aumatell, G. and G. Wurm (2011b, October). Collisions of (sub-)mm size water-ice aggregates. In *EPSC-DPS Joint Meeting 2011*, pp. 424.

Aumatell, G. and G. Wurm (2014, January). Ice aggregate contacts at the nm-scale. *Mon. Not. R. Astron. Soc. 437*, 690–702.

Balbus, S. A. and J. F. Hawley (1991, July). A powerful local shear instability in weakly magnetized disks. I - Linear analysis. II - Nonlinear evolution. *Astrophys. J. 376*, 214–233.

Barman, T. S. (2008, March). On the Presence of Water and Global Circulation in the Transiting Planet HD 189733b. *Astrophys. J., Lett. 676*, L61–L64.

Bauer, T. (1993). A general analytical approach toward the thermal conductivity of porous media. *International Journal of Heat and Mass Transfer 36*(17), 4181 – 4191.

Beaulieu, J. P., D. M. Kipping, V. Batista, G. Tinetti, I. Ribas, S. Carey, J. A. Noriega-Crespo, C. A. Griffith, G. Campanella, S. Dong, J. Tennyson, R. J. Barber, P. Deroo, S. J. Fossey, D. Liang, M. R. Swain, Y. Yung, and N. Allard (2010, December). Water in the atmosphere of HD 209458b from 3.6-8 μm IRAC photometric observations in primary transit. *Mon. Not. R. Astron. Soc. 409*, 963–974.

Beckwith, S. V. W., A. I. Sargent, R. S. Chini, and R. Guesten (1990, March). A survey for circumstellar disks around young stellar objects. *Astron. J. 99*, 924–945.

Beitz, E., C. Güttler, J. Blum, T. Meisner, J. Teiser, and G. Wurm (2011, July). Low-velocity Collisions of Centimeter-sized Dust Aggregates. *Astrophys. J. 736*, 34.

Blum, J. (2004, May). Grain Growth and Coagulation. In A. N. Witt, G. C. Clayton, & B. T. Draine (Ed.), *Astrophysics of Dust*, Volume 309 of *Astronomical Society of the Pacific Conference Series*, pp. 369.

Blum, J. and G. Wurm (2000, January). Experiments on Sticking, Restructuring, and Fragmentation of Preplanetary Dust Aggregates. *Icarus 143*, 138–146.

Blum, J. and G. Wurm (2008, September). The Growth Mechanisms of Macroscopic Bodies in Protoplanetary Disks. *Ann. Rev. Astron. Astrophys. 46*, 21–56.

Blum, J., G. Wurm, S. Kempf, and T. Henning (1996). The Brownian Motion of Dust Particles in the Solar Nebula: an Experimental Approach to the Problem of Pre-planetary Dust Aggregation. *Icarus 124*, 441–451.

Bradford, C. M., A. D. Bolatto, P. R. Maloney, J. E. Aguirre, J. J. Bock, J. Glenn, J. Kamenetzky, R. Lupu, H. Matsuhara, E. J. Murphy, B. J. Naylor, H. T. Nguyen, K. Scott, and J. Zmuidzinas (2011, November). The Water Vapor Spectrum of APM 08279+5255: X-Ray Heating and Infrared Pumping over Hundreds of Parsecs. *Astrophys. J., Lett. 741*, L37.

Brauer, F., C. P. Dullemond, and T. Henning (2008, March). Coagulation, fragmentation and radial motion of solid particles in protoplanetary disks. *Astron. Astrophys. 480*, 859–877.

Bridges, F. G., K. D. Supulver, D. N. C. Lin, R. Knight, and M. Zafra (1996, October). Energy Loss and Sticking Mechanisms in Particle Aggregation in Planetesimal Formation. *Icarus 123*, 422–435.

Brisset, J., D. Heißelmann, S. Kothe, R. Weidling, and J. Blum (2013, September). The suborbital particle aggregation and collision experiment (SPACE): Studying the collision behavior of submillimeter-sized dust aggregates on the suborbital rocket flight REXUS 12. *Review of Scientific Instruments 84*(9), 094501.

Brogi, M., I. A. G. Snellen, R. J. de Kok, S. Albrecht, J. L. Birkby, and E. J. W. de Mooij (2013, April). Detection of Molecular Absorption in the Dayside of Exoplanet 51 Pegasi b? *Astrophys. J. 767*, 27.

Bujarrabal, V., K. Young, and A. Castro-Carrizo (2009, June). The physical conditions in Gomez's Hamburger (IRAS 18059-3211), a pre-MS rotating disk. *Astron. Astrophys. 500*, 1077–1087.

Carr, J. S. and J. R. Najita (2008, March). Organic Molecules and Water in the Planet Formation Region of Young Circumstellar Disks. *Science 319*, 1504–.

Chiang, E. and A. N. Youdin (2010, May). Forming Planetesimals in Solar and Extrasolar Nebulae. *Annual Review of Earth and Planetary Sciences 38*, 493–522.

Chokshi, A., A. G. G. M. Tielens, and D. Hollenbach (1993, April). Dust coagulation. *Astrophys. J. 407*, 806–819.

Ciesla, F. J. and J. N. Cuzzi (2006, March). The evolution of the water distribution in a viscous protoplanetary disk. *Icarus 181*, 178–204.

Clarke, C. J., A. Gendrin, and M. Sotomayor (2001, December). The dispersal of circumstellar discs: the role of the ultraviolet switch. *Mon. Not. R. Astron. Soc. 328*, 485–491.

Cotera, A. S., B. A. Whitney, E. Young, M. J. Wolff, K. Wood, M. Povich, G. Schneider, M. Rieke, and R. Thompson (2001, August). High-Resolution Near-Infrared Images and Models of the Circumstellar Disk in HH 30. *Astrophys. J. 556*, 958–969.

Currie, T. and S. J. Kenyon (2009, September). Deep MIPS Observations of the IC 348 Nebula: Constraints on the Evolutionary State of Anemic Circumstellar Disks and the Primordial-to-Debris Disk Transition. *Astron. J. 138*, 703–726.

Currie, T., C. J. Lada, P. Plavchan, T. P. Robitaille, J. Irwin, and S. J. Kenyon (2009, June). The Last Gasp of Gas Giant Planet Formation: A Spitzer Study of the 5 Myr Old Cluster NGC 2362. *Astrophys. J 698*, 1–27.

Cuzzi, J. N., R. C. Hogan, and K. Shariff (2008, November). Toward Planetesimals: Dense Chondrule Clumps in the Protoplanetary Nebula. *Astrophys. J. 687*, 1432–1447.

Cuzzi, J. N. and K. J. Zahnle (2004, October). Material Enhancement in Protoplanetary Nebulae by Particle Drift through Evaporation Fronts. *Astrophys. J. 614*, 490–496.

Cyr, K. E., W. D. Sears, and J. I. Lunine (1998, October). Distribution and Evolution of Water Ice in the Solar Nebula: Implications for Solar System Body Formation. *Icarus 135*, 537–548.

D'Angelo, G., R. H. Durisen, and J. J. Lissauer (2011). *Giant Planet Formation*, pp. 319–346.

Davis, S. S. (2005, July). The Surface Density Distribution in the Solar Nebula. *Astrophys. J., Lett. 627*, L153–L155.

Deckers, J. and J. Teiser (2013, June). Colliding Decimeter Dust. *Astrophys. J. 769*, 151.

Desch, S. J. (2007, December). Mass Distribution and Planet Formation in the Solar Nebula. *Astrophys. J. 671*, 878–893.

D'Hendecourt, L. B., L. J. Allamandola, and J. M. Greenberg (1985, November). Time dependent chemistry in dense molecular clouds. I - Grain surface reactions, gas/grain interactions and infrared spectroscopy. *Astron. Astrophys 152*, 130–150.

Dilley, J. P. (1993, September). Energy Loss in Collisions of Icy Spheres: Loss Mechanism and Size-Mass Dependence. *Icarus 105*, 225–234.

Ding, W., A. J. Howard, M. M. Peri, and C. Cetinkaya (2007). Rolling resistance moment of microspheres on surfaces: contact measurements. *Philosophical Magazine 87*(36), 5685–5696.

Dittrich, K., H. Klahr, and A. Johansen (2013, February). Gravoturbulent Planetesimal Formation: The Positive Effect of Long-lived Zonal Flows. *Astrophys. J. 763*, 117.

Dominik, C., J. Blum, J. N. Cuzzi, and G. Wurm (2007). Growth of Dust as the Initial Step Toward Planet Formation. *Protostars and Planets V*, 783–800.

Dominik, C. and A. G. G. M. Tielens (1995, September). Resistance to rolling in the adhesive contact of two elastic spheres. *Philosophical Magazine, Part A 72*, 783–803.

Dominik, C. and A. G. G. M. Tielens (1996). Resistance to sliding on atomic scales in the adhesive contact of two elastic spheres. *Philosphical Magazine A, Vol. 73, p.1279 73*, 1279.

Dominik, C. and A. G. G. M. Tielens (1997). The Physics of Dust Coagulation and the Structure of Dust Aggregates in Space. *Astrophys. J. 480*, 647.

Dullemond, C. P. and C. Dominik (2004, December). The Global Structure of Protoplanetary Disks. In J. Beaulieu, A. Lecavelier Des Etangs, and C. Terquem (Eds.), *Extrasolar Planets: Today and Tomorrow*, Volume 321 of *Astronomical Society of the Pacific Conference Series*, pp. 361.

Dullemond, C. P. and C. Dominik (2005, May). Dust coagulation in protoplanetary disks: A rapid depletion of small grains. *Astron. Astrophys. 434*, 971–986.

Dwek, E., V. Zubko, R. G. Arendt, and R. K. Smith (2004, May). Probing Interstellar Dust Models Through SAXS (Small Angle X-Ray Scattering). In A. N. Witt, G. C. Clayton, and B. T. Draine (Eds.), *Astrophysics of Dust*, Volume 309 of *Astronomical Society of the Pacific Conference Series*, pp. 499.

Eisner, J. A. (2007, May). Water vapour and hydrogen in the terrestrial-planet-forming region of a protoplanetary disk. *Nature 447*, 562–564.

Evans, N., N. Calvet, L. Cieza, J. Forbrich, L. Hillenbrand, C. Lada, B. Merín, S. Strom, and D. Watson (2009, January). The Diskionary: A Glossary of Terms Commonly Used for Disks and Related Objects, First Edition. *ArXiv e-prints*.

Garaud, P. and D. N. C. Lin (2007, January). The Effect of Internal Dissipation and Surface Irradiation on the Structure of Disks and the Location of the Snow Line around Sun-like Stars. *Astrophys. J. 654*, 606–624.

Geretshauser, R. J., R. Speith, C. Güttler, M. Krause, and J. Blum (2010, April). Numerical simulations of highly porous dust aggregates in the low-velocity collision regime. Implementation and calibration of a smooth particle hydrodynamics code. *Astron. Astrophys. 513*, A58.

Geretshauser, R. J., R. Speith, and W. Kley (2011, December). Collisions of inhomogeneous pre-planetesimals. *Astron. Astrophys. 536*, A104.

Gillett, F. C. (1986). IRAS observations of cool excess around main sequence stars. In F. P. Israel (Ed.), *Light on Dark Matter*, Volume 124 of *Astrophysics and Space Science Library*, pp. 61–69.

Gillett, F. C. and W. J. Forrest (1973, January). Spectra of the Becklin-Neugebauer point source and the Kleinmann-Low nebula from 2.8 to 13.5 microns. *Astrophys. J. 179*, 483–491.

Glassgold, A. E., R. Meijerink, and J. R. Najita (2009, August). Formation of Water in the Warm Atmospheres of Protoplanetary Disks. *Astrophys. J. 701*, 142–153.

Goldreich, P., Y. Lithwick, and R. Sari (2004, October). Final Stages of Planet Formation. *Astrophys. J. 614*, 497–507.

Grigorieva, A., P. Thébault, P. Artymowicz, and A. Brandeker (2007, November). Survival of icy grains in debris discs. The role of photosputtering. *Astron. Astroph. 475*, 755–764.

Gundlach, B., S. Kilias, E. Beitz, and J. Blum (2011, August). Micrometer-sized ice particles for planetary-science experiments - I. Preparation, critical rolling friction force, and specific surface energy. *Icarus 214*, 717–723.

Güttler, C., J. Blum, A. Zsom, C. W. Ormel, and C. P. Dullemond (2010, April). The outcome of protoplanetary dust growth: pebbles, boulders, or planetesimals?. I. Mapping the zoo of laboratory collision experiments. *Astron. Astrophys. 513*, A56.

Hadamcik, E., A. K. Sen, A. C. Levasseur-Regourd, R. Gupta, J. Lasue, and R. Botet (2013, February). Dust in Comet 103P/Hartley 2 coma during EPOXI mission. *Icarus 222*, 774–785.

Haisch, Jr., K. E., E. A. Lada, and C. J. Lada (2001, June). Disk Frequencies and Lifetimes in Young Clusters. *Astrophys. J., Lett. 553*, L153–L156.

Hartmann, L., N. Calvet, E. Gullbring, and P. D'Alessio (1998, March). Accretion and the Evolution of T Tauri Disks. *Astrophys. J. 495*, 385.

Hasegawa, T. I., E. Herbst, and C. M. Leung (1992, September). Models of gas-grain chemistry in dense interstellar clouds with complex organic molecules. *Astrophys. J., Suppl. Ser. 82*, 167–195.

Hatzes, A. P., F. G. Bridges, and D. N. C. Lin (1988, April). Collisional properties of ice spheres at low impact velocities. *Mon. Not. R. Astron. Soc 231*, 1091–1115.

Hayashi, C. (1981). Structure of the Solar Nebula, Growth and Decay of Magnetic Fields and Effects of Magnetic and Turbulent Viscosities on the Nebula. *Progress of Theoretical Physics Supplement 70*, 35–53.

Heim, L.-O., J. Blum, M. Preuss, and H.-J. Butt (1999, October). Adhesion and Friction Forces between Spherical Micrometer-Sized Particles. *Physical Review Letters 83*, 3328–3331.

Heißelmann, D., J. Blum, H. J. Fraser, and K. Wolling (2010, April). Microgravity experiments on the collisional behavior of saturnian ring particles. *Icarus 206*, 424–430.

Higa, M., M. Arakawa, and N. Maeno (1998, June). Size Dependence of Restitution Coefficients of Ice in Relation to Collision Strength. *Icarus 133*, 310–320.

Hobbs, P. V. (1974). *Ice physics*.

Hogerheijde, M. R. (2010, January). Structure and life time of circumstellar disks. In T. Montmerle, D. Ehrenreich, and A.-M. Lagrange (Eds.), *EAS Publications Series*, Volume 41 of *EAS Publications Series*, pp. 113–132.

Hollenbach, D. J., H. W. Yorke, and D. Johnstone (2000, May). Disk Dispersal around Young Stars. *Protostars and Planets IV*, 401.

Honda, M., A. K. Inoue, M. Fukagawa, A. Oka, T. Nakamoto, M. Ishii, H. Terada, N. Takato, H. Kawakita, Y. K. Okamoto, H. Shibai, M. Tamura, T. Kudo, and Y. Itoh (2009, January). Detection of Water Ice Grains on the Surface of the Circumstellar Disk Around HD 142527. *Astrophys. J., Lett. 690*, L110–L113.

Hughes, A. M., D. J. Wilner, C. Qi, and M. R. Hogerheijde (2008, May). Gas and Dust Emission at the Outer Edge of Protoplanetary Disks. *Astrophys. J. 678*, 1119–1126.

Humphreys, E. M. L., L. J. Greenhill, M. J. Reid, H. Beuther, J. M. Moran, M. Gurwell, D. J. Wilner, and P. T. Kondratko (2005, December). First Detection of Millimeter/Submillimeter Extragalactic H_2O Maser Emission. *Astrophys. J., Lett. 634*, L133–L136.

Ioppolo, S., H. M. Cuppen, C. Romanzin, E. F. van Dishoeck, and H. Linnartz (2008, October). Laboratory Evidence for Efficient Water Formation in Interstellar Ices. *Astrophys. J. 686*, 1474–1479.

Isella, A., L. Testi, A. Natta, R. Neri, D. Wilner, and C. Qi (2007, July). Millimeter imaging of HD 163296: probing the disk structure and kinematics. *Astron. Astrophys 469*, 213–222.

Jankowski, T., G. Wurm, T. Kelling, J. Teiser, W. Sabolo, P. J. Gutiérrez, and I. Bertini (2012, June). Crossing barriers in planetesimal formation: The growth of mm-dust aggregates with large constituent grains. *Astron. Astrophys. 542*, A80.

Jeans, J. H. (1919, June). The Present Position of the Nebular Hypothesis. *J. R. Astron. Soc. Can. 13*, 215.

Jewitt, D. (2009, May). The Active Centaurs. *Astron. J. 137*, 4296–4312.

Johansen, A., H. Klahr, and T. Henning (2006, January). Gravoturbulent Formation of Planetesimals. *Astrophys. J. 636*, 1121–1134.

Johnson, J. A. (2009, April). International Year of Astronomy Invited Review on Exoplanets. *Publ.. Astron. Soc. Pac. 121*, 309–315.

Johnson, K. L., K. Kendall, and A. D. Roberts (1971, September). Surface Energy and the Contact of Elastic Solids. *Royal Society of London Proceedings Series A 324*, 301–313.

Johnston, J. and V. Molinero (2012). Crystallization, melting, and structure of water nanoparticles at atmospherically relevant temperatures. *J Am Chem Soc 134*(15), 6650–9.

Kataoka, A., H. Tanaka, S. Okuzumi, and K. Wada (2013, September). Fluffy dust forms icy planetesimals by static compression. *Astron. Astrophys. 557*, L4.

Kato, M., Y.-I. Iijima, M. Arakawa, Y. Okimura, A. Fujimura, N. Maeno, and H. Mizutani (1995, February). Ice-on-ice impact experiments. *Icarus 113*, 423–441.

Kelling, T. and G. Wurm (2009, November). Self-Sustained Levitation of Dust Aggregate Ensembles by Temperature-Gradient-Induced Overpressures. *Physical Review Letters 103*(21), 215502.

Kelling, T., G. Wurm, and C. Dürmann (2011, November). Ice particles trapped by temperature gradients at mbar pressure. *Review of Scientific Instruments 82*(11), 115105.

Kelling, T., G. Wurm, and M. Köster (2014, March). Experimental Study on Bouncing Barriers in Protoplanetary Disks. *Astrophys. J. 783*, 111.

Kenyon, S. J. and L. Hartmann (1987, December). Spectral energy distributions of T Tauri stars - Disk flaring and limits on accretion. *Astrophys. J. 323*, 714–733.

Kerr, F. J. and G. R. Knapp (1974). The Gas-To Ratio in the Galaxy. In F. J. Kerr and S. C. Simonson (Eds.), *Galactic Radio Astronomy*, Volume 60 of *IAU Symposium*, pp. 179.

Klahr, H. and P. Bodenheimer (2006, March). Formation of Giant Planets by Concurrent Accretion of Solids and Gas inside an Anticyclonic Vortex. *Astrophys. J. 639*, 432–440.

Klahr, H. and A. Johansen (2008, August). Gravoturbulent planetesimal formation. *Physica Scripta Volume T 130*(1), 014018.

Knudsen, M. (1909). Eine Revision der Gleichgewichtsbedingung der Gase. Thermische Molekularströmung. *Annalen der Physik 336*, 205–229.

Krauss, O. and G. Wurm (2005, September). Photophoresis and the Pile-up of Dust in Young Circumstellar Disks. *Astrophys. J. 630*, 1088–1092.

Kretke, K. A. and D. N. C. Lin (2010, October). Structure of Magnetorotational Instability Active Protoplanetary Disks. *Astrophys. J. 721*, 1585–1592.

Krijt, S., C. Gttler, D. Heielmann, C. Dominik, and A. G. G. M. Tielens (2013). Energy dissipation in head-on collisions of spheres. *Journal of Physics D: Applied Physics 46*(43), 435303.

Kuroiwa, T. and S.-i. Sirono (2011, September). Evolution of Size Distribution of Icy Grains by Sublimation and Condensation. *Astrophys. J. 739*, 18.

Lada, C. J. (1987). Star formation - From OB associations to protostars. In M. Peimbert and J. Jugaku (Eds.), *Star Forming Regions*, Volume 115 of *IAU Symposium*, pp. 1–17.

Lada, C. J. and B. A. Wilking (1984, December). The nature of the embedded population in the Rho Ophiuchi dark cloud - Mid-infrared observations. *Astrophys. J. 287*, 610–621.

Leger, A., J. Klein, S. de Cheveigne, C. Guinet, D. Defourneau, and M. Belin (1979, October). The 3.1 micron absorption in molecular clouds is probably due to amorphous H2O ice. *Astron. Astrophys. 79*, 256–259.

Lichtenegger, H. I. M. and N. I. Komle (1991, April). Heating and evaporation of icy particles in the vicinity of comets. *Icarus 90*, 319–325.

Lis, D. C., D. A. Neufeld, T. G. Phillips, M. Gerin, and R. Neri (2011, September). Discovery of Water Vapor in the High-redshift Quasar APM 08279+5255 at z = 3.91. *Astrophys. J., Lett. 738*, L6.

Loerting, T. and N. Giovambattista (2006, December). TOPICAL REVIEW: Amorphous ices: experiments and numerical simulations. *Journal of Physics Condensed Matter 18*, 919.

Machida, R. and Y. Abe (2010, June). Terrestrial Planet Formation Through Accretion of Sublimating Icy Planetesimals in a Cold Nebula. *Astrophys. J. 716*, 1252–1262.

Mamajek, E. E. (2009, August). Initial Conditions of Planet Formation: Lifetimes of Primordial Disks. In T. Usuda, M. Tamura, and M. Ishii (Eds.), *American Institute of Physics Conference Series*, Volume 1158 of *American Institute of Physics Conference Series*, pp. 3–10.

Marboeuf, U., B. Schmitt, J.-M. Petit, O. Mousis, and N. Fray (2012, June). A cometary nucleus model taking into account all phase changes of water ice: amorphous, crystalline, and clathrate. *Astron. Astrophys. 542*, A82.

Marchewka, A., D. S. Abbott, and R. J. Beichner (2004, April). Oscillator damped by a constant-magnitude friction force. *American Journal of Physics 72*, 477–483.

Masset, F. S., A. Morbidelli, A. Crida, and J. Ferreira (2006, May). Disk Surface Density Transitions as Protoplanet Traps. *Astrophys. J. 642*, 478–487.

Mathis, J. S. (1986, September). The alignment of interstellar grains. *Astrophys. J. 308*, 281–287.

Meech, K. J., J. Pittichová, A. Bar-Nun, G. Notesco, D. Laufer, O. R. Hainaut, S. C. Lowry, D. K. Yeomans, and M. Pitts (2009, June). Activity of comets at large heliocentric distances pre-perihelion. *Icarus 201*, 719–739.

Meijerink, R., G. Aresu, I. Kamp, M. Spaans, W.-F. Thi, and P. Woitke (2012, November). Far-ultraviolet and X-ray irradiated protoplanetary disks: a grid of models. I. The disk structure. *Astron. Astrophys. 547*, A68.

Meijerink, R., K. M. Pontoppidan, G. A. Blake, D. R. Poelman, and C. P. Dullemond (2009, October). Radiative Transfer Models of Mid-Infrared H_2O Lines in the Planet-Forming Region of Circumstellar Disks. *Astrophys. J. 704*, 1471–1481.

Meisner, T., G. Wurm, and J. Teiser (2012, August). Experiments on centimeter-sized dust aggregates and their implications for planetesimal formation. *Astron. Astrophys. 544*, A138.

Meru, F., R. J. Geretshauser, C. Schäfer, R. Speith, and W. Kley (2013, November). Growth and fragmentation of centimetre-sized dust aggregates: the dependence on aggregate size and porosity. *Mon. Not. R. Astron. Soc. 435*, 2371–2390.

Min, M., C. P. Dullemond, M. Kama, and C. Dominik (2011, March). The thermal structure and the location of the snow line in the protosolar nebula: Axisymmetric models with full 3-D radiative transfer. *Icarus 212*, 416–426.

Mishima, O., L. D. Calvert, and E. Whalley (1984, August). 'Melting ice' I at 77 K and 10 kbar: a new method of making amorphous solids. *Nature 310*, 393–395.

Miyauchi, N., H. Hidaka, T. Chigai, A. Nagaoka, N. Watanabe, and A. Kouchi (2008, April). Formation of hydrogen peroxide and water from the reaction of cold hydrogen atoms with solid oxygen at 10 K. *Chemical Physics Letters 456*, 27–30.

Mo, Y. and I. Szlufarska (2010, Jan). Roughness picture of friction in dry nanoscale contacts. *Phys. Rev. B 81*, 035405.

Montmessin, F., R. M. Haberle, F. Forget, Y. Langevin, R. T. Clancy, and J.-P. Bibring (2007, August). On the origin of perennial water ice at the south pole of Mars: A precession-controlled mechanism? *Journal of Geophysical Research (Planets) 112*, 8.

Moore, N. W. and J. E. Houston (2010). The pull-off force and the work of adhesion: New challenges at the nanoscale. *Journal of Adhesion Science and Technology 24*(15-16), 2531–2544.

Muntz, E. P., Y. Sone, K. Aoki, S. Vargo, and M. Young (2002). Performance analysis and optimization considerations for a knudsen compressor in transitional flow. *Journal of Vacuum Science & Technology A: Vacuum, Surfaces, and Films 20*(1), 214–224.

Myers, P. C., F. C. Adams, H. Chen, and E. Schaff (1998, January). Evolution of the Bolometric Temperature and Luminosity of Young Stellar Objects. *Astrophys. J. 492*, 703–726.

Najita, J. R., S. E. Strom, and J. Muzerolle (2007, June). Demographics of transition objects. *Mon. Not. R. Astron. Soc. 378*, 369–378.

Noll, K. (2000, July). Hubble Heritage Observations of Gomez's Hamburger {IRAS 18059-3211}. In *HST Proposal*, pp. 9315.

Oka, A., T. Nakamoto, and S. Ida (2011, September). Evolution of Snow Line in Optically Thick Protoplanetary Disks: Effects of Water Ice Opacity and Dust Grain Size. *Astrophys. J. 738*, 141.

Okuzumi, S., H. Tanaka, H. Kobayashi, and K. Wada (2012, June). Rapid Coagulation of Porous Dust Aggregates outside the Snow Line: A Pathway to Successful Icy Planetesimal Formation. *Astrophys. J. 752*, 106.

Pagani, L., J. Steinacker, A. Bacmann, A. Stutz, and T. Henning (2010, September). The Ubiquity of Micrometer-Sized Dust Grains in the Dense Interstellar Medium. *Science 329*, 1622–.

Petrenko, V. F. and R. W. Whitworth (1999). *Physics of Ice*.

Piétu, V., S. Guilloteau, and A. Dutrey (2005, December). Sub-arcsec imaging of the AB Aur molecular disk and envelope at millimeter wavelengths: a non Keplerian disk. *Astron. Astrophys 443*, 945–954.

Podio, L., I. Kamp, C. Codella, S. Cabrit, B. Nisini, C. Dougados, G. Sandell, J. P. Williams, L. Testi, W.-F. Thi, P. Woitke, R. Meijerink, M. Spaans, G. Aresu, F. Ménard, and C. Pinte (2013, March). Water Vapor in the Protoplanetary Disk of DG Tau. *Astrophys. J., Lett. 766*, L5.

Podolak, M. (2010). The Location of the Snow Line in Protostellar Disks. In J. A. Fernandez, D. Lazzaro, D. Prialnik, and R. Schulz (Eds.), *IAU Symposium*, Volume 263 of *IAU Symposium*, pp. 19–28.

Poppe, T., J. Blum, and T. Henning (2000, April). Analogous Experiments on the Stickiness of Micron-sized Preplanetary Dust. *Astrophys. J. 533*, 454–471.

Renn, N. O., B. J. Bos, D. Catling, B. C. Clark, L. Drube, D. Fisher, W. Goetz, S. F. Hviid, H. U. Keller, J. F. Kok, S. P. Kounaves, K. Leer, M. Lemmon, M. B. Madsen, W. J. Markiewicz, J. Marshall, C. McKay, M. Mehta, M. Smith, M. P. Zorzano, P. H. Smith, C. Stoker, and S. M. M. Young (2009). Possible physical and thermodynamical evidence for liquid water at the phoenix landing site. *Journal of Geophysical Research: Planets 114*(E1), n/a–n/a.

Richling, S., D. Hollenbach, and H. W. Yorke (2006). *Destruction of protoplanetary disks by photoevaporation.* Cambridge Astrobiology.

Riviere-Marichalar, P., F. Ménard, W. F. Thi, I. Kamp, B. Montesinos, G. Meeus, P. Woitke, C. Howard, G. Sandell, L. Podio, W. R. F. Dent, I. Mendigutía, C. Pinte, G. J. White, and D. Barrado (2012, February). Detection of warm water vapour in Taurus protoplanetary discs by Herschel. *Astron. Astrophys. 538*, L3.

Roberge, A. and I. Kamp (2011). *Protoplanetary and Debris Disks*, pp. 269–295.

Rohatschek, H. (1995). Semi-empirical model of photophoretic forces for the entire range of pressures. *Journal of Aerosol Science 26*(5), 717–734.

Ros, K. and A. Johansen (2013, April). Ice condensation as a planet formation mechanism. *Astron. and Atrophys. 552*, A137.

Ruden, S. P. and J. B. Pollack (1991, July). The dynamical evolution of the protosolar nebula. *Astrophys. J. 375*, 740–760.

Safronov, V. S. (1966). The Protoplanetary Cloud and Its Evolution. *Astron. Zh. 43*, 817.

Saito, E. and S.-i. Sirono (2011). Planetesimal Formation by Sublimation. *Astrophys. J. 728*, 20.

Salyk, C., K. M. Pontoppidan, G. A. Blake, F. Lahuis, E. F. van Dishoeck, and N. J. Evans, II (2008, March). H_2O and OH Gas in the Terrestrial Planet-forming Zones of Protoplanetary Disks. *Astrophys. J., Lett. 676*, L49–L52.

Sasselov, D. D. and M. Lecar (2000, January). On the Snow Line in Dusty Protoplanetary Disks. *Astrophys. J. 528*, 995–998.

Satyawali, P. and A. Singh (2008). Dependence of thermal conductivity of snow on microstructure. *Journal of Earth System Science 117*(4), 465–475.

Schäfer, C., R. Speith, and W. Kley (2007, August). Collisions between equal-sized ice grain agglomerates. *Astron. Astrophys. 470*, 733–739.

Schegerer, A. A. and S. Wolf (2010, July). Spatially resolved detection of crystallized water ice in a T Tauri object. *Astron. Atrophys. 517*, A87.

Schräpler, R., J. Blum, A. Seizinger, and W. Kley (2012, October). The Physics of Protoplanetesimal Dust Agglomerates. VII. The Low-velocity Collision Behavior of Large Dust Agglomerates. *Astrphys. J. 758*, 35.

Seizinger, A. and W. Kley (2013, March). Bouncing behavior of microscopic dust aggregates. *Astron. Astrophys. 551*, A65.

Seizinger, A., R. Speith, and W. Kley (2012, May). Compression behavior of porous dust agglomerates. *Astron. Astrophys. 541*, A59.

Shimaki, Y. and M. Arakawa (2012, September). Low-velocity collisions between centimeter-sized snowballs: Porosity dependence of coefficient of restitution for ice aggregates analogues in the Solar System. *Icarus 221*, 310–319.

Sirono, S.-i. (2011a, June). Planetesimal Formation Induced by Sintering. *Astrophys. J., Lett. 733*, L41.

Sirono, S.-i. (2011b, July). The Sintering Region of Icy Dust Aggregates in a Protoplanetary Nebula. *Astrophys. J. 735*, 131.

Sirono, S.-i. (2013). Size and surface area of icy dust aggregates after a heating event at a protoplanetary nebula. *Astrophys. J. 765*(1), 50.

Stanley, M. (2003). *Emanuel Swedenborg: Essential Readings (Western Esoteric Master).* North Atlantic Books.

Stäuber, P., J. K. Jørgensen, E. F. van Dishoeck, S. D. Doty, and A. O. Benz (2006, July). Water destruction by X-rays in young stellar objects. *Astron. Astrophys. 453*, 555–565.

Steinacker, J., L. Pagani, A. Bacmann, and S. Guieu (2010, February). Direct evidence of dust growth in L183 from mid-infrared light scattering. *Astron. Astrophys. 511*, A9.

Stepinski, T. F. and P. Valageas (1997, March). Global evolution of solid matter in turbulent protoplanetary disks. II. Development of icy planetesimals. *Astron. Astrophys. 319*, 1007–1019.

Stevenson, D. J. and J. I. Lunine (1988, July). Rapid formation of Jupiter by diffuse redistribution of water vapor in the solar nebula. *Icarus 75*, 146–155.

Strom, K. M., S. E. Strom, S. Edwards, S. Cabrit, and M. F. Skrutskie (1989, May). Circumstellar material associated with solar-type pre-main-sequence stars - A possible constraint on the timescale for planet building. *Astron. J. 97*, 1451–1470.

Su, K. Y. L. and G. H. Rieke (2013, July). Signpost of Multiple Planets in Debris Disks. *ArXiv e-prints*.

Su, K. Y. L., G. H. Rieke, J. A. Stansberry, G. Bryden, K. R. Stapelfeldt, D. E. Trilling, J. Muzerolle, C. A. Beichman, A. Moro-Martin, D. C. Hines, and M. W. Werner (2006, December). Debris Disk Evolution around A Stars. *Astrophys. J. 653*, 675–689.

Sümer, B. and M. Sitti (2008). Rolling and spinning friction characterization of fine particles using lateral force microscopy based contact pushing. *Journ. of Adhesion Science and Technology 22*(5-6), 481–506.

Suyama, T., K. Wada, and H. Tanaka (2008, September). Numerical Simulation of Density Evolution of Dust Aggregates in Protoplanetary Disks. I. Head-on Collisions. *Astrophys. J. 684*, 1310–1322.

Swift, J. J., J. A. Johnson, T. D. Morton, J. R. Crepp, B. T. Montet, D. C. Fabrycky, and P. S. Muirhead (2013, February). Characterizing the Cool KOIs. IV. Kepler-32 as a Prototype for the Formation of Compact Planetary Systems throughout the Galaxy. *Astrophys. J. 764*, 105.

Tanaka, H., K. Wada, T. Suyama, and S. Okuzumi (2012). Growth of Cosmic Dust Aggregates and Reexamination of Particle Interaction Models. *Progress of Theoretical Physics Supplement 195*, 101–113.

Teiser, J., I. Engelhardt, and G. Wurm (2011, November). Porosities of Protoplanetary Dust Agglomerates from Collision Experiments. *Astrophys. J. 742*, 5.

Teiser, J. and G. Wurm (2009a, October). Decimetre dust aggregates in protoplanetary discs. *Astron. Atrophys. 505*, 351–359.

Teiser, J. and G. Wurm (2009b, March). High-velocity dust collisions: forming planetesimals in a fragmentation cascade with final accretion. *Mon. Not. R. Astron. Soc. 393*, 1584–1594.

Terada, H., A. T. Tokunaga, N. Kobayashi, N. Takato, Y. Hayano, and H. Takami (2007, September). Detection of Water Ice in Edge-on Protoplanetary Disks: HK Tauri B and HV Tauri C. *Astrophys. J. 667*, 303–307.

Thi, W. F., E. F. van Dishoeck, G. A. Blake, G. J. van Zadelhoff, J. Horn, E. E. Becklin, V. Mannings, A. I. Sargent, M. E. van den Ancker, A. Natta, and J. Kessler (2001, November). H_2 and CO Emission from Disks around T Tauri and Herbig Ae Pre-Main-Sequence Stars and from Debris Disks around Young Stars: Warm and Cold Circumstellar Gas. *Astrophys. J. 561*, 1074–1094.

Tielens, A. G. G. M. (2010, August). *The Physics and Chemistry of the Interstellar Medium*. Cambridge, UK: Cambridge University Press.

Tinetti, G., M. Liang, J. Beaulieu, Y. L. Yung, S. Carey, I. Ribas, J. Tennyson, B. Barber, N. Allard, G. Ballester, D. Sing, and F. Selsis (2007, October). Water Vapour In The Atmosphere Of An Extrasolar Planet. In *AAS/Division for Planetary Sciences Meeting Abstracts #39*, Volume 39 of *Bulletin of the American Astronomical Society*, pp. 467.

van Dishoeck, E. F., E. A. Bergin, D. C. Lis, and J. I. Lunine (2014, January). Water: from clouds to planets. *ArXiv e-prints*.

van Eymeren, J. and G. Wurm (2012, February). The implications of particle rotation on the effect of photophoresis. *Mon. Not. R. Astron. Soc. 420*, 183–186.

Vicente, S. M. and J. Alves (2005, October). Size distribution of circumstellar disks in the Trapezium cluster. *Astron. Astrophys. 441*, 195–205.

Wada, K., H. Tanaka, T. Suyama, H. Kimura, and T. Yamamoto (2007, May). Numerical Simulation of Dust Aggregate Collisions. I. Compression and Disruption of Two-Dimensional Aggregates. *Astrophys. J. 661*, 320–333.

Wada, K., H. Tanaka, T. Suyama, H. Kimura, and T. Yamamoto (2011, August). The Rebound Condition of Dust Aggregates Revealed by Numerical Simulation of Their Collisions. *Astrophys. J. 737*, 36.

Wagner, W., T. Riethmann, R. Feistel, and A. H. Harvey (2011, December). New Equations for the Sublimation Pressure and Melting Pressure of H2O Ice Ih. *Journal of Physical and Chemical Reference Data 40*(4), 043103.

Wang, H., R. C. Bell, M. J. Iedema, A. A. Tsekouras, and J. P. Cowin (2005, February). Sticky Ice Grains Aid Planet Formation: Unusual Properties of Cryogenic Water Ice. *Astrophys. J. 620*, 1027–1032.

Warren, S. G. (1982). Optical properties of snow. *Reviews of Geophysics 20*(1), 67–89.

Weidenschilling, S. J. (1977, July). Aerodynamics of solid bodies in the solar nebula. *Mon. Not. R. Astron. Soc. 180*, 57–70.

Weidenschilling, S. J. and J. N. Cuzzi (1993). Formation of planetesimals in the solar nebula. In E. H. Levy and J. I. Lunine (Eds.), *Protostars and Planets III*, pp. 1031–1060.

Weidenschilling, S. J., D. Spaute, D. R. Davis, F. Marzari, and K. Ohtsuki (1997, August). Accretional Evolution of a Planetesimal Swarm. *Icarus 128*, 429–455.

Weidling, R., C. Güttler, and J. Blum (2012, March). Free collisions in a microgravity many-particle experiment. I. Dust aggregate sticking at low velocities. *Icarus 218*, 688–700.

Weizsäcker, C. F. V. (1943). Über die Entstehung des Planetensystems. Mit 2 Abbildungen. *Z. Astrophys. 22*, 319.

Williams, I. P. and A. W. Cremin (1968, March). A Survey of Theories Relating to the Origin of the Solar System. *Q. J. R. Astron. Soc. 9*, 40.

Williams, J. P. and L. A. Cieza (2011, September). Protoplanetary Disks and Their Evolution. *Ann. Rev. Astron. Astrophys. 49*, 67–117.

Windmark, F., T. Birnstiel, C. Güttler, J. Blum, C. P. Dullemond, and T. Henning (2012, April). Planetesimal formation by sweep-up: how the bouncing barrier can be beneficial to growth. *Astron. Astrophys. 540*, A73.

Woolfson, M. M. (1993, March). The Solar - Origin and Evolution. *Q. J. R. Astron. Soc. 34*, 1–20.

Wurm, G. and J. Blum (1998, March). Experiments on Preplanetary Dust Aggregation. *Icarus 132*, 125–136.

Wurm, G., G. Paraskov, and O. Krauss (2005, November). Growth of planetesimals by impacts at 25 m/s. *Icarus 178*, 253–263.

Yamamoto, T., N. Nakagawa, and Y. Fukui (1983, June). The chemical composition and thermal history of the ice of a cometary nucleus. *Astron. Astrophys. 122*, 171–176.

Zheng, F. (2002). Thermophoresis of spherical and non-spherical particles: a review of theories and experiments. *Adv Colloid Interface Sci 97*(1-3), 255–78.

Zolensky, M. E. (2010, April). Liquid Water in Asteroids: Evidence from Fluid Inclusions in Meteorites. *LPI Contributions 1538*, 5278.

Zonetti, L. F. C., A. S. S. Camargo, J. Sartori, D. F. de Sousa, and L. A. O. Nunes (1999, March). A demonstration of dry and viscous damping of an oscillating pendulum. *European Journal of Physics 20*, 85–88.

Zsom, A., C. W. Ormel, C. Güttler, J. Blum, and C. P. Dullemond (2010, April). The outcome of protoplanetary dust growth: pebbles, boulders, or planetesimals? II. Introducing the bouncing barrier. *Astron. Astrophys. 513*, A57.

Own Publications and Conference Contributions

Publications in reviewed journals

- **G. Aumatell** & G. Wurm, *Breaking the ice: planetesimal formation at the snowline*, Monthly Notices of the Royal Astronomy Society, 418, L1-L5, 2011.
- **G. Aumatell** & G. Wurm, *Ice aggregate contacts at the nm-scale*, Monthly Notices of the Royal Astronomy Society, 437, 690-702, 2014.

Conference Contributions

- **G. Aumatell** & G. Wurm, *Water Ice Experiments in the Context of Planetesimal Formation at the Snowline*, Talk, LYDAN Meeting, Leiden (The Netherlands), 2014.
- **G. Aumatell** & G. Wurm, *Nanometer Contact Physics of Water Ice in Protoplanetary Disks, Breakup, Twisting and Rolling*, Poster and Abstract, Protostars & Planets VI, Heidelberg (Germany), 2013.
- **G. Aumatell** & G. Wurm, *Nanometer Contact Physics of Water Ice in Protoplanetary Disks, Breakup, Twisting and Rolling*, Poster and Abstract, The Chemical Cosmos, Windsor (United Kingdom), 2013.
- **G. Aumatell** & G. Wurm, *Contact Physics of Water Ice in Protoplanetary Disks, Breakup, Twisting, Rolling and Sliding*, Poster and Abstract, Planet Formation and Evolution, München (Germany), 2012.

- **G. Aumatell** & G. Wurm, *Contact Physics of Water Ice in Protoplanetary Disks, Breakup, Twisting, Rolling and Sliding*, Poster and Abstract, Chemistry and Infrared Spectroscopy of Interstellar Dust, Cuijk (The Netherlands), 2012.
- **G. Aumatell** & G. Wurm, *Collisions and Sublimation of Water Ice Aggregates in Protoplanetary Disks*, Talk, Young Astronomers Meeting, Paris (France), 2011.
- **G. Aumatell** & G. Wurm, *Collisions of (sub-)mm Size Water-Ice Aggregates*, Poster and Abstract, ESPC-DPS Joint Meeting, Nantes (France), 2011.
- **G. Aumatell** & G. Wurm, *Collisions of (sub-)mm Size Water-Ice Aggregates*, Poster and Abstract, The Chemical Cosmos, Valetta (Malta), 2011.
- **G. Aumatell** & G. Wurm, *Breaking the Ice: Planetesimal Formation at the Snowline*, Poster and Abstract, AstroSurf Meeting, Edinburgh (United Kingdom), 2011.
- **G. Aumatell** & G. Wurm, *First Observations of mm and sub-mm Ice Aggregation*, Talk, Planet Formation and Evolution, Göttingen (Germany), 2011.
- **G. Aumatell** & G. Wurm, *Dust and Ice Aggregation in Protoplanetary Disks*, Talk, Young Researchers Meeting, London (United Kingdom), 2010.

Acknowledgements

First of all, I would like to thank the European Union "Seventh Framework Programme" (FP7 / 2007-2013) which has funded most part of my research work through the program LASSIE (Laboratory Astrochemistry Surface Science in Europe) at the Universität Münster and at the University Duisburg- Essen, which has also contributed financially to this project.

This thesis has seen the light thanks mainly to the constant activity of Professor Gerhard Wurm, whom I deeply appreciate his effort in the tasks of monitoring and assessment. His patience, tolerance and communication skills have been fundamental for the realization of this work.

Thanks to all the members of my team, especially Dr. Jens Teiser, Dr. Thorben Kelling, Dr. Janine van Eymereen, Caroline de Beule, Markus Küpper, Christoph Lösche, Tim Jankowski, Thorsten Meisner, Manfred Aderholz and Beate Trispel. I can not forget the invaluable help that have carried out the administrative assistants Rosa Esteban from Duisburg and Anja Fliss from Münster. I communicate my appreciation also to Professor Helmut Zacharias, who has managed my arrival to Duisburg.

I deeply appreciate the LASSIE program staff for giving me the opportunity to attend many international conferences and workshops. It has given me the chance to stay at Graphic Science and the Open University, whom I sincerely express my gratitude too. But mainly, LASSIE allowed me to meet excellent scientists around the world, having the possibility to establish a nice friendship with some of them.

I also express my personal thanks to Pedro Rafael Alba Bernal who helped me by writing this work, and Jordi Carreras Martorell for his support in both personal and professional aspects. To my flatmates by helping me in the most difficult moments

of this thesis, as well as many friends who also supported me during the last years.

Finally, I dedicate this work to my family, especially my parents, without whom I could never get to fulfill the dream of studying astrophysics. My gratitude towards them can not be expressed by words alone. I love you with all my heart.

To all of you, thank you very much.

Erklärung

Die vorliegende Dissertation wurde von mir selbstständig verfasst. Bei der Abfassung der Dissertation wurden nur die angegebenen Hilfsmittel benutzt und alle wörtlich oder inhaltlich übernommenen Stellen sind als solche gekennzeichnet. Die Dissertation ist nur in diesem Promotionsverfahren eingereicht und es wird der Doktorgrad Dr. rer. nat. angestrebt.

Ort, Datum und Unterschrift